Universiteit Utrecht

Master thesis

Interactions in graphene in the quantum Hall regime

Marianne Knoester

December 11, 2015

Utrecht University
Institute for Theoretical Physics

Supervisor:
Prof. Dr. C. de Morais Smith (UU)

Co-supervisors:
Dr. C.F.J. Flipse (TU/e)
Dr. V. Juričić (UU)

Abstract

Recent experiments with hydrogenated graphene reveal fractal-like structures in the electronic density. They are reminiscent of fingering patterns in electronic droplets in the quantum Hall regime. Pseudo-magnetic fields in graphene due to chemical or mechanical strain might generate these kinds of patterns. In order to obtain a better understanding of these kinds of systems, we study two kinds of interactions in graphene, under the influence of a magnetic field. First of all, we consider the Coulomb interaction between electrons in the fractional quantum Hall regime, which can give rise to various kinds of electron-solid and -liquid phases. We construct the phase diagram in various Landau levels. Secondly, we study the interaction between electrons in the integer quantum Hall regime and an additional non-uniform magnetic field, which can drive the fractal growth in electronic droplets. We set up the groundwork for the application of this theory to the experiment.

Contents

Chapter 1

Introduction

During the last decade, graphene has attracted much attention of both theoretical and experimental scientists. The material, which consists of one layer of carbon atoms, has some unique properties with potential for widespread applications. Its lightweight, thin and flexible structure, high conductivity and huge mechanical strength make graphene an interesting material for the fabrication of, for instance, flexible display screens and electronic circuits. Besides the technological advancements it may provide, graphene turned out to be a very exciting material for theoretical physicists as well. Since the electrons in graphene have a linear dispersion, they behave as two-dimensional massless Dirac particles. Therefore, properties of relativistic particles, which are usually very difficult to investigate, are now accessible in table-top experiments. In this way, graphene can provide a connection between condensed-matter and high-energy physics.

Recent experiments at TU/e have revealed remarkable structures in hydrogenated graphene. After exposing graphene to a source of hydrogen atoms, which chemisorb to its surface, the sample is observed using atomic-force microscopy (AFM). The patterns that arise, as shown in Fig. 1.1a, are islands that seem to have a fractal-like structure. What are these islands actually consisting of? What is the underlying mechanism that drives the formation of these patterns? The answers to these questions would provide a great deal of insight in this curious phenomenon and they form the inspiration on which part of this thesis is based.

(a) (b)

Figure 1.1: (a) AFM measurement of hydrogenated graphene done by C.F.J. Flipse et al. (b) Viscous fingering in a Hele-Shaw cell (figure from Ref. [1]).

The formation of fractals is in fact ubiquitous in nature. Trees, ferns, coast lines and the nervous system are a few of the numerous natural phenomena that posses fractal struc-

tures. Less apparent examples of fractals in physics include the Hofstadter butterfly [2] and self-similarity in the fractional quantum Hall effect [3]. Interestingly, there exists an example of fractal behavior in a two-dimensional classical system, called the Hele-Shaw cell, that is reminiscent of the patterns that are observed in the experiment. Fig. 1.1b shows its set-up: between two glass plates, a viscous fluid is injected into another fluid with a higher viscosity. The injected fluid starts to form fingers due to inhomogeneities in the pressure. What makes this similarity with the experiment even more striking is that there is actually a quantum-mechanical analogy of this viscous fingering experiment, provided by Agam et al. [4]. An electronic droplet confined to a two-dimensional geometry in perpendicular magnetic field is exposed to a nonuniform magnetic field outside the droplet. This field plays the role of the inhomogeneous pressure and will generate the same kind of fingering patterns in the electronic droplet as those that were visible in the classical Hele-Shaw experiment. This makes us wonder if this mechanism can be driving the fingering patterns in hydrogenated graphene. One important ingredient in the fractal growth of electronic droplet is the presence of a magnetic field, which quantizes the kinetic energy of the electrons and leads to the integer quantum Hall effect. Although there is no external magnetic field present in the experiment, the deformations in the graphene sample that arise due to a combination of the hydrogen atoms and the substrate, may actually lead to a pseudo-magnetic field. Using this field, we can then nevertheless try to investigate whether the theory of Agam et al. can provide an explanation for the fractal structures that are observed in the hydrogenated graphene experiment.

The experiment forms the inspiration for the thesis, which focuses on graphene in a magnetic field. We will examine two different kinds of interactions that can arise in such systems. First of all, we will investigate the effect of interactions between the electrons, since these interactions are in principle always present. They turn out to be the driving mechanism of the fractional quantum Hall effect. Even more so, by varying the electron density or the magnetic field strength, we gain access to a variety of exotic electronic phases, such as Wigner crystals and electron-bubble phases. We will provide a theoretical description of these phases and analyze the phase diagram in graphene. This might not be directly applicable to the experiment, but it leads to results that are interesting on its own.

Secondly, we will explore the theory of viscous fingering in electronic liquids, which arises due to the interaction between electrons and a nonuniform magnetic field. We will subsequently set up a model that serves as a tool to apply this highly complex theory to actual experiments. We will do some example calculations which are necessary to derive the effective potential that describes the droplet's shape. In further research, these methods could be used as a starting point for Monte Carlo simulations.

The structure of the thesis is as follows. We start with a brief description of the experiment and the AFM measurements in Chapter 2. We proceed by explaining the physics of two-dimensional electrons in a perpendicular magnetic field in Chapter 3. Then, in Chapter 4 we will discuss the theory of graphene, including the quantum Hall effect in graphene and the formation of pseudo-magnetic fields due to strain. Next, we will consider electronic interactions in two-dimensional electron systems in Chapter 5 and explain about the various electron phases. Then, in Chapter 7, the theory of viscous fingering in electronic droplets in a quantum Hall system is addressed. In the subsequent chapters, we will apply those two theories to graphene, starting with electron phases in graphene in Chapter 6, followed by the hydrodynamical model in Chapter 8. Finally, we conclude and discuss the possibilities for further research in Chapter 9.

Chapter 2

The experiment

To make graphene nowadays, more advanced methods than the deceivingly simple 'scotch tape' method are used. At TU/e, graphene is epitaxially grown on silicon carbide (SiC) by thermal decomposition of the substrate [5–7]. First of all, surface defects and impurities of the SiC sample are removed by etching in an hydrogen atmosphere. Then, the SiC sample is heated up to 1650°C such that the silicon evaporates. Since the evaporation temperature of carbon is higher than that of silicon, the carbon atoms will stay at the surface. Some of the carbon atoms in this layer are covalently bonded to the silicon atoms in the substrate. As a results, this layer will not have the same electronic properties as graphene, hence it acts a buffer layer (see Fig. 2.1a). On top of that, another layer of carbon atoms is grown which serves as the actual graphene sample (see Fig. 2.1b). Since some of the silicon atoms in the top of the substrate are not bonded with the carbon atoms, they are so-called dangling bonds.

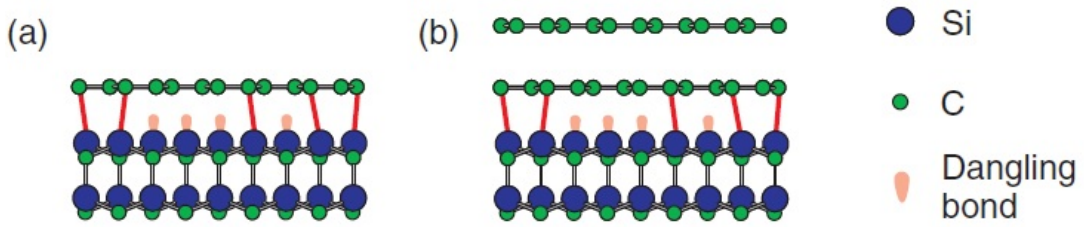

Figure 2.1: Schematic picture of (a) the buffer layer on top of SiC substrate consisting of carbon atoms, some of which are bonded to the substrate and (b) the monolayer of graphene on top of the buffer layer. Figure from Ref. [6].

Although the aim is to make the actual graphene layer as pristine as possible, the substrate inevitably has some effect on the graphene. Here, it are the dangling bonds that influence its structure mostly. The buffer layer on top of the SiC substrate 'feels' the unsaturated bonds and as a results it deforms, that is, above the dangling bonds the buffer layer forms a bump. Since the dangling bonds are arranged in a triangular lattice, with a lattice spacing of about 2 nm, there is also a periodic deformation in the buffer layer [8]. The actual graphene layer follows the morphology of the buffer layer, hence it also possesses this triangular lattice of bumps, albeit with a smaller amplitude. In Fig. 2.2a, a cross-section of the substrate with the two layer is shown. The deformation in the buffer layer is clearly visible. The actual graphene layer looks flat, but upon careful inspection, one can see a slight deformation above the point where the buffer layer is also

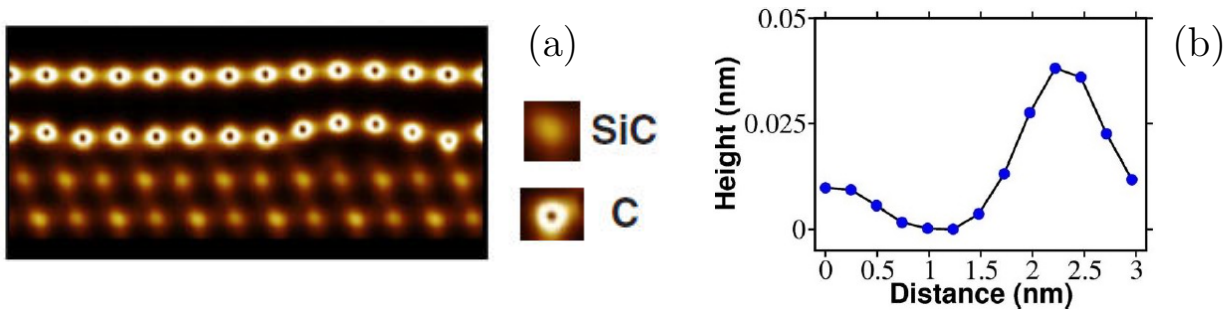

Figure 2.2: (a) Cross-section of buffer layer and actual graphene layer on top of the SiC substrate. The bumping effect is the largest in the buffer layer, but it is still visible in the top graphene layer. (b) Height of the graphene layer. Figures from Ref. [8].

deformed. In Fig. 2.2b the height of the graphene layer is shown. There we can see that the bump has an amplitude of 0.04 nm.

Having fabricated a layer of graphene with this method, the sample is subsequently exposed to a source of hydrogen atoms, which chemisorb to the graphene surface. The hydrogen atom also deform the surface, just like the dangling bonds. When the hydrogenation dose is low, the hydrogen atoms are probably more likely to sit on sites above the dangling bonds. Thereby, they lift the bump in the graphene layer that was already there due to the substrate. We expect in principle that the hydrogen atoms cover these preferential sites first and upon further increasing the hydrogen dose they cover the surface randomly. Furthermore, we expect the hydrogen atoms to stay fixed at their places once they are bonded to the surface.

When the hydrogenated graphene sample is observed using AFM, some remarkable patterns appear, as shown in Fig. 2.3. We can see islands with fractal-like structures. The number of islands increases with increasing hydrogen dose. However, the islands never seem to merge into each other. The line in Fig. 2.3a in probably due to some defect, such as a crease in the graphene sheet. The origin of these structures is not fully understood yet. As a first suggestion, we might consider the possibility that they are simply the hydrogen atoms themselves that cluster under the influence of some underlying mechanism. However, as the AFM measurements by Flipse et al. reveal, the height of the hydrogenated sample is in the order of nanometers. It is quite unlikely that the mere effect of bonding hydrogen atoms to graphene (which is already atomically thin) leads to a sample that is nanometers thick. Compare this, for example, to the height of the bumps due to the substrate; they have an amplitude of 0.04 nm. The hydrogen may increase the amplitude of the bumps, but it is doubtful that it will increase two orders of magnitude. As an alternative explanation, we can consider the possibility that the tip of the AFM device was charged. Then, the force between the tip and the surface (which is in fact what an AFM measures) can become very large if there is charge on the sample. This suggests that the patterns in Fig. 2.3 are actually patterns in the charge density. However, scanning tunneling microscopy (STM) measurements will have to be performed in order to determine the details of the islands more precisely.

Regardless of the origin of these structures, there is a remarkable similarity between these patters and fractal structures appearing in classical fluids. These patterns are, in fact, reminiscent of fingering patterns that arise in Laplacian growth processes. Interestingly, there is a description of such processes in electronic droplets [4]. They arise in

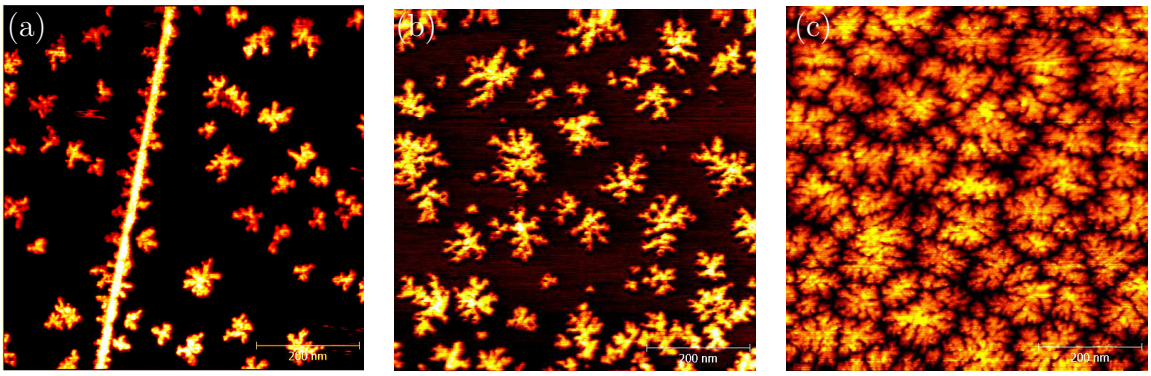

Figure 2.3: AFM images (made by Flipse et al.) of hydrogenated graphene for a low (a), medium (b) and high (c) hydrogen dose. Images are $700 \times 700\,\mathrm{nm}$.

quantum Hall systems with an additional nonuniform magnetic field. In this experiment, the pseudo-magnetic fields that arises due to strain in the sample might provide this magnetic field. It is well-known that mechanical deformations in graphene can lead to pseudo-magnetic fields. In this sample, there are deformations due to the substrate and the hydrogen atoms, but these deformations are nevertheless not large enough to generate pseudo-magnetic fields. It is then the chemical strain that the hydrogen atom imposes on the carbon bonds that generates the pseudo-magnetic fields. However, we can model the deformations plus the chemical strain by some effective deformation, which will lead to a pseudo-magnetic field. Notice furthermore that this is a general model that applies to mechanical deformations in graphene in general, which are strong enough to generate pseudo-magnetic fields. Secondly, the principle of fingering in electronic droplets is irrelevant of the mechanism that generates the (pseudo-)magnetic fields, thus it is anyhow instructive for the experiment to study them, and it is theoretically interesting on its own. In Chapters 7 and 8, we will explain this mechanism in detail and investigate how we possibly could apply this to this experimental set-up.

Chapter 3

The quantum Hall effect

3.1 Introduction

In 1879, Edwin Hall discovered that a current through an electrical conductor in a perpendicular magnetic field not only produces a voltage in the direction of the current, but also a voltage transverse to it (called the Hall voltage). This was called the Hall effect, named after its discoverer. It can be explained classically by the Lorentz force which is exerted on the electrons by the magnetic field. This force is perpendicular to the motion of the electrons and will cause the electrons to pile up at one edge of the conductor, creating a potential difference that can be measured transverse to the direction of the current, as shown in Fig. 3.1. In Section 3.2, we will explain in detail the procedure to set up the equations of motion for the electrons and to calculate the Hall resistance. It will turn out that it is is linear in the magnetic field strength. This is a classical effect, that is only valid for sufficiently high temperatures. At low temperatures and in high magnetic fields, quantum mechanical effects start to play a dominant role and will change this continuous, linear behavior. Klaus von Klitzing discovered in 1980 that in this quantum mechanical regime the Hall resistance is quantized, taking the values

$$R_H = \frac{h}{e^2}\frac{1}{\nu}, \tag{3.1}$$

where h/e^2 is the resistance quantum and ν is called the filling factor, which takes integer values. One of the most salient features of this integer quantum Hall effect (IQHE) is that the system size is irrelevant. From the relation between resistance R and resistivity ρ,

$$R = \rho L^{(2-d)},$$

where L is the length of a hypercube in d dimensions, we can see that in two dimensions, the resistance and resistivity coincide and the resistance is indeed scale invariant [9]. This means that one can measure the resistance of a sample to very high accuracy without having to measure the dimensions of the sample. The so-called von Klitzing constant $R_K = h/e^2$ has been determined up to an accuracy in the order of 10^{-10}, and has been adopted as a new standard for resistance [10].

In Fig. 3.2, the typical character of the quantum Hall effect is depicted. There are plateaus in the transverse resistivity at the quantized values $h/e^2\nu$ and the plateaus are accompanied by a vanishing longitudinal resistivity. At the transition from one plateau to the next one, there is a peak in the longitudinal resistivity. The explanation of the

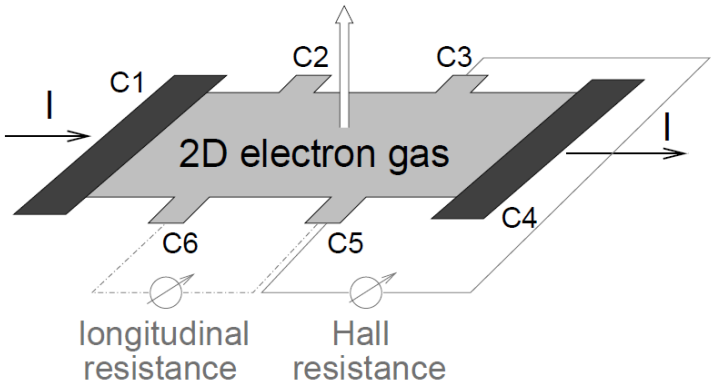

Figure 3.1: A two-dimensional electron gas in a perpendicular magnetic field shows the classical Hall effect at high temperatures. The Hall resistance is measured transverse to the direction of the applied current. Figure from Ref. [11].

quantum Hall effect is more involved than the classical analogue. It relies on quantization of electronic orbitals into so-called Landau levels and the presence of impurities in the sample. In Section 3.3, we will derive the Landau quantization, which will predict the quantization of the resistivity. In Section 3.4, we will explain how the impurities cause localization of electrons in the bulk, which explains this characteristic picture of plateaus and peaks shown in Fig. 3.2.

Three years after the discovery of the IQHE, Tsui, Störmer and Gossard discovered a Hall resistance quantization of $\nu = 1/3$ [12]. Since then, a whole range of plateaus at fractionally filled Landau levels has been discovered, as shown in Fig. 3.3 [11]. This opened the door to an even more mysterious field of the fractional quantum Hall effect (FQHE). Whereas the IQHE was easily understood in terms of the Landau quantization of the kinetic energy of the electrons, the FQHE relies on strong electronic interactions [11]. Since it occurs when a Landau level is partially filled, the kinetic energy is constant and plays no role. Instead, the interactions between the electrons become relevant. Since we are dealing with strongly-correlated electrons, perturbation is useless to describe the system. In 1983 Laughlin proposed a trial wave function to describe the FQHE for $\nu = 1/p$, where p is an odd integer, as an incompressible electron liquid [13]. Another description for the values $\nu = p/(2sp \pm 1)$, where p and s are integers was given by Jain in terms of composite fermions. For these values, the FQHE can be viewed as and IQHE for quasi-particles consisting of a combination of electrons and flux quanta [14, 15]. The fractional regime indeed exhibits a plethora of exotic phenomena, the description of which is outside the scope of this thesis.

Since graphene is also a two-dimensional electron system, one may expect to find quantum Hall effects in graphene. Indeed, in 2005, a quantization of the Hall resistance at filling factors $\nu = 2(2n+1)$ was reported in graphene [16,17]. Due to the special structure of graphene, the electrons do not behave like electrons in normal two-dimensional electron gases (2DEGs), but rather like massless, relativistic particles. This leads to a change in the Landau levels and hence in the quantization of the Hall resistivity. Furthermore, since the typical spacing between the energy levels is much larger in graphene, the quantum Hall effect can be observed at temperature as high as room temperature. In Section 4.4, we will give a detailed description on the quantum Hall effect in graphene.

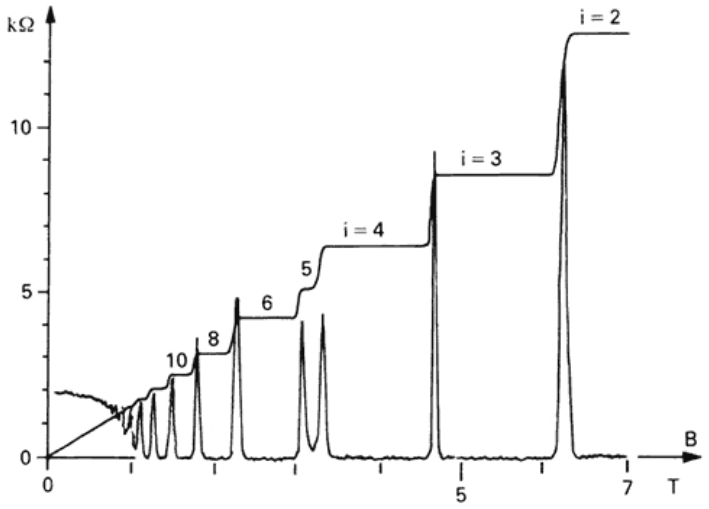

Figure 3.2: Plateaus in the transverse resistivity are visible for high magnetic fields. They are accompanied by a vanishing longitudinal resistivity. At the transition between the plateaus the longitudinal resistivity becomes finite. Figure from Ref. [18].

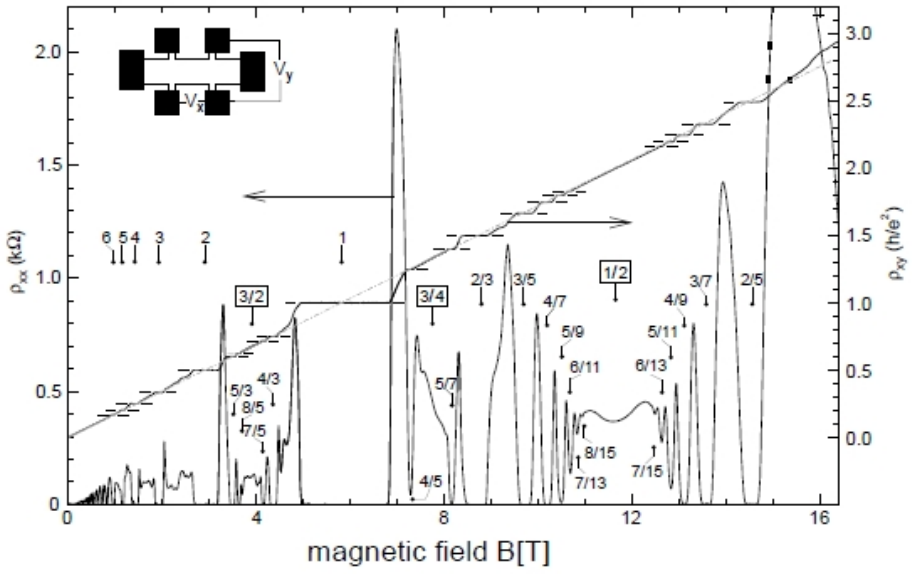

Figure 3.3: Characteristic behavior of the FQHE. The Hall resistivity shows plateaus at numerous fractional values of the filling factor, accompanied by peaks in the longitudinal resistivity. Figure from Ref. [11]

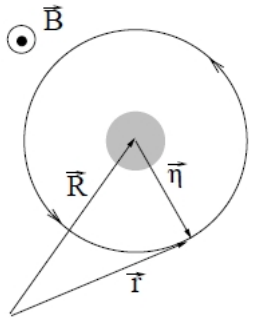

Figure 3.4: Electron at position $\boldsymbol{r}$ makes a cyclotron motion around the guiding centered at $\boldsymbol{R}$ in a perpendicular magnetic field $\boldsymbol{B}$.

3.2 Classical Hall effect

For a particle with charge $-e$ and mass m, moving in the xy-plane under the influence of a magnetic field $\mathbf{B} = B\hat{z}$, the equation of motion is $m\mathbf{a} = -e\mathbf{v} \times \mathbf{B}$. The two components of this equation are given by

$$\begin{aligned} \ddot{x} &= -\omega_c \dot{y}, \\ \ddot{y} &= \quad \omega_c \dot{x}, \end{aligned} \tag{3.2}$$

where we defined the cyclotron frequency $\omega_c \equiv eB/m$. It can easily be seen that the solution to this set of equations is given by

$$\begin{aligned} x(t) &= X + r\sin(\omega_c t + \phi), \\ y(t) &= Y + r\cos(\omega_c t + \phi), \end{aligned} \tag{3.3}$$

where ϕ is some arbitrary phase and X and Y are the coordinates of the guiding center $\boldsymbol{R}$ around which the particle moves in a circular motion, as shown in Fig. 3.4. For future reference, we also define the cyclotron variable $\boldsymbol{\eta} = \boldsymbol{r} - \boldsymbol{R}$, which described the cyclotron motion.

Subsequently, we consider an additional, external electric field $\boldsymbol{E} = E_x\hat{x} + E_y\hat{y}$. The equation of motion is now $m\mathbf{a} = -e\boldsymbol{E} - e\mathbf{v} \times \mathbf{B}$, which corresponds to

$$\begin{aligned} \dot{v}_x &= \frac{-eE_x}{m} - \omega_c v_y, \\ \dot{v}_y &= \frac{-eE_y}{m} + \omega_c v_x. \end{aligned} \tag{3.4}$$

Taking time derivatives on both sides and solving for $\dot{\boldsymbol{v}}$ is straightforward and yields

$$\begin{aligned} \dot{v}_x &= C\cos(\omega_c t), \\ \dot{v}_y &= C\sin(\omega_c t), \end{aligned}$$

where C is some constant. Substituting this back into Eq. (3.4) and solving for v_x and v_y leads to

$$\begin{aligned} v_x &= \frac{C}{\omega_c}\sin(\omega_c t) + \frac{eE_y}{m\omega_c}, \\ v_y &= -\frac{C}{\omega_c}\cos(\omega_c t) - \frac{eE_x}{m\omega_c}. \end{aligned}$$

Hence, the velocity of the particles $\boldsymbol{v} = \boldsymbol{v}_c + \boldsymbol{v}_D$ consists of a cyclotron velocity that accounts for the cyclotron motion of the particle, as illustrated in Eq. (3.3), and a constant that describes the drift velocity due to the electric field. This drift velocity is called the Hall drift and it is defined by

$$\boldsymbol{v}_D = \frac{\boldsymbol{E} \times \boldsymbol{B}}{B^2}. \tag{3.5}$$

To determine the resistivity and conductivity we look for static solutions to the equation of motion, i.e., $\mathrm{d}\boldsymbol{p}/\mathrm{d}t = 0$. Furthermore, we add an impurity term $-\boldsymbol{p}/\tau$, which describes the decrease in momentum due to the diffusion of electrons by impurities, where τ is the relaxation time. Therefore, we solve

$$0 = \frac{\mathrm{d}\boldsymbol{p}}{\mathrm{d}t} = -e\left(\boldsymbol{E} + \frac{1}{m}\boldsymbol{p} \times \boldsymbol{B}\right) - \frac{\boldsymbol{p}}{\tau}.$$

This yields the two equations

$$\begin{aligned} eE_x &= -\omega_c p_y - \frac{p_x}{\tau}, \\ eE_y &= \omega_c p_x - \frac{p_y}{\tau}, \end{aligned}$$

which may be rewritten as

$$\begin{aligned} \sigma_0 E_x &= -en_{el}\frac{p_x}{m} - (\omega_c\tau)en_{el}\frac{p_y}{m}, \\ \sigma_0 E_y &= (\omega_c\tau)en_{el}\frac{p_x}{m} - en_{el}\frac{p_y}{m}. \end{aligned} \tag{3.6}$$

Here, σ_0 is the Drude conductivity given by $\sigma_0 = n_{el}e^2\tau/m$. The current density is related to the momentum by $\boldsymbol{j} = -en_{el}\boldsymbol{p}/m$, with n_{el} denoting the electron density. With this we can write Eq. (3.6) in matrix form as $\boldsymbol{E} = \rho\boldsymbol{j}$. The resistivity ρ can then be obtained, together with its inverse, the conductivity σ. They read

$$\rho = \begin{pmatrix} 1/\sigma_0 & \frac{B}{en_{el}} \\ -\frac{B}{en_{el}} & 1/\sigma_0 \end{pmatrix}, \qquad \sigma = \begin{pmatrix} \sigma_L & -\sigma_H, \\ \sigma_H & \sigma_L \end{pmatrix},$$

where

$$\sigma_L = \frac{\sigma_0}{1 + \omega_c^2\tau^2}, \qquad \sigma_H = \omega_c\tau\frac{\sigma_0}{1 + \omega_c^2\tau^2}.$$

In the limit of vanishing impurities, i.e., $\tau \to \infty$, the resistivity and conductivity reduce to

$$\rho = \begin{pmatrix} 0 & \frac{B}{en_{el}} \\ -\frac{B}{en_{el}} & 0 \end{pmatrix}, \qquad \sigma = \begin{pmatrix} 0 & -\frac{en_{el}}{B}, \\ \frac{en_{el}}{B} & 0 \end{pmatrix}. \tag{3.7}$$

Notice that because of the matrix form, we arrive at the somewhat peculiar situation where the longitudinal components of both the resistivity and conductivity vanish in the limit of pure samples. The transverse, or Hall resistance $\rho_H = B/en_{el}$ is linear in B. This result holds in the classical regime at high temperatures.

3.3 Landau quantization

In order to eventually understand the quantum Hall effect, we will first study the quantum mechanical behavior of charged particles in a perpendicular magnetic field, in the absence of electric fields. For convenience, we will ignore spin degeneracy here. First, we will set up the Lagrangian for this situation, from which we can derive the Hamiltonian and the canonical variables. Then, we will continue to quantize the theory and arrive at the Hamiltonian operator and its eigenvalues.

In order to set up the Lagrangian for this problem, we first write the magnetic field in terms of the vector potential, $\boldsymbol{B} = \nabla \times \boldsymbol{A}$, such that the force on the particle can be written as:

$$\begin{aligned}\boldsymbol{F} &= -e(\boldsymbol{v} \times \nabla \times \boldsymbol{A}) \\ &= -e\nabla(\boldsymbol{v} \cdot \boldsymbol{A}) - \boldsymbol{A}(\nabla \cdot \boldsymbol{v}) \\ &= -e\nabla(\boldsymbol{v} \cdot \boldsymbol{A}).\end{aligned}$$

Since the potential energy U is related to the force by $\boldsymbol{F} = -\nabla U$, we can derive that $U = e(\boldsymbol{v} \cdot \boldsymbol{A})$. The Lagrangian is then given by

$$L(x, y, \dot{x}, \dot{y}) = \frac{m}{2}(\dot{x}^2 + \dot{y}^2) - e(A_x\dot{x} + A_y\dot{y}).$$

From this Lagrangian, we can derive the canonical momentum

$$p_x = \frac{\partial L}{\partial \dot{x}} = m\dot{x} - eA_x, \qquad p_y = \frac{\partial L}{\partial \dot{y}} = m\dot{y} - eA_y.$$

Obviously, this canonical momentum is not invariant under a gauge transformation $\boldsymbol{A} \to \boldsymbol{A} + \nabla\chi$, but the mechanical momentum $\boldsymbol{\Pi} \equiv m\dot{\boldsymbol{r}} = \boldsymbol{p} + e\boldsymbol{A}$ is. Therefore, we will write the Hamiltonian in terms of the latter,

$$\begin{aligned}H(x, y, p_x, p_y) &= \dot{x}p_x + \dot{y}p_y - L(x, y, \dot{x}, \dot{y}) \\ &= \frac{1}{2m}\left((p_x + eA_x)^2 + (p_y + eA_y)^2\right) \\ &= \frac{1}{2m}\left(\Pi_x^2 + \Pi_y^2\right).\end{aligned} \tag{3.8}$$

Notice that we can express the cyclotron variable, introduced in section 3.2, in terms of this mechanical momentum as

$$\eta_x = -\frac{\Pi_y}{eB}, \qquad \eta_y = \frac{\Pi_x}{eB}. \tag{3.9}$$

In this Hamiltonian formalism, we can now continue to quantize the theory by imposing canonical commutation relations between the position and canonical momentum:

$$[x, p_x] = [y, p_y] = i\hbar, \qquad [x, y] = [p_x, p_y] = [x, p_y] = [y, p_x] = 0.$$

To compute the commutator of Π_x and Π_y, we may use the formula

$$[A, f(B)] = \frac{df}{dB}[A, B], \tag{3.10}$$

which is valid for any two operators A and B for which $[A,[A,B]] = [B,[A,B]] = 0$. In this case, we have $[x,[x,p_x]] = [y,[y,p_y]] = 0$, and we may write

$$\begin{aligned}[p_x, A_y(x,y)] &= \frac{\partial A_y}{\partial x}[p_x, x] = -i\hbar\partial_x A_y, \\ [p_y, A_x(x,y)] &= \frac{\partial A_x}{\partial y}[p_y, y] = -i\hbar\partial_y A_x,\end{aligned} \tag{3.11}$$

where we denoted $\partial_x \equiv \frac{\partial}{\partial x}$ and $\partial_y \equiv \frac{\partial}{\partial y}$. Notice that the commutator of $A_x(x,y)$ and $A_y(x,y)$ vanishes because x and y commute. Hence, we have

$$[\Pi_x, \Pi_y] = i\hbar e(\partial_y A_x - \partial_x A_y) = -i\hbar e(\nabla \times \boldsymbol{A})_z = -i\hbar eB.$$

We define the magnetic length as $l_B \equiv \sqrt{\hbar/eB}$, which allows us to write

$$[\Pi_x, \Pi_y] = -i\frac{\hbar^2}{l_B^2}. \tag{3.12}$$

Notice that since the x- and y-components of the mechanical momentum do not commute, they can not be determined simultaneously. Hence, if you measure the velocity of a particle in the x-direction, you can not determine the velocity in the y-direction at the same time, due to the uncertainty principle.

If we consider the Hamiltonian given by Eq. (3.8) together with the commutator in Eq. (3.12), we notice that the system is similar to the one-dimensional quantum-mechanical harmonic oscillator. In that light, we will introduce ladder operators

$$a \equiv \frac{l_B}{\sqrt{2}\hbar}(\Pi_x - i\Pi_y), \qquad a^\dagger \equiv \frac{l_B}{\sqrt{2}\hbar}(\Pi_x + i\Pi_y), \tag{3.13}$$

such that

$$[a, a^\dagger] = 1.$$

The Hamiltonian in Eq. (3.8) can then be rewritten as

$$H = \hbar\omega_c\left(a^\dagger a + \frac{1}{2}\right). \tag{3.14}$$

From the well known properties of the harmonic oscillator, we can now readily conclude that the energy levels of a charged particle in a magnetic field are given by

$$\epsilon_n = \hbar\omega_c\left(n + \frac{1}{2}\right).$$

These energy levels are referred to as Landau levels.

3.3.1 Degeneracy of Landau levels

We have seen that Π_x and Π_y are conjugate variables, which gave rise to a harmonic oscillator with frequency ω_c and energy ϵ_n, where n is a quantum number that describes the levels of the system. Physically, it is clear that the mechanical momentum is conserved, which means that Π_x and Π_y are constants of motion. If we compare the original Hamiltonian in Eq. (3.8) with the one in Eq. (3.14), we notice that the former is described

by two sets of conjugate variables (x, p_x) and (y, p_y), whereas the latter only contains one set of conjugate variables $(a, a^\dagger)$. This would imply there exists another quantum number, which we will denote by m, which we must include to describe the complete system. Since the energy does not depend on m, this quantum number must represent a degeneracy of the energy levels. Corresponding to m, there will be a set of conjugate variables, independent of Π_x and Π_y, that are constants of motion. We will show that X and Y, which are the guiding centers of the cyclotron motion in the classical picture, satisfy these criteria and will constitute the degeneracy.

In order to show this, we first compute the commutation relation of X and Y. From Eqs. (3.2) and (3.3) one can write

$$X = x - \frac{1}{\omega_c^2}\ddot{x} = x - \frac{1}{m\omega_c}(p_y + eA_y), \qquad Y = y - \frac{1}{\omega_c^2}\ddot{y} = y + \frac{1}{m\omega_c}(p_x + eA_x). \quad (3.15)$$

The commutator is then given by

$$\begin{aligned}
[X, Y] &= \frac{1}{m\omega_c}\left([x, p_x] - [p_y, y]\right) - \frac{e}{m^2\omega_c^2}\left([p_y, A_x] + [A_y, p_x]\right) \\
&= \frac{2i\hbar}{m\omega_c} - \frac{ei\hbar}{m^2\omega_c^2}(\partial_x A_y - \partial_y A_x) \\
&= il_B^2, \qquad (3.16)
\end{aligned}$$

where we used Eq. (3.11) and the fact that $(\partial_x A_y - \partial_y A_x) = (\nabla \times \boldsymbol{A})_z = B$. Hence, X and Y are conjugate variables. We can also compute the commutator of X with the Hamiltonian:

$$\begin{aligned}
[X, H] &= \frac{1}{2m}[x - \frac{1}{m\omega_c}\Pi_y, \Pi_x^2 + \Pi_y^2] \\
&= \frac{1}{2m}\left([x, \Pi_x^2] - \frac{1}{m\omega_c}[\Pi_y, \Pi_x^2]\right) \\
&= \frac{1}{2m}\left(2[x, p_x] - \frac{2}{m\omega_c}\frac{i\hbar^2}{l_B^2}\right) \\
&= 0.
\end{aligned}$$

Using a similar derivation, we can show that $[Y, H] = 0$. Since X and Y do not explicitly depend on time and have a vanishing commutator with the Hamiltonian, we can conclude that they are in fact constants of motion. Therefore, there is indeed a second quantum number m associated with the conjugate variables X and Y on which the system depends. We can make this dependence explicit in the Hamiltonian by writing it as

$$H = \hbar\omega_c(a^\dagger a + \frac{1}{2}) + \hbar\omega'(b^\dagger b + \frac{1}{2}),$$

with $\omega' \to 0$. Here, b and $b^\dagger$ are ladder operators defined by

$$b = \frac{1}{\sqrt{2}l_B}(X + iY), \qquad b^\dagger = \frac{1}{\sqrt{2}l_B}(X - iY), \quad (3.17)$$

satisfying the usual commutation relation $[b, b^\dagger] = 1$. The eigenvalue of $b^\dagger b$ is the quantum number m. Then, a state in this system is described by

$$|n, m\rangle = \frac{(a^\dagger)^n}{\sqrt{n!}}\frac{(b^\dagger)^m}{\sqrt{m!}}|0, 0\rangle. \quad (3.18)$$

The physical interpretation of this degeneracy can be made clear if we consider the uncertainty relation that follows from the commutator of X and Y. It indicates that the components of the guiding center can not be determined simultaneously, i.e., each guiding center is on average occupying some minimal surface $\Delta X \Delta Y = 2\pi l_B^2$. In each Landau level there are thus $1/2\pi l_B^2$ states per unit area available. If we rewrite this as $1/2\pi l_B^2 = eB/2\pi\hbar = B/he = B/\phi_0$, with ϕ_0 the magnetic flux quantum, we can conclude that the number of states per unit area, per Landau level, is equal to the number of flux quanta $n_B = B/\phi_0$. When we are dealing with electrons, we are dealing with fermions that obey Pauli's exclusion principle. Hence, in each state there can be only one electron (we ignore spin degeneracy here). The many-body ground state is thus formed by filling up the states, starting from the lowest-energy state. The electrons will preferably occupy the lowest Landau level, but if that level is completely filled, the electrons must start occupying the second lowest level, etc. If there are n_{el} electrons in the system, we can define the filling factor $\nu = n_{el}/n_B$, which indicates the filling of the Landau levels.

3.3.2 Gauge invariance

As we discussed before, the mechanical momentum is gauge invariant. This means that we have some freedom in choosing the gauge field $\boldsymbol{A}$, without altering the physical results. There are two choices for $\boldsymbol{A}$ that we will use, which will turn out to be convenient in different situations. The first one is the Landau gauge, which is given by

$$\boldsymbol{A}_L = B(-y, 0, 0).$$

It is convenient for a rectangular system with translational invariance in the x-direction, since this gauge matches that spatial symmetry. The other gauge we will use is the symmetric gauge, given by

$$\boldsymbol{A}_S = \frac{B}{2}(-y, x, 0).$$

It is particularly convenient for systems with a circular geometry, since this gauge is rotationally invariant.

3.3.3 Wave functions in real space representation

Now that we have established the Hamiltonian of the system, we can compute the ground-state wave function, i.e., the wave function for the lowest Landau level. We will do this for both the Landau and the symmetric gauge, in real space representation. We start off in the symmetric gauge: $\boldsymbol{A}_S = \frac{B}{2}(-y, x, 0)$. In real space, a state is represented by the wave function $\phi_{n,m}(x, y) = \langle x, y | n, m \rangle$. To derive the ground state wave function $\phi_{0,m}(x, y)$, we use the property of the ground state that it must be destroyed by the annihilation operator, i.e., $a\,\phi_{0,m}(x, y) = 0$. In the symmetric gauge, the annihilation operator defined by Eq. (3.13) reduces to:

$$\begin{aligned} a &= \frac{l_B}{\sqrt{2}\hbar}\left[p_x - \frac{eBy}{2} - i\left(p_y + \frac{eBx}{2}\right)\right] \\ &= \frac{-il_B}{\sqrt{2}\hbar}\left[\frac{eB}{2}(x - iy) + \hbar\left(\partial_x - i\partial_y\right)\right] \\ &= -i\sqrt{2}\left(\frac{1}{4l_B}z + l_B\partial_{z^*}\right), \end{aligned}$$

where we define the complex variable $z \equiv x - iy$, such that $z^* = x + iy$, opposite to conventional complex coordinates. The derivatives with respect to these complex variables are then given by $\partial_z = (\partial_x + i\partial_y)/2$ and $\partial_{z^*} = (\partial_x - i\partial_y)/2$. The real space representation of b in the symmetric gauge can be determined similarly, such that we obtain

$$\begin{aligned} a &= -i\sqrt{2}\left(\frac{1}{4l_B}z + l_B\partial_{z^*}\right), \qquad a^\dagger = i\sqrt{2}\left(\frac{1}{4l_B}z^* - l_B\partial_z\right), \\ b &= -i\sqrt{2}\left(\frac{1}{4l_B}z^* + l_B\partial_z\right), \qquad b^\dagger = i\sqrt{2}\left(\frac{1}{4l_B}z - l_B\partial_{z^*}\right). \end{aligned} \tag{3.19}$$

If we now apply the ground state condition $a\,\phi_{0,m}(z,z^*) = 0$, we find

$$\left(\frac{1}{4l_B}z + l_B\partial_{z^*}\right)\phi_{0,m}(z,z^*) = 0,$$

which yields the differential equation

$$\frac{-1}{4l_B^2}z\phi_{0,m}(z,z^*) = \partial_{z^*}\phi_{0,m}(z,z^*).$$

The z^* dependence of $\phi_{0,m}(z,z^*)$ is fixed by this equation, which allows us to write the solution for the ground-state wave function as

$$\phi_{0,m}(z,z^*) = f(z)e^{-|z|^2/4l_B^2}, \tag{3.20}$$

where $f(z)$ is an analytic function, i.e., $\partial_{z^*}f(z) = 0$. The choice of $f(z)$ is related to the degeneracy. In order to determine $f(z)$, we can use Eq. (3.18), if we have an expression for the vacuum state $|0,0\rangle$. First, we determine the wave functions for which $m = 0$. They can be calculated similarly as before, by requiring $b\phi_{n,0}(z,z^*) = 0$, which yields a similar differential equation:

$$\left(\frac{1}{4l_B}z^* + l_B\partial_z\right)\phi_{n,0}(z,z^*) = 0.$$

For $m = 0$, the wave function is of the form

$$\phi_{n,0}(z,z^*) = g(z^*)e^{-|z|^2/4l_B^2}, \tag{3.21}$$

where $g(z^*)$ is an anti-analytic function. The state $\phi_{0,0}(z,z^*)$ should obey both Eq. (3.20) and Eq. (3.21), which means that it is given by the Gaussian $e^{-|z|^2/4l_B^2}$ multiplied by a function that is both analytic and anti-analytic, which can only be a constant. That constant is fixed by normalization as $1/\sqrt{2\pi l_B^2}$. We can now use Eq. (3.18) to determine the general form of the wave function in the lowest Landau level, including the degeneracy,

$$\begin{aligned} \phi_{0,m}(z,z^*) &= \frac{(b^\dagger)^m}{\sqrt{m!}}\phi_{0,0}(z,z^*) \\ &= \left(i\sqrt{2}\right)^m\left(\frac{1}{4l_B}z - l_B\partial_{z^*}\right)^m\frac{1}{\sqrt{2\pi l_B^2 m!}}e^{-|z|^2/4l_B^2} \\ &= \frac{i^m}{\sqrt{2\pi l_B^2 m!}}\left(\frac{z}{\sqrt{2}l_B}\right)^m e^{-|z|^2/4l_B^2}. \end{aligned} \tag{3.22}$$

Hence, wave functions in the lowest Landau level are Gaussians multiplied by some power of z.

Lastly, using this wave function, we can compute the expectation value of the guiding center $\boldsymbol{R}$, by writing it in operator form using Eq. (3.15) and computing explicitly $\langle \boldsymbol{R} \rangle = \langle 0, m | \boldsymbol{R} | 0, m \rangle$. We obtain

$$\langle \boldsymbol{R} \rangle = 0, \qquad \langle |\boldsymbol{R}| \rangle = l_B \sqrt{2m+1}, \tag{3.23}$$

for the $n = 0$ Landau level. The guiding centers are positioned on circles centered at the origin, with radius $l_B\sqrt{2m+1}$. Since the symmetric gauge is suited to describe systems with a rotationally symmetric geometry, we consider a disk with an area A. We can then compute the maximal value that the quantum number m can take, because the cyclotron radius can not exceed the size of the dis. Hence m_{max} is such that the area corresponding to the cyclotron radius is equal to the area of the disk $A = \pi l_B^2 (2m_{max} + 1)$. In the thermodynamic limit, this leads to

$$m_{max} = \frac{A}{2\pi l_B^2} = N_B,$$

where N_B is the number of flux quanta. Similarly, we can derive that, for $m = 0$, the average value of the cyclotron variable is

$$R_C \equiv \langle |\boldsymbol{\eta}| \rangle = l_B \sqrt{2n+1}.$$

This quantity is denoted by R_C and is called the cyclotron radius.

Now that we have established the wave functions in the symmetric gauge, we will also determine them in the Landau gauge $\boldsymbol{A}_L = B(-y, 0, 0)$. It is appropriate to use this gauge if the sample is translationally invariant in the x-direction. In that case, $p_x = \hbar k$ is a good quantum number and we may use the plane-wave ansatz for the wave function: $\phi_{n,k}(x, y) = e^{ikx}\chi(y)$. If we write the Hamiltonian given by Eq. (3.8) in the Landau gauge, we find

$$\begin{aligned} H_L &= \frac{1}{2m}\left[(\hbar k - eBy)^2 + p_y^2\right] \\ &= \frac{p_y^2}{2m} + \frac{1}{2} m\omega_c^2 (y - y_0)^2. \end{aligned} \tag{3.24}$$

But this is just the Hamiltonian of a one-dimensional harmonic oscillator centered around the position $y_0 = l_B^2 k$. The well known eigenstates of this Hamiltonian are given in terms of the Hermite polynomials $H_n(y)$,

$$\chi_{n,k}(y) = H_n\left(\frac{y - y_0}{l_B}\right) e^{-(y-y_0)^2/2l_B^2}.$$

Note that this expression depends on k through y_0.

3.4 Integer quantum Hall effect

In the previous section, we have seen that the energy of an electron in a magnetic field is quantized in highly degenerate Landau levels, with a level spacing of $\hbar\omega_c$. Besides

these Landau levels, there are two more ingredients needed to form the quantum Hall effect. The first requirement is that the sample has boundaries, which is in practice of course always the case. We will model the boundaries by a confinement potential, which will lead to chiral edge states, as we will show. Each Landau level will contribute then one quantum of conductance to the electronic transport, which is conducted via the edge states. This will explain the quantized conductance.

The second ingredient needed to explain the plateaus in the resistivity (see Fig. 3.2) are some impurities in the sample. This gives rise to an impurity potential that will localize the electrons for partially filled Landau levels, such that they do not contribute to electronic transport. When a Landau level is filled up, there is a phase transition to the next plateau.

In the following, we will calculate the conductance of a completely filled Landau level and show that it coincides with the classical values at integer filling.

3.4.1 Conductance of a completely filled Landau level

In order to calculate the conductivity and resistivity, we consider a rectangular sample of width W and length L, such that $L \gg W$. Here, we assume that the system is translationally invariant in the x-direction, thus we impose periodic boundary conditions in the x-direction. In practice, there are usually boundaries in the sample, but as long as the length of the sample is much larger than the width, we can neglect the effects of the edges in the x-direction. Just as in the classical case, we send a current across the length of the sample and we are then interested in calculating the induced transverse Hall voltage. By determining the relation between the current and the Hall voltage, we can determine the conductance. Due to the translational invariance, the electric potential energy associated to the Hall current is independent of x, hence $U = U(y)$. Furthermore, we assume that the Landau level structure is preserved by imposing that the energy between the Landau levels is much larger than the variation of the potential over a cyclotron radius, which is proportional to l_B, as we have calculated in Eq. (3.23). Hence, we impose the condition

$$|\nabla U| \ll \frac{\hbar\omega_c}{l_B}. \tag{3.25}$$

In Section 3.3.3, we have seen that in the absence of an electric field, the Hamiltonian in the Landau gauge is that of a harmonic oscillator centered around $y_0 = kl_B^2$, thus the wave functions are peaked around this value. Since the variation in the electric potential energy that is now added to the Hamiltonian is much smaller than the Landau level spacing, we may assume that the wave functions are still roughly centered around y_0. Hence, we expand $U(y)$ up to first order around y_0,

$$\begin{aligned} U(y) &= U(y_0) + \left.\frac{\partial U}{\partial y}\right|_{y_0} (y - y_0) + \mathcal{O}\left(\frac{\partial^2 U}{\partial y^2}\right) \\ &\approx U(y_0) + eE(y_0)(y - y_0). \end{aligned} \tag{3.26}$$

If we add this expansion to the Hamiltonian in the Landau gauge, given by Eq. (3.24), we obtain the following expression by completing the square in $y - y_0$:

$$\begin{aligned} H &= \frac{p_y^2}{2m} + \frac{1}{2}m\omega_c^2(y-y_0)^2 + eE(y_0)(y-y_0) + U(y_0) \\ &= \frac{p_y^2}{2m} + \frac{1}{2}m\omega_c^2\left(y - y_0 + \frac{eE(y_0)}{m\omega_c^2}\right)^2 + U(y_0) - \frac{e^2E^2(y_0)}{m\omega_c^2} \\ &= \frac{p_y^2}{2m} + \frac{1}{2}m\omega_c^2\left(y - y_k\right)^2 + U(y_0) - \frac{e^2E^2(y_0)}{m\omega_c^2}, \end{aligned} \tag{3.27}$$

where we have defined

$$y_k = y_0 - \frac{eE(y_0)}{m\omega_c^2}.$$

According to the condition in Eq. (3.25), the second term is small in comparison to y_0, thus we may use Eq. (3.26) to write:

$$\begin{aligned} U(y_0) &= U(y_k) - eE(y_0)(y_k - y_0) \\ &= U(y_k) + \frac{e^2E^2(y_0)}{m\omega_c^2}. \end{aligned}$$

Notice that $e^2E^2/2m\omega_c^2 = mv_D^2/2$ is the kinetic energy associated to the motion of the guiding centers, which is much smaller than the total kinetic and potential energy, hence it can be neglected. We now insert the expression for $U(y_0)$ in the Hamiltonian in Eq. (3.27) and obtain

$$H = \frac{p_y^2}{2m} + \frac{1}{2}m\omega_c^2\left(y - y_k\right)^2 + U(y_k),$$

which is nothing but the Hamiltonian of a harmonic oscillator centered around y_k, shifted by a constant. The energy levels are then readily determined to be

$$\epsilon_{n,k} = \hbar\omega_c\left(n + \frac{1}{2}\right) + U(y_k). \tag{3.28}$$

Hence, the electric field shifts energy levels by the value of the electric potential at the harmonic oscillator's position.

To calculate the conductance, we consider n completely filled Landau levels and calculate the current along the x-direction,

$$I_n^x = -\frac{e}{L}\sum_k \langle n,k|v_x|n,k\rangle.$$

The expectation value of $v_x = \dot{x}$ can be calculated using the Heisenberg equations of motion:

$$i\hbar\dot{x} = [x,H] = \frac{\partial H}{\partial p_x}[x,p_x] = i\frac{\partial H}{\partial k},$$

where we used $p_x = \hbar k$. Hence,

$$\langle n,k|v_x|n,k\rangle = \frac{1}{\hbar}\frac{\partial\epsilon_{n,k}}{\partial k} \approx \frac{1}{\hbar}\frac{\Delta\epsilon_{n,k}}{\Delta k} = \frac{L}{2\pi\hbar}(\epsilon_{n,k+1} - \epsilon_{n,k}),$$

where the approximation is valid if $\Delta k = 2\pi/L$ is small. With this, we can now calculate the current carried by the n-th Landau level,

$$\begin{aligned} I_n^x &= -\frac{e}{L}\sum_k \frac{L}{h}(\epsilon_{n,k+1} - \epsilon_{n,k}) \\ &= -\frac{e}{h}(\epsilon_{n,k_{max}} - \epsilon_{n,k_{min}}), \end{aligned}$$

where $h = 2\pi\hbar$. We can observe that all the intermediate energies cancel out and the current only depends on the energies at the edges. The difference of those energies is given by $-eV$, where V is the voltage that generates the current, such that

$$I_n^x = \frac{e^2}{h}V. \tag{3.29}$$

Therefore, each Landau level contributes one quantum of conductance $G_0 = e^2/h$ to the current. The total Hall conductance of n filled Landau levels (which is thus a transverse conductance) is then

$$G_H = n\frac{e^2}{h}.$$

It will turn out that this electronic transport is ballistic, meaning that the transmission of electrons is perfect, i.e., no electrons are back-scattered. Since there is no current in the y-direction, the longitudinal conductance is zero and we obtain for the conductance and resistance matrices (which are each others inverses):

$$G = \begin{pmatrix} 0 & G_H \\ -G_H & 0 \end{pmatrix}, \qquad R = \begin{pmatrix} 0 & -R_H \\ R_H & 0 \end{pmatrix},$$

where $R_H = h/e^2 n$ is the Hall resistance. In the classical picture we found for the transverse resistivity:

$$\rho_H = \frac{B}{en_{el}} = \frac{B}{en_B\nu} = \frac{h}{e^2}\frac{1}{\nu},$$

where we used $\nu = n_{el}/n_B$ and $n_B = eB/h$. This coincides exactly with the classical picture (3.7) at integer filling, i.e., for $\nu = n$ integer.

3.4.2 Impurity and confinement potentials

So far, we have seen that two-dimensional electrons in a perpendicular magnetic field have quantized energy levels and in the presence of an electric field, which is perpendicular to the magnetic field, the system produces a Hall voltage that is transverse to the current. We have shown that for completely filled Landau levels, the resistivity matches the classical case. There are, however, two more ingredients needed to describe the quantum Hall effect completely, including the behavior of the system at fractional filling of the Landau levels. Firstly, the edges of the sample, which can be modeled by a confinement potential, will give rise to edge states. These edge states carry the current we have calculated in the previous section without dissipation. Furthermore, for the quantum Hall effect to arise, there must be some impurity in the sample. The impurities give rise to an impurity potential, which localizes the electrons, preventing them to contribute to the

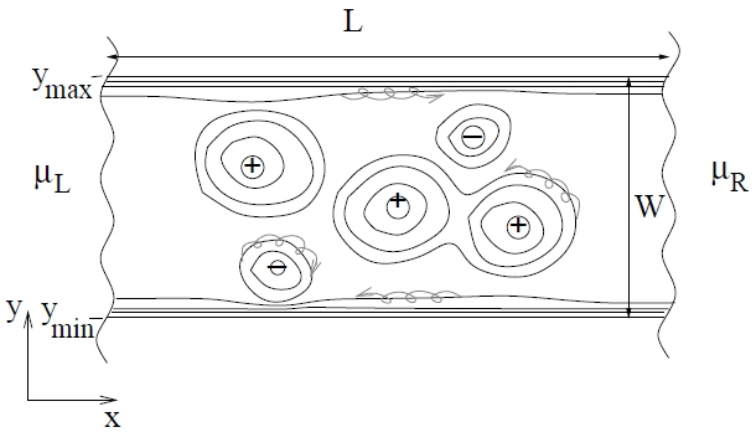

Figure 3.5: Potential lines of the impurity potential in the sample. In the semi-classical picture, electrons follow the potential lines in a spiraling motion. At the edges, the confinement potential dominates and forms straight potential lines. Figure from Ref. [11]

macroscopic, electric current. This eventually leads to the plateaus in the resistance, on which we will elaborate in the next section.

Firstly, we will consider the impurity potential $V_{\text{imp}}(\boldsymbol{r})$. We assume that it is slowly varying in space, such that the characteristic length scale on which it varies is large compared to the magnetic length l_B. This will ensure the condition (3.25) to preserve the Landau level structure is satisfied. An example of such a potential is shown in Fig. 3.5. It consists of potential hills and valleys enclosed by equipotential lines, comparable to a landscape with mountains and valleys. This potential breaks the translational invariance in both directions, hence the degeneracy associated with the position of the guiding centers is lifted. Therefore, the guiding centers are not constants of motion anymore, since they do not commute with the Hamiltonian now and thus acquire dynamics:

$$i\hbar\dot{X} = [X, H] = [X, U_{\text{imp}}(X, Y)] = \frac{\partial U_{\text{imp}}}{\partial Y}[X, Y] = il_B^2 \frac{\partial U_{\text{imp}}}{\partial Y},$$
$$i\hbar\dot{Y} = [Y, H] = [Y, U_{\text{imp}}(X, Y)] = \frac{\partial U_{\text{imp}}}{\partial X}[Y, X] = -il_B^2 \frac{\partial U_{\text{imp}}}{\partial X},$$

where we used Eqs. (3.10) and (3.16). The potential energy $U_{\text{imp}} = -eV_{\text{imp}}$ is related to the electric field by $-e\boldsymbol{E}_{\text{imp}} = -\nabla U_{\text{imp}}$, thus we can rewrite these equations as

$$\dot{\boldsymbol{R}} = \frac{1}{eB}\frac{(\nabla U_{\text{imp}}) \times \boldsymbol{B}}{B} = \frac{\boldsymbol{E}_{\text{imp}} \times \boldsymbol{B}}{B^2} = v_D,$$

which shows that the velocity of the guiding centers is indeed the Hall drift velocity as defined in Eq. (3.5). Since $v_D \perp \nabla V_{\text{imp}}$, this result agrees with the classical picture of guiding centers moving along the equipotential lines of the potential. Notice that, if the equipotential line along which an electron moves is closed, the electron is localized and does not contribute to macroscopic electronic transport. This is a key feature of the quantum Hall effect, which causes the formation of plateaus in the resistivity (see Section 3.4.3), although the localization of the electrons is purely a classical effect.

Next, we consider a rectangular sample in the xy-plane and we assume for now that the system is translationally invariant in the x-direction. The sample has boundaries in the y-direction, which can be modeled by a confinement potential $V_{\text{conf}}(y)$. This potential is

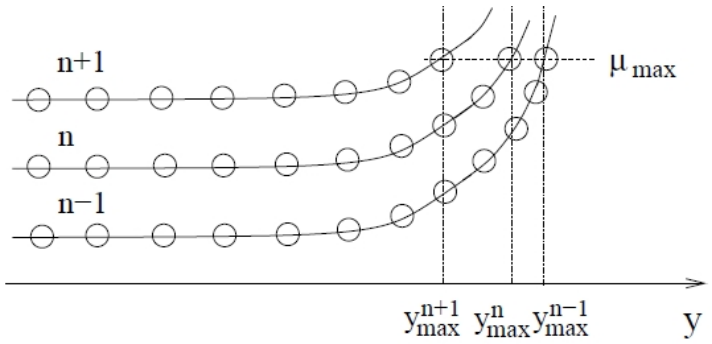

Figure 3.6: Landau levels bend upwards near the edges due to the confinement potential in the y-direction. Figure from Ref. [11]

strongly varying near the boundaries, thus we can not right away apply the semi-classical arguments just mentioned. However, in order to be able to account for this potential in the Hamiltonian, we can use the method of Section 3.4.1 and expand it around $y_0 = kl_B^2$. As indicated in Eq. (3.28), the energy levels are then shifted by the potential energy at the guiding center's position,

$$\epsilon_{n,k} = \hbar\omega_c \left(n + \frac{1}{2}\right) + U_{\text{conf}}(y_0).$$

Hence, the Landau levels follow the confinement potential and bend upwards near the boundaries of the sample, as shown in Fig. 3.6. Notice that here, y_0 corresponds to the position of the guiding center and this results is thus in agreement with the semi-classical picture we had before. Near the edges, the equipotential lines of the confinement potential are stretched out along the edge. The electrons that occupy the states on those lines can travel thus along the length of the sample and contribute to electronic transport. These states are called edge states. From the definition of the Hall drift velocity $v_D = \frac{1}{B^2}(\nabla V_{\text{conf}}) \times \boldsymbol{B}$, we can see that the electrons in the edge states move indeed in the x-direction and electrons on the opposite edges move in opposite directions, where the direction is imposed by the gradient of the confinement potential. Since electrons on one edge move all in the same direction, they are chiral. Even if they would scatter to another nearby edge state, they would keep moving in the same direction. The only way to change the direction of the electrons is if they would be able to scatter to edge states on the other side of the sample. However, the edges are usually too far apart for this to happen, thus the conduction of electrons at the edges is ballistic. This leads to the somewhat peculiar situation of a insulating bulk with perfectly conducting edge states.

3.4.3 Occurrence of plateaus in the resistivity

So far, we have derived the Hall resistance at integer filling of the Landau levels, but we have not yet explained the plateaus in the resitivity that form around the integer filling factors. In order to do this, we resort to the so-called percolation picture.

If we start off with n completely filled Landau levels, as shown in Fig. 3.7a, the transverse resistance is $R_H = h/e^2 n$ and the longitudinal resistance is zero, as we have seen before. Now, if we decrease the magnetic field slightly, as in Fig. 3.7b, the number of states per Landau level decreases and some of the electrons are forced to populate the next Landau level. When they do so, they prefer to occupy the states on the equipotential

lines of the lowest valley of the potential. The next electron will then occupy the next lowest potential line. We can picture this by imagining a 'sea' in a mountain landscape, where the sea level operates as the filling factor. If the sea level is low, the water will sit in the lowest valleys and will form small lakes. If the sea level is slightly higher, the water in the lakes rises and when the sea level increases further, some lakes may merge into one big lake. At some point, if the sea level increases even more, the water will stretch out over the whole landscape. This is precisely what happens with the 'sea' of electrons in the sample during the transition between the plateaus. As the filling is increased, the electrons start occupying the valleys of the potential. Since they are localized, they do not contribute to macroscopic, electronic transport and thus the resistance remains the same as in a completely filled Landau level. If we increase the filling even further, at some point, the puddles of electrons stretch across the sample and electrons in edge states on one end of the sample can now dissipate to the other edge via the potential lines (see Fig 3.7c). The point of percolation depends on the impurity potential and can be different in each sample. At that point, there is a macroscopic current carried by the edge states which are now extended across the sample. Hence, the resistance is no longer quantized and follows the classical curve to the next plateau. Furthermore, since the edge states are now close to each other (see Fig. 3.8), the electrons can tunnel from one edge state to the other. This backscattering causes the longitudinal resistance to become finite. The percolation transition happens at the peak in the density of states and if the filling is then increased further, the same reasoning applies to holes instead of particles. Hence, the puddles of electrons will then reduce to localized states again and eventually we end up with $n+1$ edge states and a resistance that is quantized as $h/e^2(n+1)$.

To summarize the conclusions from this chapter, we have seen that the confinement potential leads to chiral edge states, in which the electrons move without dissipation. The impurity potential localizes some of the electrons at filling factors near an integer value. At the transition to the next Landau level, the electrons in the bulk are spread out across the sample and dissipation can occur in the edge states. Hence, there is a peak in the longitudinal resistance at the transition where the electrons are flooding into the next Landau level and the Hall resistance shifts towards the next plateau. This explains the integer quantum Hall effect.

3.5 Fractional quantum Hall effect

As mentioned already in the introduction, these plateaus in the resistivity do not only occur at integer filling, but there are also numerous plateaus observed at fractional filling, mainly in the lowest Landau levels. The first time that this fractional quantum Hall effect (FQHE) was observed in 1982, the Hall resistance was found to be quantized for a filling $\nu = 1/3$ with a corresponding resistance $R_H = h/e^2\nu = 3h/e^2$ [12]. The discovery of this phenomenon was quite a surprise, because in between two Landau levels, there is no gap that can lead to the formation of these plateaus via the mechanism of the IQHE. Remember that for the IQHE a Landau level is completely filled, such that an additional electron is forced to occupy the next Landau level due to the Pauli principle. There is a finite energy gap of $\Delta E = \hbar\omega_c$ between the Landau levels. The system is thus said to be incompressible, since you cannot change the filling factor by only adding an infinitesimal amount of energy. However, for a fractionally filled Landau level, there is nothing that prevents an extra electron to occupy the same Landau level. In fact, at

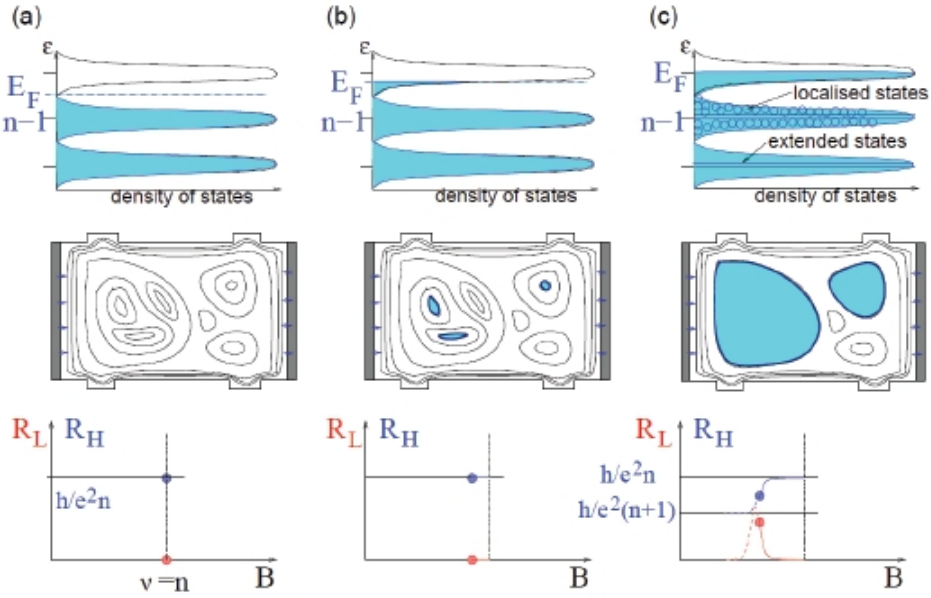

Figure 3.7: a) The first n Landau levels are completely filled. b) Upon decreasing the magnetic field electrons start populating the next Landau level (upper image) and localize in the valleys of the impurity potential (middle image). Since they do not contribute to electronic transport, the Hall resistance remains quantized at h/e^2n (lower image). c) Upon increasing the magnetic field further, the edge states percolate and extend across the sample (middle image). The Hall resistance drops, following the classical value, while the longitudinal resistance peaks due to backscattering (lower image). Figure from Ref. [11]

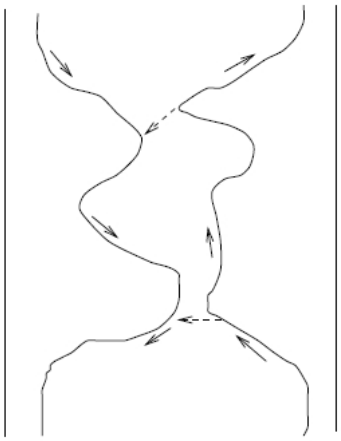

Figure 3.8: The solid arrows indicate the edge states which extend across the sample. Since they are close together, electrons can tunnel from one edge state to the other, as indicated by the dashed arrows. Figure from Ref. [9]

first sight there is nothing that makes a filling of, say, $\nu = 1/3$ special, thus why would the quantum Hall effect occur at this fraction? The answer lies in the fact that we have ignored the interaction between the electrons until now. If a Landau level is fractionally filled, all electrons in that level have the same kinetic energy. It is precisely therefore that the Coulomb interaction between the electrons becomes relevant for describing the low-energy electronic properties. Since we are then dealing with a system of strongly correlated electrons, perturbation theory is useless, thus we must resort to other methods.

The first method that was proposed to deal with the FQHE came from Laughlin in 1983 [13]. He postulated a trial wave function for filling factors $\nu_L = 1/(2s+1)$, with s an integer, based on only a few symmetry arguments. This wave function represents an incompressible quantum liquid. Incompressibility is required for the FQHE because an essential ingredient for Hall quantization is the presence of a gap to the next excited state. Being only an 'educated guess', this wave function miraculously turned out to be very accurate and have a high overlap with exact wave functions calculated for small systems [19]. Laughlin's wave function was originally constructed for the lowest Landau level, but it can easily be generalized to higher ones [20]. In Section 3.5.1, we will elaborate on the arguments Laughlin used to construct this wave function and explain the so-called plasma analogy, which relates Laughlin's incompressible quantum liquid to a classical 2D one-component plasma.

Another approach for the FQHE, which was designed by Jain short after Laughlin, was the introduction of composite fermions. Whereas Laughlin's wave function only holds for filling factors $\bar{\nu} = 1/(2s+1)$, Jain's composite fermion (CF) description can explain the FQHE for filling factors $\bar{\nu} = p/(2ps+1)$. In Section 3.5.2, we will shortly explain the ideas of CF theory. For a more detailed description we refer to the literature [14, 15, 21].

3.5.1 Laughlin's incompressible quantum liquid

In order to demonstrate Laughlin's trial wave function, we first recall the one-particle wave function in the lowest Landau level which we derived in Eq. (3.22) in the symmetric gauge,

$$\phi_{0,m}(z, z^*) \sim z^m e^{-|z|^2/4l_B^2}.$$

Consider then an arbitrary two-particle wave function in the lowest Landau level. It must also be analytic in both coordinates z_1 and z_2, such that it can be written as a linear combination of the basis states, which are given up to some normalization constant by

$$\psi^{(2)}(z_1, z_2) = (z_1 + z_2)^M (z_1 - z_2)^m e^{-(|z_1|^2+|z_2|^2)/4},$$

where m, and M are integers, associated to the relative and total angular momentum respectively. Furthermore, we have absorbed l_B in z_1 and z_2. Because electrons are fermions, the wave function must be anti-symmetric under exchange of particles. Since

$$\begin{aligned}\psi^{(2)}(z_2, z_1) &= (z_1 + z_2)^M (z_2 - z_1)^m e^{-(|z_1|^2+|z_2|^2)/4} \\ &= (-1)^m \psi^{(2)}(z_1, z_2),\end{aligned}$$

this implies that m must be odd. The two-particle wave function can be generalized to the full many-body wave function [11],

$$\psi_m^L(\{z_i\}) = \prod_{k<l} (z_k - z_l)^m e^{-\sum_j |z_j|^2/4}, \tag{3.30}$$

where $\{z_i\} = (z_1, z_2, \cdots, z_N)$. Notice that there is no center-of-mass dependence, i.e., $M = 0$, because a non-zero value for M would break the continuous spatial symmetry. This wave function in the lowest Landau level can be generalized to higher Landau levels as well, e.g. by using Eq. (3.18).

In principle, Laughlin's wave function is a variational wave function, with m its variational parameter. Minimizing the energy eigenvalue of ψ_m^L with respect to m would yield its correct value. However, m is in fact completely determined by the filling of the lowest Landau level. To see this, consider the explicit dependence of the wave function on some arbitrary coordinate, say, z_1,

$$\psi_m^L(z_1) = f(z_2, \cdots, z_N)(z_1 - z_2)^m (z_1 - z_3)^m \cdots (z_1 - z_N)^m e^{-\sum_j |z_j|^2/4}.$$

Since there are $N - 1$ factors of $(z_1 - z_i)$ in the product, this implies that the highest power with which z_1 occurs is $m(N - 1)$. In Section 3.3.3, we have seen that this highest power is fixed by the number of flux quanta N_B in a Landau level. Hence $m(N-1) = N_B$, and in the thermodynamic limit, we thus have a relation that fixes m at

$$m = \frac{N_B}{N} = \frac{1}{\nu}.$$

Since m must be odd, $\nu = 1/(2s + 1)$, for some positive integer s. At these filling factors, the wave function in the lowest Landau level is thus described by Eq. (3.30), with $m = 2s + 1$.

There is a striking analogy between Laughlin's quantum liquid and a classical two-dimensional one-component plasma, invented by Laughlin himself. Consider the square of the absolute value of the wave function $|\psi_M^L|^2$. As known from quantum mechanics, this represents a probability distribution. Laughlin identified this with a probability distribution from classical mechanics: the Boltzmann factor. Hence,

$$e^{-\beta U_{cl}} = \prod_{k<l} |z_k - z_l|^{2m} e^{-\sum_j |z_j|^2/2}.$$

Here, β does not represent temperature (the quantum liquid is at T=0 anyway) like in the classical case, but is rather some formal parameter which we will set equal to $2/q$. If we put $m = q$, we obtain

$$U_{cl} = -q^2 \sum_{k<l} |z_k - z_l| + q \sum_j |z_j|^2/4.$$

This is exactly the energy of a two-dimensional one-component plasma of interacting particles with charge q in a neutralizing background. The first term in the above-mentioned energy describes the interactions between the particles, while the interaction with the background is given by the second term. Hence, we can translate well-known properties of a classical system to this exotic and less explored quantum liquid.

3.5.2 Composite fermions

The description given by Laughlin, however accurate, was not sufficient to describe all the fractional quantum Hall states. It only holds for filling factors of the form $\bar{\nu} = 1/(2s+1)$, with s an integer. In 1989, Jain proposed a description that could explain all states

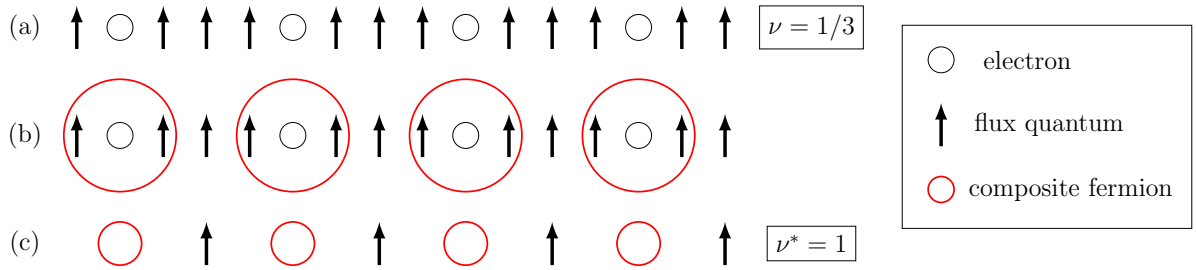

Figure 3.9: (a) $\nu = 1/3$. There is one electron for each three flux quanta. (b) Two flux quanta, together with one electron form a composite fermion (CF). (c) There is now one flux quantum for each CF. This corresponds to a CF filling $\nu^* = 1$.

with filling factor $\bar{\nu} = p/(2ps+1)$, with p and s integers, in terms of so-called composite fermions [14]. Remember that the filling factor is the ratio between the electron density and the magnetic flux density, such that for these filling factors there are $2ps+1$ flux quanta for each p electrons. In the model proposed by Jain, each electron forms a composite fermion (CF) together with $2s$ flux quanta. For each p CFs there is then one residual flux quantum. With this we can define a CF filling factor $\bar{\nu}^* = n_{CF}/n_B^*$. This describes the filling of the effective CF Landau levels (also called Λ-levels). The gap to the next Λ-level is then determined by the Coulomb energy. The CF filling factor can be written in terms of the original flux density as $n_B^* = n_B - 2sn_{el}$. This then defines an effective magnetic field B^* that acts on the CFs,

$$B^* = B - 2s\phi_0 n_{el} = B(1 - 2s\bar{\nu}) \tag{3.31}$$

An electron filling of $\bar{\nu} = p/(2ps+1)$ thus corresponds with a CF filling of $\bar{\nu}^* = p$. Therefore, the FQHE of electrons maps into an IQHE of CFs. Note that the electrons do not actually bind to the flux quanta somehow, but it is just a model that maps a complicated situation of a fractionally filled Landau level to the situation of some effective Landau level completely filled with CFs such that we can apply the familiar theory from the IQHE. To illustrate this construction, Fig. 3.9 shows an example for the state $\nu = 1/3$.

Chapter 4

Graphene

Ever since its experimental realization, graphene has been of great interest to scientists all over the world. The one-atom thick layer of carbon atoms arranged in a honeycomb lattice was first isolated by Geim and Novoselov in 2004, for which they received the Nobel Prize in 2010. It has enjoyed much attention outside the scientific world as well, due to the fascinating physics it discloses and the myriad of potential applications. Examples of such applications include flexible display screens, electronic circuits and energy storage. Due to its huge mechanical strength, high electron mobility, and its lightweight structure, graphene might also be used to manufacture new kinds of materials that could be used for example in biomedical sciences [22].

Besides the technological applications it may be used for, graphene is also of great interest to theoretical physicists. One of the peculiar features of graphene is that the electrons behave as if they were massless, relativistic particles. They have the same linear dispersion, which was first calculated by Wallace in 1947 [23]. This has led to the emergence of a new field of physics, bridging the gap between condensed-matter and high-energy physics. Those quantum relativistic phenomena are usually very difficult, if not impossible, to observe in high-energy physics, but with graphene those phenomena can now be mimicked and observed on table-top experiments. Furthermore, graphene is a realization of a two-dimensional electron system, thus it can serve as an example to study the relatively new field of low-dimensional materials, which exhibit all kinds of exotic phenomena.

In this section, we will explain the lattice model of graphene, derive its famous linear dispersion relation and elaborate on Landau quantization and the quantum Hall effect in graphene.

4.1 Crystal structure of graphene

In this section, we will introduce the crystal structure of graphene and elaborate on how the carbon atoms hybridize, forming graphene's characteristic honeycomb lattice.

4.1.1 Hybridization

The carbon atom has six electrons. In the ground state, these electrons are in the $1s^2 2s^2 2p^2$ configuration. This means that two electrons are in the $1s$ orbital, which is close to the nucleus and has the lowest energy. These electrons are tightly bound and do therefore not influence the electronic properties significantly. The other four electrons

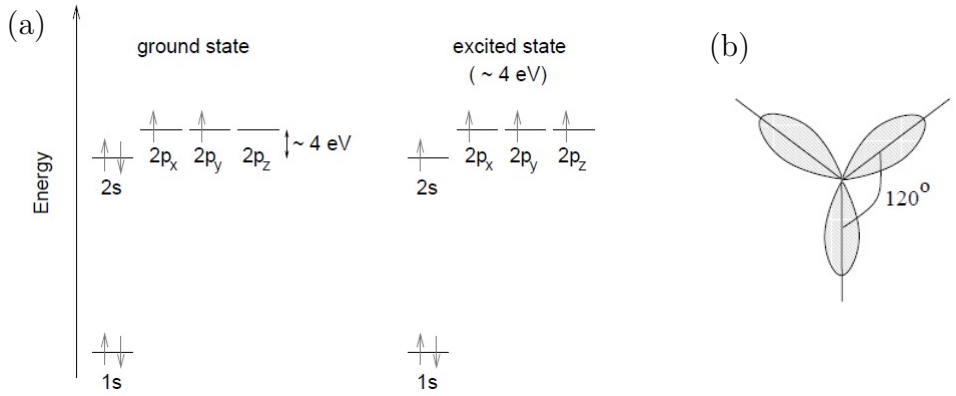

Figure 4.1: (a) Electronic orbitals for the carbon atom in the ground state and the excited state. (b) sp^2 hybridization. Figure from Ref. [24]

are distributed over the $2s$ and $2p$ orbitals. Two electrons are in in the $2s$ orbital, which is 4 eV lower in energy than the three equivalent $2p_x$, $2p_y$ and $2p_z$ orbitals. The remaining two electrons are in two of those three $2p$ orbitals. In the presence of other carbon atoms, it might be favorable to excite one of the electrons in the $2s$ orbital to the third $2p$ orbital, as depicted in Fig. 4.1. In this excited state, the electrons can form a quantum-mechanical superposition of a $2s$ state with n of these $2p$ state (for $n = 1, 2, 3$). In graphene, the electrons hybridize into sp^2 states, meaning that the $2s$-electron form a quantum-mechanical superposition with two of the three $2p$ states, say, p_x and p_y. The hybridized orbitals are all in the xy-plane and are rotated over an angle of 120° with respect to each other. Due to the strong overlap of these electrons with the ones of neighboring carbon atoms, in what we call σ-bonds, these electrons are fixed at their positions. The fourth electron is in the remaining p_z-orbital, perpendicular to the plane. This electron is responsible for the electronic properties in graphene.

4.1.2 The lattice

As we have seen, graphene consists of a single layer of carbon atoms arranged in a honeycomb lattice. Since such a configuration can not be constructed with just two primitive lattice vectors, the honeycomb lattice is not a Bravais lattice. We can, however, view the honeycomb lattice as two interpenetrating triangular sublattices (see Fig. 4.2a). Equivalently, this can be modeled as one triangular lattice with two atoms in the unit cell: one of each sublattice. Since the triangular lattice is indeed a Bravais lattice, we can construct the two primitive lattice vectors as

$$\boldsymbol{a}_1 = \sqrt{3}a\hat{x}, \qquad \boldsymbol{a}_2 = \frac{\sqrt{3}a}{2}\left(\hat{x} + \sqrt{3}\hat{y}\right), \tag{4.1}$$

where $a = 0.142\,\text{nm}$ is the distance between two neighboring carbon atoms. In Fig. 4.2a, we also denoted the three vectors connecting the atoms of sublattice A to their nearest neighbors on sublattice B. They are given by

$$\boldsymbol{\delta}_1 = \frac{a}{2}\left(\sqrt{3}\hat{x} + \hat{y}\right), \qquad \boldsymbol{\delta}_2 = \frac{a}{2}\left(-\sqrt{3}\hat{x} + \hat{y}\right), \qquad \boldsymbol{\delta}_3 = -a\hat{y}. \tag{4.2}$$

Note that the two sublattices are completely equivalent and there is no physical distinction between them. Given the two lattice vectors in Eq. (4.1), we can now determine the

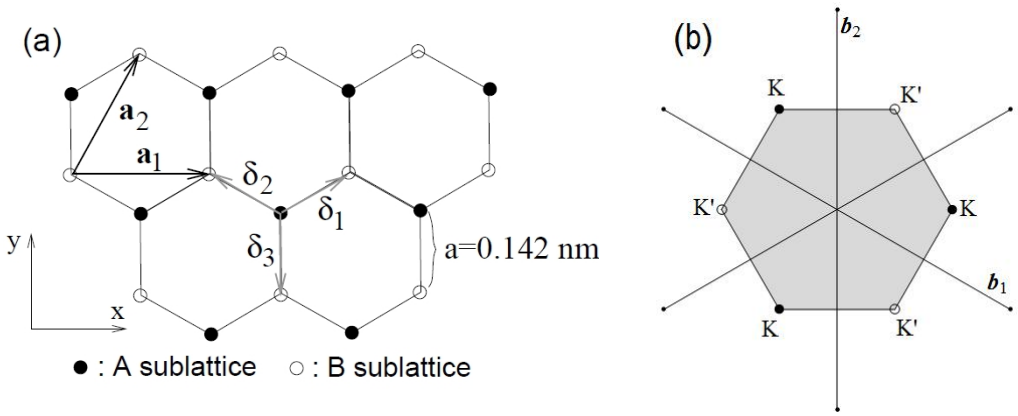

Figure 4.2: (a) The crystal structure of graphene is a honeycomb lattice consisting of two equivalent triangular sublattices, with $\boldsymbol{a}_1$ and $\boldsymbol{a}_2$ its primitive lattice vectors. Figure from Ref. [24]. (b) Reciprocal space with $\boldsymbol{b}_1$ and $\boldsymbol{b}_2$ the reciprocal lattice vectors. The gray area is the first Brillouin zone. It has two inequivalent points K and K'.

reciprocal lattice vectors straightforwardly,

$$\boldsymbol{b}_1 = \frac{2\pi}{\sqrt{3}a}\left(\hat{x} - \frac{1}{\sqrt{3}}\hat{y}\right), \qquad \boldsymbol{b}_2 = \frac{4\pi}{3a}\hat{y}.$$

They span a triangular lattice in reciprocal space. We can then construct the first Brillouin zone, that is, the set of all points in reciprocal space that cannot be connected with one another by reciprocal lattice vectors. It is pictured by the shaded hexagonal region in Fig. 4.2b. Of the six corners of the Brillouin zone, there are two inequivalent points K and K', and the other four are equivalent to either one of them. Note that K and K' are inequivalent because the vector that connects them is not a reciprocal lattice vector. This inequivalence is a property of the triangular Bravais lattice and is irrespective of the number of atoms in the unit cell. The K and K' points are given by

$$K = \frac{4\pi}{3\sqrt{3}a}\hat{x}, \qquad K' = -\frac{4\pi}{3\sqrt{3}a}\hat{x}. \tag{4.3}$$

The other corners can then be constructed as $K^{(\prime)} + u_1\boldsymbol{b}_1 + u_2\boldsymbol{b}_2$, for some integers u_1 and u_2.

4.2 Dispersion in graphene

One of the remarkable features of graphene is that its electrons near the Fermi level have a linear dispersion, just like free relativistic electrons. In this section, we will use a tight-binding Hamiltonian to model the behavior of the electrons and subsequently we will derive the dispersion relation. We will follow the derivation that Wallace performed originally in 1947 [23].

Remember that three of the electrons in the carbon atom are hybridized in strong σ-bonds and do not contribute to the electronic properties, since they have energies far away from the Fermi level [25]. The only electrons that are relevant for the low energy excitation are the p_z-electrons, of which there is one on each lattice site. We can model the wave functions of these electrons using a tight-binding model. Tight-binding

models are useful in the description of electrons which are tightly bound to their atomic core, where the local orbital wave function dominates. They behave almost like isolated electrons. However, the wave functions can overlap due to the closeness of the electrons on neighboring lattice sites. The tight-binding model includes a correction for this, in order to accurately describe the behavior of the electrons. Naturally, the effects of these overlaps are the greatest for electrons close to each other and therefore we only consider the influence of nearest- and next-nearest-neighbors initially. Later on, we will even ignore the next-nearest-neighbor interactions, since they will turn out to be about ten times smaller than the nearest-neighbor interactions.

To start off, we can write the total wave function in terms of wave functions of the two sublattices A and B [24],

$$\psi_{\boldsymbol{k}}(\boldsymbol{r}) = a_{\boldsymbol{k}}\psi_{\boldsymbol{k}}^{(A)} + b_{\boldsymbol{k}}\psi_{\boldsymbol{k}}^{(B)}. \tag{4.4}$$

The wave functions on both sublattice are then assumed to be a linear combination of the atomic orbital wave functions of all the electrons on that particular sublattice. According to Bloch's theorem, the wave function of a particle in a periodic potential can be written as $e^{i\boldsymbol{k}\cdot\boldsymbol{r}}u_{\boldsymbol{k}}(\boldsymbol{r})$, where $u_{\boldsymbol{k}}(\boldsymbol{r})$ is some function which exhibits the same periodicity as the potential [26]. Hence, we can write the wave functions on the individual sublattices as

$$\psi_{\boldsymbol{k}}^{(j)} = \sum_{\boldsymbol{R}_l} e^{i\boldsymbol{k}\cdot\boldsymbol{R}_l}\,\phi^{(j)}(\boldsymbol{r} + \boldsymbol{\delta}_j - \boldsymbol{R}_l),$$

where the sum runs over all Bravais lattice sites $\boldsymbol{R}_l$ and $\phi^{(j)}(\boldsymbol{r} + \boldsymbol{\delta}_j - \boldsymbol{R}_l)$ is the atomic orbital wave function in the vicinity of the atom at position $\boldsymbol{R}_l - \boldsymbol{\delta}_j$ at sublattice j. We choose the Bravais lattice to coincide with the A-sublattice, such that $\boldsymbol{\delta}_A = 0$ and $\boldsymbol{\delta}_B$ is a vector that connects the two sublattices, which we choose to be equal to $\boldsymbol{\delta}_3$, as defined in Eq. (4.2).

In the tight-binding model, the Hamiltonian is assumed to take the form

$$H = H^a + \Delta V, \tag{4.5}$$

where H^a is the atomic orbital Hamiltonian [24]. It satisfies the eigenvalue equation

$$H^a\,\phi^{(j)}(\boldsymbol{r}) = \epsilon_0\,\phi^{(j)}(\boldsymbol{r}).$$

Here, ϵ_0 is the atomic orbital energy which is the same for both sublattices, since all the electrons are in p_z-orbitals. Hence, ϵ_0 just shifts the total energy by a constant and is therefore not physically relevant and we will set it to zero for convenience. Furthermore, in Eq. (4.5), ΔV is the potential that arises due to the presence of all other atoms. We now wish to solve the Schrödinger equation

$$H\psi_{\boldsymbol{k}} = \epsilon_{\boldsymbol{k}}^{\lambda}\,\psi_{\boldsymbol{k}},$$

where λ indicates the different solutions for the energy. Multiplying both sides of this equation on the left with $\psi_{\boldsymbol{k}}^*$, integrating over space and substituting Eq. (4.4), we get, in matrix notation,

$$\begin{pmatrix} a_{\boldsymbol{k}}^* & b_{\boldsymbol{k}}^* \end{pmatrix} \mathcal{H}_{\boldsymbol{k}} \begin{pmatrix} a_{\boldsymbol{k}} \\ b_{\boldsymbol{k}} \end{pmatrix} = \epsilon_{\boldsymbol{k}}^{\lambda} \begin{pmatrix} a_{\boldsymbol{k}}^* & b_{\boldsymbol{k}}^* \end{pmatrix} \mathcal{S}_{\boldsymbol{k}} \begin{pmatrix} a_{\boldsymbol{k}} \\ b_{\boldsymbol{k}} \end{pmatrix}, \tag{4.6}$$

where the Hamiltonian matrix and overlap matrix are given by

$$\mathcal{H}_{\boldsymbol{k}} = \int \mathrm{d}\boldsymbol{r} \begin{pmatrix} \psi_{\boldsymbol{k}}^{*(A)} H \psi_{\boldsymbol{k}}^{(A)} & \psi_{\boldsymbol{k}}^{*(A)} H \psi_{\boldsymbol{k}}^{(B)} \\ \psi_{\boldsymbol{k}}^{*(B)} H \psi_{\boldsymbol{k}}^{(A)} & \psi_{\boldsymbol{k}}^{*(B)} H \psi_{\boldsymbol{k}}^{(B)} \end{pmatrix}, \quad \mathcal{S}_{\boldsymbol{k}} = \int \mathrm{d}\boldsymbol{r} \begin{pmatrix} \psi_{\boldsymbol{k}}^{*(A)} \psi_{\boldsymbol{k}}^{(A)} & \psi_{\boldsymbol{k}}^{*(A)} \psi_{\boldsymbol{k}}^{(B)} \\ \psi_{\boldsymbol{k}}^{*(B)} \psi_{\boldsymbol{k}}^{(A)} & \psi_{\boldsymbol{k}}^{*(B)} \psi_{\boldsymbol{k}}^{(B)} \end{pmatrix}.$$

Notice that we are working with non-orthogonal wave functions, which means that the off-diagonal terms in the overlap matrix do not necessarily vanish. By inserting the explicit expressions for H and $\psi_{\boldsymbol{k}}^{(j)}$, we can compute the matrix elements of the Hamiltonian matrix as follows,

$$\begin{aligned} \mathcal{H}_{\boldsymbol{k}}^{ij} &= \int \mathrm{d}\boldsymbol{r} \sum_{\boldsymbol{R}_l} \sum_{\boldsymbol{R}_m} e^{-i\boldsymbol{k}\cdot(\boldsymbol{R}_l - \boldsymbol{R}_m)}\, \phi^{(i)*}(\boldsymbol{r} + \boldsymbol{\delta}_i - \boldsymbol{R}_l) \Delta V \phi^{(j)}(\boldsymbol{r} + \boldsymbol{\delta}_j - \boldsymbol{R}_m) \\ &= \int \mathrm{d}\boldsymbol{r} \sum_{\boldsymbol{R}_l} \sum_{\boldsymbol{R}_m} e^{-i\boldsymbol{k}\cdot(\boldsymbol{R}_l - \boldsymbol{R}_m)}\, \phi^{(i)*}(\boldsymbol{r} + \boldsymbol{\delta}_i) \Delta V \phi^{(j)}(\boldsymbol{r} + \boldsymbol{\delta}_j + \boldsymbol{R}_l - \boldsymbol{R}_m) \\ &= N \int \mathrm{d}\boldsymbol{r} \sum_{\boldsymbol{R}_l} e^{i\boldsymbol{k}\cdot\boldsymbol{R}_l}\, \phi^{(i)*}(\boldsymbol{r} + \boldsymbol{\delta}_i) \Delta V \phi^{(j)}(\boldsymbol{r} + \boldsymbol{\delta}_j - \boldsymbol{R}_l), \end{aligned} \tag{4.7}$$

where we made the substitution $\boldsymbol{r} \to \boldsymbol{r} + \boldsymbol{R}_l$ in the second line, such that we were able to evaluate one of the sums in the third line. Consider first the off-diagonal term $\mathcal{H}_{\boldsymbol{k}}^{AB}$. Remember that $\boldsymbol{\delta}_A = 0$ and $\boldsymbol{\delta}_B = \boldsymbol{\delta}_3$. Since we only consider nearest- and next-nearest-neighbor interactions, the summation over $\boldsymbol{R}_l$ is now restricted to those sites on the B-sublattice which are the nearest neighbors of a site on the A-sublattice. Notice that its next-nearest neighbors are located on the A-sublattice. The three nearest neighbors of an electron on the A-sublattice are given by the translations $\boldsymbol{\delta}_i$ defined in Eq. (4.2), for $i = 1, 2, 3$. Hence, $\boldsymbol{R}_l$ runs over the three vectors $\boldsymbol{\delta}_3 - \boldsymbol{\delta}_1 = -\boldsymbol{a}_2$, $\boldsymbol{\delta}_3 - \boldsymbol{\delta}_2 = -\boldsymbol{a}_3$ and $\boldsymbol{0}$. Here, we have defined $\boldsymbol{a}_3 \equiv -\frac{\sqrt{3}a}{2}\left(\hat{x} - \sqrt{3}\hat{y}\right) = \boldsymbol{a}_2 - \boldsymbol{a}_1$. Inserting these vectors into the summation in Eq. (4.7), we obtain

$$\mathcal{H}_{\boldsymbol{k}}^{AB} = N t \gamma_{\boldsymbol{k}}, \tag{4.8}$$

where we defined the nearest-neighbor hopping amplitude as

$$t \equiv \int \mathrm{d}\boldsymbol{r}\, \phi^{(A)*}(\boldsymbol{r}) \Delta V \phi^{(B)}(\boldsymbol{r} + \boldsymbol{\delta}_3),$$

and $\gamma_{\boldsymbol{k}}$ as

$$\gamma_{\boldsymbol{k}} = \left(1 + e^{-i\boldsymbol{k}\cdot\boldsymbol{a}_2} + e^{-i\boldsymbol{k}\cdot\boldsymbol{a}_3}\right). \tag{4.9}$$

Notice that the translation from lattice B to lattice A is $-\boldsymbol{\delta}_i$, for $i = 1, 2, 3$. Hence, if we substitute this into the other off-diagonal term $\mathcal{H}_{\boldsymbol{k}}^{BA}$, we just get extra minus signs in the exponents, implying that $\mathcal{H}_{\boldsymbol{k}}^{BA} = (\mathcal{H}_{\boldsymbol{k}}^{AB})^*$. For the diagonal terms $\mathcal{H}_{\boldsymbol{k}}^{AA} = \mathcal{H}_{\boldsymbol{k}}^{BB}$, we get

$$\mathcal{H}_{\boldsymbol{k}}^{AA} = N \int \mathrm{d}\boldsymbol{r} \sum_{\boldsymbol{R}_l} e^{i\boldsymbol{k}\cdot\boldsymbol{R}_l}\, \phi^{(A)*}(\boldsymbol{r}) \Delta V \phi^{(A)}(\boldsymbol{r} - \boldsymbol{R}_l)$$

Here, $\boldsymbol{R}_l$ runs over the six next-nearest neighbors, which are on the same sublattice. From Fig. 4.2a, we can see that they are given by the translations $\pm\boldsymbol{a}_i$ for $i = 1, 2, 3$. Hence, for the diagonal terms in the Hamiltonian matrix we obtain

$$\begin{aligned} \mathcal{H}_{\boldsymbol{k}}^{AA} &= 2Nt' \sum_{i=1}^{3} \cos(\boldsymbol{k}\cdot\boldsymbol{a}_i) \\ &= Nt' \left(|\gamma_{\boldsymbol{k}}|^2 - 3\right), \end{aligned} \tag{4.10}$$

where we defined the next-nearest-neighbor hopping amplitude as

$$t' \equiv \int \mathrm{d}\boldsymbol{r}\, \phi^{(A)*}(\boldsymbol{r}) \Delta V \phi^{(A)}(\boldsymbol{r} + \boldsymbol{a}_1).$$

Notice that the hopping amplitude is the same for each nearest neighbor due to symmetry. Similarly, we can determine the matrix elements of the overlap matrix. They are given by

$$\begin{aligned} \mathcal{S}_{\boldsymbol{k}}^{AB} &= (\mathcal{S}_{\boldsymbol{k}}^{BA})^* = s\gamma_{\boldsymbol{k}}^*, \\ \mathcal{S}_{\boldsymbol{k}}^{AA} &= \mathcal{S}_{\boldsymbol{k}}^{BB} = 1, \end{aligned}$$

where the overlap between orbitals on different sublattices is

$$s \equiv \int \mathrm{d}\boldsymbol{r}\, \phi^{(A)*}(\boldsymbol{r}) \phi^{(B)}(\boldsymbol{r} + \boldsymbol{\delta}_3).$$

The wave functions are assumed to be properly normalized, such that the overlap of wave functions on the same site is equal to one.

From Eq. (4.6), we see that solving the Schrödinger equation boils down to solving $\left(\mathcal{H}_{\boldsymbol{k}} - \epsilon_{\boldsymbol{k}}^{\lambda} \mathcal{S}_{\boldsymbol{k}}\right) \begin{pmatrix} a_{\boldsymbol{k}} \\ b_{\boldsymbol{k}} \end{pmatrix} = 0$, or equivalently,

$$\det\left(\mathcal{H}_{\boldsymbol{k}} - \epsilon_{\boldsymbol{k}}^{\lambda} \mathcal{S}_{\boldsymbol{k}}\right) = 0.$$

Inserting the expressions for the matrix elements of $\mathcal{H}_{\boldsymbol{k}}$ and $\mathcal{S}_{\boldsymbol{k}}$, this determinant becomes

$$\det \begin{bmatrix} t'\left(|\gamma_{\boldsymbol{k}}|^2 - 3\right) - \epsilon_{\boldsymbol{k}}^{\lambda} & (t - s\epsilon_{\boldsymbol{k}}^{\lambda})\gamma_{\boldsymbol{k}}^* \\ (t - s\epsilon_{\boldsymbol{k}}^{\lambda})\gamma_{\boldsymbol{k}} & t'\left(|\gamma_{\boldsymbol{k}}|^2 - 3\right) - \epsilon_{\boldsymbol{k}}^{\lambda} \end{bmatrix} = 0$$

From this equation, the dispersion can be computed straightforwardly by writing out the determinant and rearranging the terms, which eventually gives

$$\epsilon_{\boldsymbol{k}}^{\lambda} = \frac{t'\left(|\gamma_{\boldsymbol{k}}|^2 - 3\right) + \lambda t |\gamma_{\boldsymbol{k}}|}{1 + \lambda s |\gamma_{\boldsymbol{k}}|}, \qquad \lambda = \pm 1.$$

Under the reasonable assumptions that the overlap is small, i.e., $s \ll 1$, and that the nearest-neighbor interactions dominate over the next-nearest-neighbor interactions, i.e., $t' \ll t$, we may expand this dispersion around small s. This leads to

$$\epsilon_{\boldsymbol{k}}^{\lambda} = t'|\gamma_{\boldsymbol{k}}|^2 + \lambda t |\gamma_{\boldsymbol{k}}|. \tag{4.11}$$

A couple of remarks must be made. First of all, the expansion would actually yield an additional constant $-3t'$, which we omit because it is just an irrelevant energy shift. Furthermore, we have absorbed a term $-st$ into t', such that $t' - st \to t'$. We can view the redefined t' as some effective next-nearest-neighbor hopping term. Fitting this dispersion to numerical data yields values for the hopping parameters $t \simeq -3\,\mathrm{eV}$ and $t' \simeq 0.1t$ [24]. This confirms that t' is indeed considerably smaller than t. Notice that these values do not tell us the true next-nearest-neighbor hopping, but only the effective amplitude which includes a contribution from the nearest-neighbor overlap. In Fig. 4.3, the dispersion in Eq. (4.11) is plotted for $t' = 0.1t$. The solution for $\lambda = -1$ corresponds to the π-band (or valence band) and the solution for $\lambda = +1$ corresponds to the π^*-band

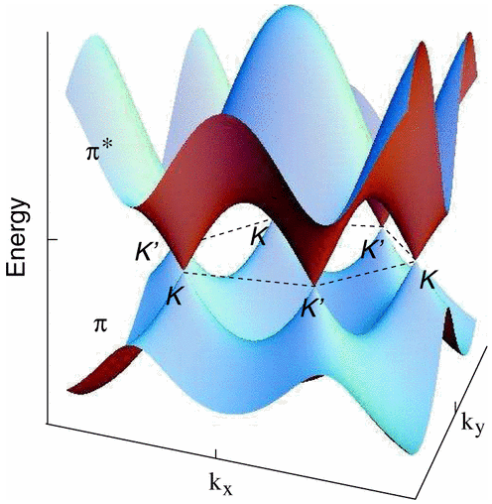

Figure 4.3: Dispersion in units of t as a function of $a\boldsymbol{k}$, using $t' = 0.1t$. Figure from Ref. [24]

(or conduction band) [24]. Both bands contain the same number of states, and each carbon atom contains one π-electron, which can have either spin up or down. Since the ground state of a fermionic system is formed by filling states from the bottom up, the valence band is completely filled, while the conduction band is completely empty (or, equivalently, completely filled with holes). The Fermi level is thus situated at the points where the bands touch each other. These six points are called Dirac points and they coincide with the corners of the first Brillouin zone, i.e., the K and K' points. From this plot, we can already see that the dispersion near these points is linear, which is characteristic for Dirac electrons, hence the name Dirac points. In order to check that these Dirac points indeed coincide with the K and K' points, we can set the dispersion to zero and solve for $\boldsymbol{k}$. This boils down to solving $|\gamma_{\boldsymbol{k}}| = 0$. Since $\gamma_{\boldsymbol{k}}$ is complex, both the imaginary and the real part of $\gamma_{\boldsymbol{k}}$ must be zero. This gives two equations for the two unknowns k_x and k_y. The solution is thus a set of points, and if you work out the equations you find that it is indeed the set of K and K' points that we derived earlier in Eq. (4.3).

Looking at Eq. (4.11), we can make a few remarks about the symmetries in the system. First of all, since $\epsilon^{\lambda}_{\boldsymbol{k}} = \epsilon^{\lambda}_{-\boldsymbol{k}}$, the system has time reversal symmetry[1]. This implies that the energy around the K-point is the same as around the K'-point. This twofold degeneracy at the Dirac points is also called the valley degeneracy. For low enough energies, this degeneracy survives in the vicinity of the two valleys, as can be seen from Fig. 4.3. Furthermore, there only is particle-hole symmetry, i.e., $\epsilon^{\lambda}_{\boldsymbol{k}} = -\epsilon^{-\lambda}_{\boldsymbol{k}}$, when t' vanishes. As we have seen before, t' is small in comparison to t. We can therefore neglect it altogether without significantly affecting the important features of the dispersion.

4.2.1 Effective Hamiltonian

It turns out to be instructive to define an effective Hamiltonian which ignores the fact that the wave functions are not orthogonal. The matrix elements of the effective Hamiltonian are then given by the elements of $\mathcal{H}_{\boldsymbol{k}}$, as defined in Eqs. (4.8) and (4.10), divided by N,

[1]Notice that time reversal $t \to -t$ implies $\boldsymbol{k} \to -\boldsymbol{k}$

such that

$$\mathcal{H}_{\boldsymbol{k}}^{eff} = \begin{pmatrix} t'|\gamma_{\boldsymbol{k}}|^2 & t\gamma_{\boldsymbol{k}}^* \\ t\gamma_{\boldsymbol{k}} & t'|\gamma_{\boldsymbol{k}}|^2 \end{pmatrix}. \tag{4.12}$$

This Hamiltonian yields the dispersion relation in Eq. (4.11), thus it basically uses the effective next-nearest-neighbor hopping amplitude, as we have discussed before. Notice that in this Hamiltonian we omitted the constant $-3t'$, just like we did for the dispersion in Eq. (4.11).

4.2.2 Tight-binding Hamiltonian in second quantization

In the previous section, we derived the tight-binding Hamiltonian for graphene in the language of first quantization. However, it is often more common to use the formalism of second quantization, which allows us to write the Hamiltonian in terms of creation and annihilation operators that act on states in Fock space. We introduce the operators $a_{\sigma,i}^\dagger$ and $a_{\sigma,i}$, which respectively create or annihilate a state on the A-sublattice, on site i, with spin σ. The operators $b_{\sigma,i}^\dagger$ and $b_{\sigma,i}$ are defined similarly for the B-sublattice. The hopping between nearest neighbors (which are on different sublattices) and next-nearest neighbors (which are on the same sublattice) can then be represented by the Hamiltonian [27]

$$H = t \sum_{\langle i,j\rangle,\sigma} (a_{\sigma,i}^\dagger b_{\sigma,j} + \text{h.c.}) + t' \sum_{\langle\langle i,j\rangle\rangle,\sigma} (a_{\sigma,i}^\dagger a_{\sigma,j} + b_{\sigma,i}^\dagger b_{\sigma,j} + \text{h.c.}), \tag{4.13}$$

where the first term runs over all nearest neighbors and the second sums runs over the next-nearest neighbors. In Appendix A.1, we show that this Hamiltonian is indeed equivalent to the effective Hamiltonian in first quantization that we derived in Eq. (4.12). The second quantized Hamiltonian will thus give rise to the same dispersion relation as the effective Hamiltonian, which is given by Eq. (4.11).

4.2.3 Low energy excitations

In Fig. 4.3, we can see that the low energy excitations occur near the Dirac points $\pm\boldsymbol{K}$. We may therefore expand the dispersion relation around these points in order to derive the low energy excitation energies. We consider wave vectors $\boldsymbol{k} = \pm\boldsymbol{K} + \boldsymbol{q}$, where $\boldsymbol{q}$ represents a small deviation from the Dirac points, such that $|\boldsymbol{q}| \ll |\boldsymbol{K}| \sim 1/a$. We consider the dispersion in Eq. (4.11), where we set $t' = 0$ for convenience. This will not alter the results much, since the next-nearest-neighbor interactions are much smaller than the dominant nearest-neighbor interactions, as we have seen before. Then, we obtain the dispersion $\epsilon_{\boldsymbol{k}}^\lambda = \lambda t|\gamma_{\boldsymbol{k}}|$. Expanding this around the Dirac points boils down to expanding $\gamma_{\boldsymbol{k}}$ around these points. First, we remark that $\gamma_{\boldsymbol{k}}$, as introduced in (4.9), is defined up to some arbitrary phase that does not affect the dispersion, since it only depends on the absolute value of $\gamma_{\boldsymbol{k}}$. We may make the substitution $\gamma_{\boldsymbol{k}} \to \gamma_{\boldsymbol{k}} e^{i\boldsymbol{k}\cdot\boldsymbol{\delta}_3} = e^{i\boldsymbol{k}\cdot\boldsymbol{\delta}_1} + e^{i\boldsymbol{k}\cdot\boldsymbol{\delta}_2} + e^{i\boldsymbol{k}\cdot\boldsymbol{\delta}_3}$.

Now we expand $\gamma_{\pm\boldsymbol{K}+\boldsymbol{q}}$ around $|\boldsymbol{q}| = 0$,

$$\begin{aligned}
\gamma_{\pm\boldsymbol{K}+\boldsymbol{q}} &= \sum_{i=1}^{3} e^{i(\pm\boldsymbol{K}+\boldsymbol{q})\cdot\boldsymbol{\delta}_i} \\
&\simeq \sum_{i=1}^{3} e^{\pm i\boldsymbol{K}\cdot\boldsymbol{\delta}_i} \left(1 + i\boldsymbol{q}\cdot\boldsymbol{\delta}_i - \frac{1}{2}(\boldsymbol{q}\cdot\boldsymbol{\delta}_i)^2 + \cdots\right) \\
&= \sum_{i=1}^{3} e^{\pm i\boldsymbol{K}\cdot\boldsymbol{\delta}_i} \left(i\boldsymbol{q}\cdot\boldsymbol{\delta}_i - \frac{1}{2}(\boldsymbol{q}\cdot\boldsymbol{\delta}_i)^2 + \cdots\right) \\
&\equiv \gamma_{\boldsymbol{q}}^{(1)} + \gamma_{\boldsymbol{q}}^{(2)} + \cdots ,
\end{aligned} \tag{4.14}$$

where in the third line we used the fact that the energy is zero at the Dirac points, hence $\gamma_{\pm\boldsymbol{K}} = 0$. By inserting the vectors $\boldsymbol{K}$ and $\boldsymbol{\delta}_i$, we can derive the expression for $\gamma_{\boldsymbol{q}}$. The Dirac points were given by $\pm\boldsymbol{K} = \pm 4\pi/3\sqrt{3}a\hat{x}$, and the $\boldsymbol{\delta}_i$ were defined in Eq. (4.2). We thus obtain $\boldsymbol{K}\cdot\boldsymbol{\delta}_1 = \frac{2\pi}{3}$, $\boldsymbol{K}\cdot\boldsymbol{\delta}_2 = -\frac{2\pi}{3}$ and $\boldsymbol{K}\cdot\boldsymbol{\delta}_3 = 0$. Substituting this into Eq. (4.14) yields

$$\begin{aligned}
\gamma_{\boldsymbol{q}}^{(1)} &= i\frac{a}{2}\left[(\sqrt{3}q_x + q_y)e^{\pm 2\pi i/3} + (-\sqrt{3}q_x + q_y)e^{\mp 2\pi i/3}\right] - iaq_y \\
&= \mp\frac{3a}{2}(q_x \pm iq_y).
\end{aligned}$$

Inserting this into the effective Hamiltonian (4.12) (with $t' = 0$), we obtain

$$\begin{aligned}
H_{\boldsymbol{q}} &= \mp\frac{3a}{2}t\begin{pmatrix} 0 & q_x \mp iq_y \\ q_x \pm iq_y & 0 \end{pmatrix} \\
&= \xi\hbar v_F \begin{pmatrix} 0 & q_x - i\xi q_y \\ q_x + i\xi q_y & 0 \end{pmatrix},
\end{aligned}$$

where we defined the Fermi velocity $v_F = -\frac{3a}{2\hbar}t$, which is positive, since t is negative. The parameter $\xi = \pm 1$ is the valley index, which corresponds to the inequivalent Dirac points $\pm\boldsymbol{K}$. The Hamiltonian acts on a spinor $\psi_{\boldsymbol{k},\xi}$ that represents the wave function in the corresponding valley ξ. We can write this Hamiltonian more compactly by using Pauli matrices, such that

$$H_{\boldsymbol{q}} = \xi\hbar v_F \left(q_x\sigma^x + \xi q_y\sigma^y\right).$$

This Hamiltonian already resembles a Dirac Hamiltonian and by flipping the indices of the $\xi = -1$ tensor, such that

$$\psi_{\boldsymbol{k},\xi=+1} = \begin{pmatrix} \psi^A_{\boldsymbol{k},+} \\ \psi^B_{\boldsymbol{k},+} \end{pmatrix}, \qquad \psi_{\boldsymbol{k},\xi=-1} = \begin{pmatrix} \psi^B_{\boldsymbol{k},-} \\ \psi^A_{\boldsymbol{k},-} \end{pmatrix}, \tag{4.15}$$

the Hamiltonian can be written as

$$H_{\boldsymbol{q}} = \xi\hbar v_F \left(q_x\sigma^x + q_y\sigma^y\right). \tag{4.16}$$

Hence, the Hamiltonian describing the low energy excitations in graphene is a two-dimensional massless Dirac Hamiltonian. It can be rewritten in four-spinor representation as

$$H_{\boldsymbol{q}} = \hbar v_F \tau^z \otimes \boldsymbol{q}\cdot\boldsymbol{\sigma},$$

where $\boldsymbol{\sigma} = (\sigma^x, \sigma^y)$ is a vector of Pauli matrices. The valley degeneracy is now captured in the Pauli matrix τ^z and this Hamiltonian acts on the four-spinor

$$\Psi = \begin{pmatrix} \psi^A_{\boldsymbol{q},+} \\ \psi^B_{\boldsymbol{q},+} \\ \psi^B_{\boldsymbol{q},-} \\ \psi^A_{\boldsymbol{q},-} \end{pmatrix}.$$

Besides the true spin of the electrons, we can distinguish to types of pseudospin: sublattice and valley pseudospin. The former is represented by the Pauli matrices that are indicated by σ^i in the above-mentioned Hamiltonian, where 'spin up' corresponds to one sublattice and 'spin down' to the other. The valley pseudospin is represented in the Hamiltonian by the Pauli matrix that is denoted by τ^z.

By inserting the expressions we found for $\gamma_{\boldsymbol{q}}$ up to first order in the dispersion (4.11), we find the linear excitation energies,

$$\epsilon^\lambda_{\boldsymbol{q}} = \lambda \hbar v_F |\boldsymbol{q}|.$$

This linear dispersion is characteristic for relativistic particle, that is why we refer to the electrons in graphene as relativistic, or Dirac, particles, even though they do not actually travel at the speed of light.

4.3 Landau levels in graphene

In Section 3.3, we have derived the Landau energy levels of non-relativistic two-dimensional electrons in a magnetic field by writing down the Lorentz force and inserting it in the Hamiltonian, which became a function of the mechanical momentum $\boldsymbol{\Pi} = \boldsymbol{p} + e\boldsymbol{A}$. The influence of the magnetic field was then captured in the vector potential $\boldsymbol{A}$, by the relation $\boldsymbol{B} = \nabla \times \boldsymbol{A}$. Since the components of $\boldsymbol{\Pi}$ turned out to be non-commuting we introduced ladder operators in the Hamiltonian, which reduced to the Hamiltonian of the well-known harmonic oscillator which frequency ω_c. The Landau levels for the normal electrons were thus $\epsilon_n = \hbar\omega_c(n + 1/2)$.

We now wish to extend the notion of Landau levels to the case of electrons in graphene. We repeat the above-mentioned procedure, starting with the Hamiltonian we derived in Eq. (4.16) and make the substitution for the momentum $\boldsymbol{q} \to \boldsymbol{\Pi}/\hbar = \boldsymbol{q}/\hbar + e\boldsymbol{A}/\hbar$. Like before, the commutator of Π_x and Π_y reads $[\Pi_x, \Pi_y] = -i\hbar^2 l_B^2$, and again we introduce the ladder operators

$$a \equiv \frac{l_B}{\sqrt{2}\hbar}(\Pi_x - i\Pi_y), \qquad a^\dagger \equiv \frac{l_B}{\sqrt{2}\hbar}(\Pi_x + i\Pi_y),$$

for which $[a, a^\dagger] = 1$. Substituting this in the Dirac Hamiltonian, we obtain the Hamiltonian for Dirac electrons in a magnetic field.

$$H^\xi_B = \frac{\sqrt{2}\xi\hbar v_F}{l_B} \begin{pmatrix} 0 & a \\ a^\dagger & 0 \end{pmatrix}.$$

Remember that this Hamiltonian acts on the the reversed tensors defined in Eq. (4.15). In order to obtain the energies associated to this Hamiltonian, we solve the eigenvalue

equation $H\psi_n = \epsilon_n \psi_n$, where we represent the general two-spinor ψ_n by

$$\psi_n = \begin{pmatrix} \alpha_n \\ \beta_n \end{pmatrix}.$$

The eigenvalue equation then yields two equations for the two components of ψ_n,

$$\begin{aligned} a\beta_n &= \frac{l_B \epsilon_n}{\sqrt{2}\xi\hbar v_F}\alpha_n \\ a^\dagger \alpha_n &= \frac{l_B \epsilon_n}{\sqrt{2}\xi\hbar v_F}\beta_n. \end{aligned} \tag{4.17}$$

If we act with $a^\dagger$ on the first equation and insert the second one, we obtain an equation for β_n,

$$a^\dagger a\, \beta_n = \left(\frac{l_B \epsilon_n}{\sqrt{2}\hbar v_F}\right)^2 \beta_n. \tag{4.18}$$

Notice that $\xi^2 = 1$, which makes the equation independent of ξ. From this equation, we can see that β_n is an eigenstate of the number operator $a^\dagger a$, thus it must be proportional to the state $|n\rangle$, for which $a^\dagger a|n\rangle = n|n\rangle$. Hence, the numerical factor on the right-hand side of Eq. (4.18) must be equal to n. This provides us with an expression for the energies ϵ_n. Since there can be a positive and a negative solution to this equation, we label these solutions by $\lambda = \pm 1$,

$$\epsilon_{\lambda n} = \frac{\lambda\sqrt{2}\hbar v_F}{l_B}\sqrt{n} = \lambda v_F \sqrt{2e\hbar B n}. \tag{4.19}$$

The energy scales with the square root of the magnetic field, in contrast with the ordinary Landau levels, which are linear in B. Furthermore, the level spacing is not constant as it was for the usual case, since here we have $\epsilon_n - \epsilon_{n-1} \sim \sqrt{n} - \sqrt{n-1}$ (see Fig. 4.4). Since these energy levels describe the energy of massless Dirac electrons in a magnetic field, we call them relativistic Landau levels. Unlike the usual non-relativistic Landau levels, there is actually a zero energy level in this case. Notice furthremore that there is a degeneracy in the system, since the energy does not depend on the valley index ξ, thus it is the same for both valleys.

The eigenstates of this Hamiltonian may be derived using the fact that β_n is an eigenstate of the number operator, as mentioned before. Hence, $\beta_n \sim |n\rangle$. Firstly, for $n \neq 0$, we can insert the expression for the energy in the eigenvalue equations (4.17) and derive that $\lambda\xi\sqrt{n}\alpha_n = a\beta_n = \sqrt{n}|n-1\rangle$. Hence, $\alpha_n \sim \lambda\xi|n-1\rangle$. Thus we can write the normalized eigenstate for $n \neq 0$ as

$$\psi_n = \frac{1}{\sqrt{2}}\begin{pmatrix} |n-1\rangle \\ \lambda\xi|n\rangle \end{pmatrix}$$

For the case that $n = 0$, we obtain $\alpha_0 \sim a\beta_0 \sim a|0\rangle = 0$. Hence, the normalized eigenstate is

$$\psi_{n=0} = \frac{1}{\sqrt{2}}\begin{pmatrix} 0 \\ |n=0\rangle \end{pmatrix}.$$

Remember that the second component of this spinor represents the K-valley on the B-sublattice or the K'-valley on the A-sublattice. Since the first component is zero (not to be confused with the vacuum state $|0\rangle$), the valley-pseudospin and the sublattice index coincide, since there is no mixing between the valleys and the sublattices. Therefore, the two sublattices are decoupled in the zero-energy level.

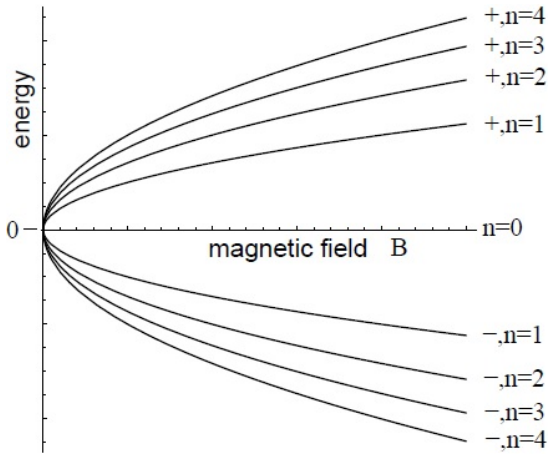

Figure 4.4: Landau levels in graphene as a function of magnetic field. Figure from Ref. [11].

4.4 Quantum Hall effect in graphene

As discussed in detail in Chapter 3, the presence of a perpendicular magnetic field in a 2DEG does not only result in the formation of Landau levels, but as a consequence also gives rise to the quantum Hall effect. When an electric current is sent through the sample, a voltage can be measured transverse to the current (the Hall voltage). The corresponding conductivity and resistivity that follow from it are then quantized. This feature can be depicted by the characteristic plateaus in the Hall resistivity, accompanied by a vanishing longitudinal resistivity, as was for example shown in Fig. 3.2. Transitions to the next plateaus occur at integer filling factors and the Hall resistance is quantized as

$$R_H = \frac{h}{e^2}\frac{1}{\nu}. \tag{4.20}$$

The quantum Hall effect can be observed when the thermal fluctuations that would otherwise destroy the Landau level structure is much smaller than the energy gap between the levels. In a usual 2DEG, the Landau level separation is $\Delta E_n = \hbar\omega_c = \hbar eB/m = 0.12\,B[\mathrm{T}]\,\mathrm{meV}$. The energy of the thermal fluctuations is of order $E_T = k_B T = 0.086\,T[\mathrm{K}]\,\mathrm{meV}$. The highest magnetic field strengths that can be realized experimentally are typically of order $B = 30\,\mathrm{T}$. For that value, the temperature should be much smaller than $40\,K$ to be able to observe the quantum Hall effect. Temperatures are then usually in the order of a couple of Kelvin at most. This makes the observation of the QHE in conventional 2DEGs rather difficult.

In graphene, we might also expect to see the quantum Hall effect, since the electrons in graphene are also quantized in Landau levels in the presence of a perpendicular magnetic field, as was explained in the previous section. However, since the Landau levels in graphene differ from the ones in a usual 2DEG, the energy gaps between the Landau levels are also different. In this case,

$$\Delta E_n = \frac{\sqrt{2}\hbar v_F}{l_B}\left(\sqrt{n} - \sqrt{n-1}\right).$$

Notice that the gaps to the next Landau levels now depend on the Landau level index, in contrast to the non-relativistic case. It is again instructive to calculate the typical

energy scale of the gaps. For the lowest few Landau levels, $\left(\sqrt{n}-\sqrt{n-1}\right) \sim 0.1-1$, hence $\Delta E_n \sim v_F\sqrt{2e\hbar}\sqrt{B}$. The energy gap scales with the square root of the magnetic field strength, as we have seen before. The Fermi velocity was defined in Section 4.2.3 as $v_F = -\frac{3a}{2\hbar}t \approx 6 \cdot 10^6\,\mathrm{ms}^{-1}$. This leads to an inter-Landau level separation energy of order $E_n \sim 0.2\sqrt{B[\mathrm{T}]}\,\mathrm{eV}$. For $B = 30\,\mathrm{T}$ this leads to $E_n \sim 1\,\mathrm{eV}$, which is much larger than the typical energy gaps in conventional 2DEGs. The temperature that corresponds to a thermal energy of 1 eV is $T = 10^4\,\mathrm{K}$. A temperature much smaller than this is easy to realize. Indeed, in 2007 the quantum Hall effect was observed in graphene at room temperature [28].

There is another essential difference for the IQHE in graphene. In conventional 2DEGs, the plateaus in the Hall resistivity occur at integer filling factors $\nu = n$, corresponding to the particular Landau level n. In graphene, however, the Hall resistivity is quantized around the filling factors $\nu = 2(2n+1)$. To understand this, remember that each filled Landau level acts as a conducting channel, contributing one quantum of conductance. The question is now how many electrons you need to fill the system up to a certain Landau level n. To illustrate this, consider first the usual case of non-relativistic electrons. If we ignore spin, then a completely filled Landau level corresponds to a filling of $\nu = 1$, or more generally, $\nu = n$. If we now consider spinfull electrons and a vanishing Zeeman effect, then a state can be occupied by an 'up' and a 'down' electron. Hence, if the lowest Landau level is completely filled, then we have $\nu = 2$ and in general, $\nu = 2n$. In the case of graphene, we not only have spin degeneracy, but also a valley degeneracy. Naively, we could assume that the filling would then become $\nu = 4n$. However, this would imply that the conductivity is vanishing for $n = 0$, which violates the fact that there is a Landau level at $n = 0$ which has extended states that contribute to the conductivity. If we look again at Fig. 4.4, we see that for each valley, there are $2n+1$ extended states. The 1 comes from the zero-energy Landau level and the $2n$ refers to the $\pm n$ states. Hence, in total the filling in graphene is $\nu = 2(2n+1)$ and the resistance (4.20) is quantized at $\nu = 2, 6, 10, 14, ...$

4.4.1 Fractional quantum Hall effect in graphene

Besides the IQHE, we also expect to see the FQHE, which arises at fractional filling factors, due to the interaction between the electrons, as elaborated on in section 3.5. Indeed, in 2009, the FQHE was observed for the first time in graphene, for $\bar{\nu} = \pm 1/3$ in the lowest Landau level [29,30]. In more recent experiments, the FQHE was observed for a range of other filling factors, mainly in the lowest Landau levels [31–33].

For graphene, we can use the same kind of Laughlin wave function as we introduced for GaAs in section 3.5.1. They merely need to be generalized to fit the multi-component character of the wave functions. This was already done by Halperin for electrons with spin in GaAs, by just taking a product of two individual wave functions for the different spin species [34]. This is be valid if we ignore interactions between electrons with different spins. This procedure can be straightforwardly generalized to the four spin-valley components in graphene. The generalized Laughlin wave function is [35]

$$\psi_{m_1,\cdots,m_4;n_{ij}} = \phi^L_{m_1,\cdots,m_4}\phi^{inter}_{n_{ij}},$$

where

$$\phi^{L}_{m_1,\cdots,m_4} = \prod_{j=1}^{4} \prod_{k_j<l_j}^{N_j} \left(z^{(j)}_{k_j} - z^{(j)}_{l_j} \right)^{m_j} e^{-\sum_{j=1}^{4} \sum_{k_j=1}^{N_j} |z^{(j)}_{k_j}|^2/4}$$

is the product of the one-component wave functions and

$$\phi^{inter}_{n_{ij}} = \prod_{i<j}^{4} \prod_{k_i}^{N_i} \prod_{k_j}^{N_j} \left(z^{(i)}_{k_i} - z^{(j)}_{k_j} \right)^{n_{ij}}$$

described the inter-component correlations.

Chapter 5

Electron phases in two-dimensional quantum Hall systems

As mentioned before, the physics of partially filled Landau levels is extremely rich. Besides the FQHE, that occurs for certain fractional values of the filling factor $\nu = p/(2ps \pm 1)$, with p and s integers, the electrons can also form a normal electron liquid and all kinds of electron-solid phases, like a Wigner crystal or electron-bubble phases. Furthermore, it was shown experimentally that, at certain filling-factor intervals, the resistivity shoots back up to the integer value corresponding to a completely filled Landau level [36, 37]. This feature is called the reentrant integer quantum Hall effect (RIQHE) and it has been theoretically explained by the formation of electron-solid phases in partially filled higher Landau levels ($n > 0$) [38]. In this section, we will study the competition between the energies of different electron phases in order to determine which phase has the lowest energy for various values of the filling factor in a partially filled Landau level. We will follow the derivations done in Ref. [38]. In Chapter 6, we will analyze how these calculations change in the case of graphene.

5.1 The model

We consider spinless electrons and restrict their dynamics to the n-th Landau level. In the absence of inter-Landau-level excitations, all the $n-1$ lowest Landau levels are completely filled and the Landau levels higher than n are empty. Hence, we can express the partial filling of the n-th Landau level as $\bar{\nu} = \nu - [\nu] = \bar{N}_{el}/N_B$, where $\bar{N}_{el}$ is the number of electrons in the last Landau level and $N_B = A/2\pi l_B^2$ is the degeneracy in each Landau level, as derived in Section 3.3.1. Since all electrons in the n-th Landau level have the same kinetic energy $\hbar\omega_c(n+1/2)$, this will just be an irrelevant constant in the Hamiltonian when calculating energy minima and we can omit it. The Hamiltonian then consist only of Coulomb interactions between the electrons,

$$H = \frac{1}{2}\int d^2r d^2r' \psi_n^\dagger(\boldsymbol{r})\psi_n(\boldsymbol{r})v(\boldsymbol{r}-\boldsymbol{r}')\psi_n^\dagger(\boldsymbol{r}')\psi_n(\boldsymbol{r}'). \tag{5.1}$$

The fermion field operators of the electrons in the n-th Landau level at a position $\boldsymbol{r}$ in space are given by

$$\psi_n(\boldsymbol{r}) = \sum_{y_0}\langle \boldsymbol{r}|n, y_0\rangle c_{n,y_0}, \tag{5.2}$$

where c_{n,y_0} ($c^\dagger_{n,y_0}$) destroys (creates) an electron in the state $|n, y_0\rangle$. As we have derived in Section 3.3.3, the wave functions in the Landau gauge can be written in terms of Hermite polynomials $H_n(x)$,

$$\langle \boldsymbol{r}|n, y_0\rangle = \left(L\sqrt{\pi}2^n n! l_B\right)^{-1/2} H_n\left(\frac{y-y_0}{l_B}\right) e^{iy_0 x/l_B^2} e^{-(y-y_0)^2/2l_B^2}.$$

In order to write the Hamiltonian in reciprocal space, we first make a Fourier transform of the density operator $\rho_n(\boldsymbol{r}) = \psi_n^\dagger(\boldsymbol{r})\psi_n(\boldsymbol{r})$,

$$\rho_n(\boldsymbol{q}) = \int d^2 r \psi_n^\dagger(\boldsymbol{r})\psi_n(\boldsymbol{r}) e^{i\boldsymbol{q}\cdot\boldsymbol{r}}.$$

Substituting the expressions for $\psi_n^\dagger(\boldsymbol{r})$ and $\psi_n(\boldsymbol{r})$ from Eq. (5.2), we can derive (see Appendix B.1) that the density operator in reciprocal space takes the form

$$\begin{aligned}\rho_n(\boldsymbol{q}) &= \langle n|e^{i\boldsymbol{q}\cdot\hat{\boldsymbol{\eta}}}|n\rangle \sum_{y_0, y_0'} \langle y_0|e^{i\boldsymbol{q}\cdot\hat{\boldsymbol{R}}}|y_0'\rangle c^\dagger_{n,y_0} c_{n,y_0'} \\ &= F_n(q)\bar{\rho}(\boldsymbol{q}),\end{aligned} \tag{5.3}$$

where the cyclotron variable $\hat{\boldsymbol{\eta}}$ and the guiding center operator $\hat{\boldsymbol{R}}$ where defined in Section 3.3. The density operator is now split into two parts: the form factor $F_n(q) = \langle n|e^{i\boldsymbol{q}\cdot\hat{\boldsymbol{\eta}}}|n\rangle$, which captures all the Landau-level dependence, and the projected density operator $\bar{\rho}(\boldsymbol{q}) = \sum_{y_0,y_0'} \langle y_0|e^{i\boldsymbol{q}\cdot\hat{\boldsymbol{R}}}|y_0'\rangle c^\dagger_{n,y_0} c_{n,y_0'}$, which projects $\rho_n(\boldsymbol{q})$ to the lowest Landau level, such that $\bar{\rho}(\boldsymbol{q})$ does not depend on n. The explicit form of the projected density operator depends on the particular choice of the gauge. In the Landau gauge, it is given by [38]

$$\bar{\rho}(\boldsymbol{q}) = \sum_{y_0} e^{-iq_y y_0} c^\dagger_{n,y_0+q_x l_B^2/2} c_{n,y_0-q_x l_B^2/2}. \tag{5.4}$$

Since the cyclotron variable $\hat{\boldsymbol{\eta}}$ is gauge invariant (see Section 3.3 for more details), the form factor is independent of the gauge as well. It is given explicitly in terms of the Laguerre polynomials $L_n(x)$ by (see Appendix B.1)

$$F_n(q) = L_n(q^2 l_B^2/2) e^{-q^2 l_B^2/4}. \tag{5.5}$$

The Hamiltonian in reciprocal space can now be written in terms of these projected density operators. Furthermore, we absorb the form factor into the potential, such that we get for the Hamiltonian

$$H = \frac{1}{2A}\sum_{\boldsymbol{q}} v_n(q)\bar{\rho}(-\boldsymbol{q})\bar{\rho}(\boldsymbol{q}). \tag{5.6}$$

where $\sum_{\boldsymbol{q}} = A\int d^2q/(2\pi)^2$ and $v_n(q)$ is the effective Coulomb potential given by

$$v_n(q) = v(q)[F_n(q)]^2, \qquad v(q) = 2\pi e^2/\epsilon q. \tag{5.7}$$

Hence, we have basically shifted the Landau-level dependence from the density operators to the potential. Therefore, the Hamiltonian depends on this effective potential that

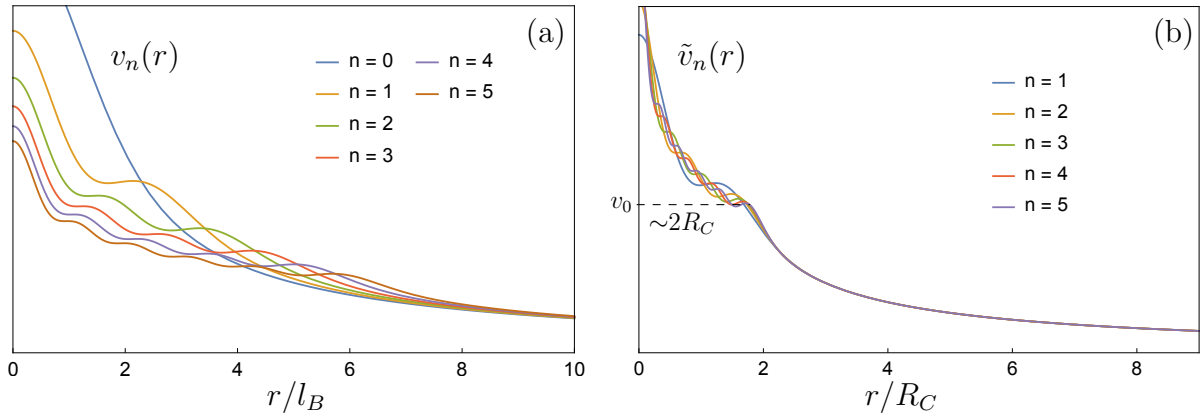

Figure 5.1: (a) Effective potential in real space, in units of $e^2/\epsilon l_B$; (b) Scaled potential, in units of $e^2/\epsilon l_B$. A universal length scale of $\sim 2R_C$ arises. Fig. replotted from Ref. [38].

captures the structure of the Landau level of interest and on the lowest-Landau-level projected density operators.

Using the anti-commutation relations for fermions, $\{c_{n,y_0}, c^\dagger_{n',y_0'}\} = \delta_{n,n'}\delta_{y_0,y_0'}$ and $\{c_{n,y_0}, c_{n',y_0'}\} = \{c^\dagger_{n,y_0}, c^\dagger_{n',y_0'}\} = 0$, we can derive the commutator between $\bar{\rho}(\boldsymbol{q})$ and $\bar{\rho}(\boldsymbol{k})$ (see Appendix B.2),

$$[\bar{\rho}(\boldsymbol{q}), \bar{\rho}(\boldsymbol{k})] = 2i \sin\left(\frac{(\boldsymbol{q}\times\boldsymbol{k})_z l_B^2}{2}\right) \bar{\rho}(\boldsymbol{q}+\boldsymbol{k}). \tag{5.8}$$

The Hamiltonian (5.6) with the interaction potential (5.7), together with the commutation relations (5.8) define the quantum mechanical model we are interested in.

In order to understand the effect of the form factor that reveals the Landau level structure, we plot the effective potential in real space for different values of n, as shown in Fig. 5.1. At first sight, no general conclusions can be drawn from this plot. Let us now define the rescaled potential $\tilde{v}_n(r/R_C) = v_n(r)(R_C/l_B) = v_n(r)\sqrt{2n+1}$, where R_C is the cyclotron radius. This potential has in fact universal features, independent of the particular Landau level, as can be seen from Fig. 5.1. For all Landau levels $n > 0$, the potential is no longer scale free, since a "shoulder" arises at a characteristic length scale of $\sim 2R_C$. This can lead to the formation of a Wigner crystal or a bubble phase, depending on the interparticle distance d. If $d \gg 2R_C$, then the particles interact via the potential tail, which is just the Coulomb interaction. In that regime, the electrons will arrange themselves in a triangular lattice in order to minimize the Coulomb energy. This state is called a Wigner crystal. If $d \sim 2R_C$ it becomes energetically favorable for electrons to form clusters, since this decrease the energy. This "short-range attraction" can be intuitively understood from a toy model. Consider electrons in one dimension distributed in a homogeneous way, let us say, separated by $d = 2R_C$, as shown in Fig. 5.2. The interaction among four electrons costs $3v_0$ (see Fig. 5.1b). On the other hand, if the electrons form two clusters of two electrons separated by $1R_C$, than the total energy is approximately $2v_0$, because the energy cost between the two clusters, which are separated by $4R_C$, is negligible. In general, the overall energy will be lower in this so-called bubble phase and the clusters of electrons interact via the Coulomb tail of the interaction potential, forming a Wigner crystal with M electrons per site.

Notice that in the lowest Landau level there is no length scale in the potential, since

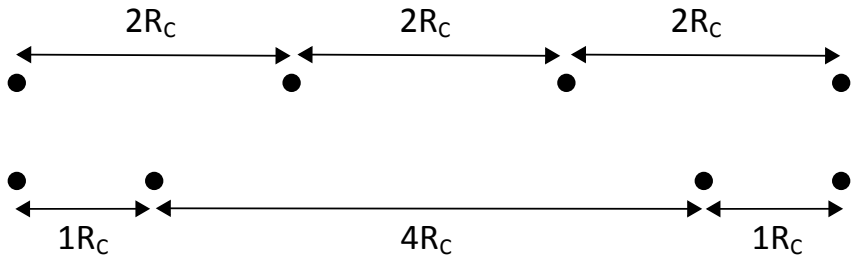

Figure 5.2: Formation of a bubble phase. In the upper line, four electrons are separated from each other by $2R_C$. If the inner two electrons move towards the outer two electrons, as in the lower line, they can reduce their total energy by forming bubbles.

the Laguerre polynomial for $n = 0$ is just a constant. Hence, in the lowest Landau level there can be a Wigner crystal, but no bubble phases.

5.2 Electron-solid phases

To describe the electron-solid phases, we resort to mean-field theory and use the Hartree-Fock approximation for the Hamiltonian. We follow the calculations done in Ref. [38]. In the Hartree-Fock approximation, we replace the two-body interaction term by an effective one-body term [39]. That is, in the Hamiltonian we replace the operator product $c^\dagger_{y_0+\gamma_q} c_{y_0-\gamma_q} c^\dagger_{y_0'+\gamma_q} c_{y_0'-\gamma_q} \to \langle c^\dagger_{y_0+\gamma_q} c_{y_0-\gamma_q}\rangle c^\dagger_{y_0'+\gamma_q} c_{y_0'-\gamma_q} - \langle c^\dagger_{y_0+\gamma_q} c_{y_0'-\gamma_q}\rangle c^\dagger_{y_0'+\gamma_q} c_{y_0-\gamma_q}$. The first term is referred to as the Hartree term and the second one as the Fock, or exchange, term. Substituting this mean-field approximation into the Hamiltonian, we get two contributions: the Hartree part of the Hamiltonian,

$$\begin{aligned} H_H &= \frac{1}{2A}\sum_{\boldsymbol{q}} v_n(q) \sum_{y_0,y_0'} e^{iq_y(y_0-y_0')} \langle c^\dagger_{y_0-\gamma_q} c_{y_0+\gamma_q}\rangle c^\dagger_{y_0'+\gamma_q} c_{y_0'-\gamma_q} \\ &= \frac{1}{2A}\sum_{\boldsymbol{q}} v_n(q) \langle \bar\rho(-\boldsymbol{q})\rangle \bar\rho(\boldsymbol{q}), \end{aligned}$$

where we used the definition of $\bar\rho(-\boldsymbol{q})$ in the second line, and the Fock term

$$H_F = \frac{1}{2A}\sum_{\boldsymbol{q}} v_n(q) \sum_{y_0,y_0'} e^{iq_y(y_0-y_0')} \langle c^\dagger_{y_0-\gamma_q} c_{y_0'-\gamma_q}\rangle c^\dagger_{y_0'+\gamma_q} c_{y_0+\gamma_q}.$$

We wish to express this in terms of $\langle\bar\rho(-\boldsymbol{q})\rangle\rho(\boldsymbol{q})$ as well. To bring the Fock Hamiltonian in this form, we make a few substitutions. Firstly, we remark that for the expectation value we want something of the form $\langle c^\dagger_{a-b} c_{a+b}\rangle$, hence we make the substitution $y_0 \to a - b$, $y_0' \to a + b$. This leads to

$$H_F = \frac{1}{2A}\sum_{\boldsymbol{q}} v_n(q) \sum_{a,b} e^{-2iq_y b} \langle c^\dagger_{a-b-\gamma_q} c_{a+b-\gamma_q}\rangle c^\dagger_{a+b+\gamma_q} c_{a-b+\gamma_q}.$$

Then, we substitute $a - \gamma_q \to x_0$, $a + \gamma_q \to x_0'$ and $b \to \gamma_p = p_x l_B^2/2$, to obtain

$$H_F = \frac{1}{2A}\sum_{\boldsymbol{q}} v_n(q) \sum_{x_0,p_x} e^{-iq_y p_x l_B^2} \langle c^\dagger_{x_0-\gamma_p} c_{x_0+\gamma_p}\rangle c^\dagger_{x_0'+\gamma_p} c_{x_0'-\gamma_p}.$$

Finally, to find the desired form of the exponents, we multiply by 1, using the identity

$$1 = \frac{1}{N_B} \sum_{p_y, x_0'} e^{ip_y(x_0 - x_0' + 2\gamma_q)},$$

where $N_B = n_B A$ is the number of states per Landau level. This finally leads to,

$$\begin{aligned} H_F &= \frac{1}{2AN_B} \sum_{\boldsymbol{q}} v_n(q) \sum_{p_x, p_y} e^{-i(q_y p_x - p_y q_x) l_B^2} \sum_{x_0, x_0'} e^{ip_y(x_0 - x_0')} \langle c^\dagger_{x_0 - \gamma_p} c_{x_0 + \gamma_p} \rangle c^\dagger_{x_0' + \gamma_p} c_{x_0' - \gamma_p} \\ &= \frac{1}{2AN_B} \sum_{\boldsymbol{q}} v_n(q) \sum_{p_x, p_y} e^{-i(q_y p_x - p_y q_x) l_B^2} \langle \bar{\rho}(-\boldsymbol{p}) \rangle \bar{\rho}(\boldsymbol{p}) \\ &= \frac{1}{2A} \sum_{\boldsymbol{p}} u^F(\boldsymbol{p}) \langle \bar{\rho}(-\boldsymbol{p}) \rangle \bar{\rho}(\boldsymbol{p}), \end{aligned}$$

where we have absorbed all the extra terms coming from the substitutions in the Fock potential $u^F(\boldsymbol{p})$. The total Hamiltonian $H_{HF} = H_H - H_F$ is then linear in the projected density operators,

$$H_{HF} = \frac{1}{2A} \sum_{\boldsymbol{q}} u_n^{HF}(\boldsymbol{q}) \langle \bar{\rho}(-\boldsymbol{q}) \rangle \bar{\rho}(\boldsymbol{q}), \tag{5.9}$$

where

$$\begin{aligned} u_n^{HF}(\boldsymbol{q}) &= v_n(q) - u_n^F(\boldsymbol{q}) \\ &= v_n(q) - \frac{1}{N_B} \sum_{\boldsymbol{p}} v_n(p) e^{-i(p_y q_x - q_y p_x) l_B^2}. \end{aligned} \tag{5.10}$$

For the lowest few Landau levels, we can calculate the exchange potential $u_n^F(\boldsymbol{q})$ explicitly, e.g., for $n = 1$ we have,

$$u_{n=1}^F(q) = \sqrt{\frac{\pi}{2}} \frac{e^2}{\epsilon l_B} \frac{e^{-q^2 l_B^2/4}}{8 n_B} \left[(6 - 2q^2 l_B^2 + q^4 l_B^4) I_0 \left(\frac{q^2 l_B^2}{4} \right) - q^4 l_B^4 I_1 \left(\frac{q^2 l_B^2}{4} \right) \right], \tag{5.11}$$

where I_j are the modified Bessel functions (see Appendix B.3).

From the Hartree-Fock Hamiltonian, we can now derive the cohesive energy of the electron-solid phases $E_{coh} = \langle H_{HF} \rangle / \bar{N}_{el}$, which is the energy per electron needed to form a certain phase. We express it in terms of the order parameter $\Delta(\boldsymbol{q}) \equiv \langle \bar{\rho}(\boldsymbol{q}) \rangle / n_B A$, which is proportional to the average (projected) electron density, such that it can detect whether the electrons are uniformly distributed or arranged in a certain structure, making it indeed behave as an order parameter. The cohesive energy of a charge density wave in the n-th Landau level thus reads

$$\begin{aligned} E_{coh}^{CDW}(n, \bar{\nu}) &= \frac{1}{2A\bar{N}_{el}} \sum_{\boldsymbol{q}} u_n^{HF}(\boldsymbol{q}) \langle \bar{\rho}(-\boldsymbol{q}) \rangle \langle \bar{\rho}(\boldsymbol{q}) \rangle \\ &= \frac{n_B}{2\bar{\nu}} \sum_{\boldsymbol{q}} u_n^{HF}(\boldsymbol{q}) |\Delta(\boldsymbol{q})|^2. \end{aligned} \tag{5.12}$$

For the bubble phase, clusters of M electrons are arranged in a two-dimensional triangular lattice, represented by lattice vectors $\boldsymbol{R}_j$. Notice that the normal Wigner

crystal is essentially a bubble phase with $M = 1$. The distribution of the electrons is described by a local guiding-center filling factor $\bar{\nu}(\boldsymbol{r}) = \sum_j \Theta(r_B - |\boldsymbol{r} - \boldsymbol{R}_j|)$, where $r_B = l_B\sqrt{2M}$ is the radius of a bubble with M electrons and Θ is the step function. The partial filling factor is the fraction of the unit cell that is occupied by a bubble, hence

$$\bar{\nu} = \frac{\text{area bubble}}{\text{area unit cell}} = \frac{\pi r_B^2}{\sqrt{3}\Lambda_B^2/2}, \tag{5.13}$$

where Λ_B is the lattice spacing of the triangular lattice. Since the local filling factor describes the local electron density per flux quantum, the order parameter can be written in terms of its Fourier transform. Hence,

$$\begin{aligned}
\Delta_M(\boldsymbol{q}) &= \frac{1}{A}\int d^2r\, \bar{\nu}(\boldsymbol{r}) e^{i\boldsymbol{q}\cdot\boldsymbol{r}} \\
&= \frac{1}{A}\sum_j \int d^2r\, \Theta(r_B - |\boldsymbol{r} - \boldsymbol{R}_j|) e^{i\boldsymbol{q}\cdot(\boldsymbol{r}-\boldsymbol{R}_j)} e^{i\boldsymbol{q}\cdot\boldsymbol{R}_j} \\
&= \frac{1}{A}\int_0^{r_B} dr\, r \int_0^{2\pi} d\phi_r\, e^{iqr(\sin\phi_q \sin\phi_r + \cos\phi_q\cos\phi_r)} \sum_j e^{i\boldsymbol{q}\cdot\boldsymbol{R}_j},
\end{aligned}$$

where we used the definition of $\bar{\nu}(\boldsymbol{r})$ and wrote the results in polar coordinates, i.e. $\boldsymbol{q} = (q\cos\phi_q, q\sin\phi_q)$ and $\boldsymbol{r} = (r\cos\phi_r, r\sin\phi_r)$. These integrals can be evaluated as

$$\begin{aligned}
\Delta_M(\boldsymbol{q}) &= \frac{2\pi}{A}\int_0^{r_B} dr\, r J_0(qr) \sum_j e^{i\boldsymbol{q}\cdot\boldsymbol{R}_j} \\
&= \frac{2\pi l_B\sqrt{2M}}{Aq} J_1(ql_B\sqrt{2M}) \sum_j e^{i\boldsymbol{q}\cdot\boldsymbol{R}_j},
\end{aligned}$$

where $J_n(x)$ are Bessel functions of the first kind. By replacing this result for the order parameter in the expression for the cohesive energy that we derived in Eq. (5.12), we obtain for the energy of the bubble phase,

$$\begin{aligned}
E_{coh}^B(n; M, \bar{\nu}) &= \frac{n_B}{2\bar{\nu}} \frac{A}{(2\pi)^2} \int d^2q\, u_n^{HF}(\boldsymbol{q}) \frac{8\pi^2 l_B^2 M}{A^2 q^2} J_1(l_B q\sqrt{2M})^2 \sum_{j,j'} e^{i\boldsymbol{q}\cdot(\boldsymbol{R}_j - \boldsymbol{R}_{j'})} \\
&= \frac{n_B l_B^2 M}{\bar{\nu} A_{pc}} \int d^2q\, u_n^{HF}(\boldsymbol{q}) \frac{J_1(l_B q\sqrt{2M})^2}{q^2} \sum_j e^{i\boldsymbol{q}\cdot\boldsymbol{R}_j},
\end{aligned}$$

where we used the fact that $\boldsymbol{R}_j - \boldsymbol{R}_{j'}$ is again a lattice vector, such that we can write $\sum_{j,j'} e^{i\boldsymbol{q}\cdot(\boldsymbol{R}_j - \boldsymbol{R}_{j'})} = N\sum_j e^{i\boldsymbol{q}\cdot\boldsymbol{R}_j}$, with N the number of lattice sites. In the triangular lattice, there is one lattice site in the unit cell, hence the total number of sites can be determined by $N = A/A_{pc}$, where A_{pc} is the area of the unit cell, which in this case reads $A_{pc} = \sqrt{3}\Lambda_B^2/2$. Furthermore, we can use the identity $\sum_j e^{-i\boldsymbol{q}\cdot\boldsymbol{R}_j} = (2\pi)^2/A_{pc}\sum_l \delta(\boldsymbol{q} - \boldsymbol{G}_l)$, where $\boldsymbol{G}_l$ are the reciprocal lattice vectors (see Appendix B.4). Using also Eq. (5.13), we can now write the cohesive energy of an M-electron-bubble phase in the n-th Landau level as a function of $\bar{\nu}$,

$$\begin{aligned}
E_{coh}^B(n; M, \bar{\nu}) &= \frac{n_B\bar{\nu}}{M} \sum_l u_n^{HF}(\boldsymbol{G}_l) \frac{J_1(\sqrt{2M} l_B|\boldsymbol{G}_l|)^2}{l_B^2|\boldsymbol{G}_l|^2} \\
&= \frac{\bar{\nu}}{2\pi l_B^2 M} \sum_l u_n^{HF}(\boldsymbol{G}_l) \frac{J_1(\sqrt{2M} l_B|\boldsymbol{G}_l|)^2}{l_B^2|\boldsymbol{G}_l|^2},
\end{aligned} \tag{5.14}$$

where we used that $n_B = 1/2\pi l_B^2$ in the second step. Notice that if we plot the energy in terms of $e^2/\epsilon l_B$, all the other l_B dependence will drop out. In Appendix B.5, we elaborate on this and other details concerning this function and its graphical representation.

As a last remark, we mention the possibility for the electrons to form other kinds of crystal phases, such as the so-called striped phase, where the electrons are arranged periodically in long bands. In this thesis, we will not go further into the details of these phases.

5.2.1 The effect of impurities

The model that we have derived thus far to describe the electron-solid phase does not take into account the fact that there are always some impurities in the sample, while they can actually play an important role in the physics of the system. As we have seen for the IQHE for example, impurities can localize electrons, which causes the formation of plateaus in the resistivity. In the FQHE, the effect of impurities is less important, because the Laughlin liquid is incompressible en therefore less susceptible to external perturbations. However, in the electron-solid phases, the impurities can pin the crystal such that the collective sliding mode is suppressed [38]. The crystal can deform slightly (while still remaining near their lattice sites) such as to find a configuration that minimizes the energy due to the impurities. This can then lower the total cohesive energy of the crystal compared to the energies that we have just derived.

To model the impurities, we consider a short-range Gaussian impurity potential with correlation length ξ and potential strength V_0 in the weak-pinning limit. In this limit, the energy gained by following the impurity potential is small compared to the elastic energy it costs to deform the crystal. The energy density that describes this competition is given by [40, 41]

$$\epsilon(L_0) = \frac{\mu\xi^2}{L_0^2} - V_0\frac{\sqrt{n_{el}}}{L_0},$$

where μ is the elasticity of an M-electron bubble and is given by $\mu \approx 0.25M^2e^2n_M^{3/2}/\epsilon$, with $n_M = \bar{\nu}/2\pi M l_B^2$ the bubble density [38]. Furthermore, L_0 is the Larkin length, which is the typical length scale on which a straight line is collectively pinned by impurities. Minimizing this energy with respect to L_0 yields

$$L_0^* = \frac{1}{4\pi}\frac{\sqrt{M}\bar{\nu}e^2\xi^2}{\epsilon l_B^2 V_0}.$$

The reduction of the cohesive energy due to the impurities is thus

$$\delta E_{coh}^B(M,\bar{\nu}) = \frac{\epsilon(L_0^*)}{n_{el}} = -\frac{(2\pi)^{3/2}l_B^2}{\sqrt{M}\bar{\nu}^{3/2}}\frac{V_0^2/\xi^2}{e^2/\epsilon l_B}.$$

The parameters V_0, ξ and ϵ are properties of the material and are not known in advance. However, we can treat the dimensionless ratio

$$E_{pin} \equiv \frac{V_0/\xi}{e^2/\epsilon l_B^2},$$

as one parameter that we can tune via l_B. The energy difference is then given in terms of this dimensionless pinning parameter as

$$\delta E^B_{coh}(M,\bar{\nu}) = -\frac{e^2}{\epsilon l_B}\frac{(2\pi)^{3/2}}{\sqrt{M}\bar{\nu}^{3/2}}E^2_{pin}.$$

In Section 5.4, we will plot the energies of the bubble phases taking into account this pinning energy to see how it changes the competition between the solid- and liquid phases.

5.3 Electron-liquid phases

For filling factors $\bar{\nu}_L = 1/M$, with M odd-integer, the FQHE occurs and the system is in an incompressible quantum-liquid state. For these values of the filling factor, the system can be described by Laughlin's wave functions, which we derived in Section 3.5.1,

$$\psi_M = \prod_{i<j}^{N}(z_i - z_j)^M e^{-\sum_k |z_k|^2/4},$$

where $z_j = x_j - iy_j$.

The cohesive energy of the liquid state can be derived using the plasma analogy. This analogy boils down to identifying $|\psi_M|^2$ with the Boltzmann factor of a classical 2D one-component plasma $e^{-\beta U_{cl}}$, where ψ_M is the Laughlin wave function for $\nu = 1/M$. To derive the energy, we follow the steps used in Ref. [42]. We start off by writing the energy corresponding to the Laughlin wave function in the statistical physics analogy,

$$U_M = \frac{\nu}{2}\int_0^\infty dr\, r\,[g(r) - 1]\,V(r),$$

where $V(r)$ is the Coulomb interaction potential and $g(r)$ is the radial distribution function given by

$$g(z_1, z_2) = \frac{N(N-1)}{Z\rho^2}\int d^2z_3 \cdots d^2z_N |\psi_M(\{z\})|^2,$$

where ρ is the density, $Z = \langle\psi_M|\psi_M\rangle$ and $dz_j = dx_j dy_j$. In order to evaluate this function, we write the z_1 and z_2 dependence of the wave function explicitly and absorb the rest of the coordinates in some general function. Furthermore, we rewrite $z_+ = z_1 + z_2$ and $z = z_1 - z_2$. We then obtain a polynomial in z_+ and z, where z turns out to appear only with odd powers,

$$\begin{aligned}\psi_M &= \prod_{i<j}^{N}(z_i - z_j)^M e^{-\sum_k |z_k|^2/4} \\ &= \sum_{n,m=0}^{\infty} a_{n,2m+1}(z_3, \cdots, z_N) z_+^n z^{2m+1} e^{-(|z_+|^2+|z|^2)/8}.\end{aligned}$$

In the radial distribution function we use $|\psi_M|^2$, thus we write this again explicitly in terms of z and z_+,

$$|\psi_M|^2 = \sum_{n,n',m,m'=0}^{\infty} a_{n,2m+1}(z_3, \cdots, z_N) b_{n',2m'+1}(z_3^*, \cdots, z_N^*) z_+^n (z_+^*)^{n'} z^{2m+1} (z^*)^{2m'+1} e^{-(|z_+|^2+|z|^2)/4}.$$

We replace this in $g(z_1, z_2)$ and, without evaluating the integral explicitly, we absorb all the terms that do not depend on z in some general function $A_{m,m'}$ that thus depends on z_+, since all the other coordinates are integrated out,

$$g(z) = \sum_{m,m'=0}^{\infty} A_{m,m'}(z_+) z^{2m+1} (z^*)^{2m'+1} e^{-|z|^2/4}.$$

This is the most general form of the radial distribution function using this particular wave function. Remember that the original wave function depends on $M = 1/(2s+1)$, the filling fraction at which is was defined. To emphasize this dependence, we write $A_{m,m'} = A^s_{m,m'}$. Now, we make two assumptions to be able to simplify this expression. First of all, we assume that the center-of-mass coordinate z_+ is uniformly distributed, which is reasonable in a liquid. This implies that $A_{m,m'}$ does not depend on z_+. Furthermore, we assume that there is no orientational order, such that $g(z)$ only depends on $|z|$, implying that $A^s_{m,m'} = 0$ if $m \neq m'$. Hence, we can write

$$A^s_{m,m'} = b^s_m \delta_{m,m'},$$

such that the radial distribution function reduces to

$$g(z) = \sum_{m=0}^{\infty} b^s_m |z|^{2(2m+1)} e^{-|z|^2/4}.$$

Since $\rho g(|z|)$ represents the average particle density at a distance $|z|$ from a given particle, we have that $\lim_{|z|\to\infty} g(|z|) = 1$, because at large distances the correlation between particles vanishes and the average density is then just the bulk density. In order to satisfy this constraint, we write b^s_m as

$$b^s_m = \frac{2}{4^{2m+1}(2m+1)!} \left(1 + c^s_{2m+1}\right),$$

with $\lim_{m\to\infty} c^s_{2m+1} = 0$. Substituting this in $g(z)$ we obtain

$$\begin{aligned} g(z) &= 2 \sum_{m=0}^{\infty} \frac{(|z|^2/4)^{2m+1}}{(2m+1)!} \left(1 + c^s_{2m+1}\right) e^{-|z|^2/4} \\ &= 1 - e^{-|z|^2/2} + 2 \sum_{m=0}^{\infty} c^s_{2m+1} \frac{(|z|^2/4)^{2m+1}}{(2m+1)!} e^{-|z|^2/4}. \end{aligned}$$

We can impose further constraints on the coefficients c_{2m+1} by using the charge-neutrality, perfect screening and compressibility sum rules, which yield [42]

$$\begin{aligned} &\sum_m c^s_{2m+1} = -s/2, \\ &\sum_m (2m+2) c^s_{2m+1} = -s/4, \\ &\sum_m (2m+3)(2m+2) c^s_{2m+1} = s^2/2. \end{aligned}$$

As a final constraint, we can look at the short-range behavior of $g(r)$, which goes like $g(r) \sim r^{2(2s+1)}$. From this, we can deduce that $c^s_{2m+1} = -1$ for $m < s$. With these constraints, we can calculate the values for c^s_{2m+1} for $m = \{s, s+1, s+2\}$, assuming $c^s_{2m+1} = 0$

	c_1^s	c_3^s	c_5^s	c_7^s	c_8^s	c_{11}^s	c_{13}^s
$s=1$	-1	17/32	1/16	-3/32	0	0	0
$s=2$	-1	-1	7/16	11/8	-13/16	0	0
$s=3$	-1	-1	-1	-25/32	79/16	-85/32	0
$s=4$	-1	-1	-1	-1	-29/8	47/4	-49/8

Table 5.1: Coefficients c_{2m+1}^s, where s represents the fractional filling $\bar{\nu} = 1/(2s+1)$.

for $m > s+2$, since c_{2m+1}^s should vanish for large m. For $s = 1, 2, 3, 4$ (corresponding to filling factors $\nu = 1/3, 1/5, 1/7, 1/9$) the coefficients are given in Table 5.1.

The energy of the Laughlin liquid in the lowest Landau level is defined with respect to the uncorrelated liquid and can be written in reciprocal space as [38]

$$U = \frac{1}{2A} \sum_{\boldsymbol{q}} v_0(q)[\bar{s}(q) - 1], \tag{5.15}$$

where $\bar{s}(q) = \langle \bar{\rho}(-\boldsymbol{q})\bar{\rho}(\boldsymbol{q})\rangle / \bar{N}_{el}$ is the projected structure factor, which relates to the static structure factor $s(q)$ by $\bar{s}(q) = s(q) - (1 - e^{-q^2/2})$ [43]. Since the structure factor is the Fourier transform of $g(r)$, we can derive the projected structure factor to be [38]

$$\bar{s}(q) = (1-\bar{\nu}) + 4\bar{\nu} \sum_{m=0}^{\infty} c_{2m+1}^s L_{2m+1}(q^2) e^{-q^2/2},$$

where $L_{2m+1}(x)$ are Laguerre polynomials. The energy of the Laughlin liquid in the n-th Landau level can be obtained by replacing $v_0(q)$ by the effective potential $v_n(q)$. It can be written in the form

$$U = -\frac{\bar{\nu}}{2A} \sum_{\boldsymbol{q}} v_n(q) + E_{coh}^L(n, s), \tag{5.16}$$

with the cohesive energy given by

$$E_{coh}^L(n, s) = \frac{\bar{\nu}}{\pi} \sum_{m=0}^{\infty} c_{2m+1}^s V_{2m+1}^n, \tag{5.17}$$

where V_{2m+1}^n are Haldane's pseudo potentials,

$$V_{2m+1}^n = \frac{2\pi}{A} \sum_{\boldsymbol{q}} v_n(q) L_{2m+1}(q^2) e^{-q^2/2}.$$

5.3.1 Quasiparticle- and quasihole excitations

The energy derived in Eq. (5.17) is valid at the filling factors $\bar{\nu}_L = 1/(2s+1)$. For filling factors that are slightly different from $\bar{\nu}_L$, we need to take into account the quasiparticle and quasihole excitation energies. For filling factors in the vicinity of $\bar{\nu}_L$, the situation can be mapped into completely filled Landau levels of composite fermions and hence the quasiparticles and -holes can be treated as non-interacting. The cohesive energy for the

quantum-liquid phase is then given by the Laughlin energy plus a small contribution from the energy of the quasiparticles ($\Delta^n_+(s)$) or quasiholes ($\Delta^n_-(s)$),

$$E^{q-l}_{coh}(n,s,\bar{\nu}_\pm) = E^L_{coh}(n,s) + [\pm\bar{\nu}(2s+1)-1]\Delta^n_\pm(s),$$

where $\bar{\nu}_+$ ($\bar{\nu}_-$) indicate a filling that is slightly higher (lower) than the Laughlin filling factor $\bar{\nu} = 1/(2s+1)$. The quasiparticle and -hole excitation energies may be computed analytically using Murthy and Shankar's Hamiltonian theory [44, 45]. They treat the problem in terms of composite fermions (CFs), which were introduced in Section 3.5.2. For an electron filling of $\bar{\nu} = 1/(2s+1)$, the problem maps to a completely filled Λ-level with an effective magnetic length $l^*_B = \sqrt{\hbar/eB^*} = l_B/\sqrt{1-c^2}$, where we used Eq. (3.31) to derive $c^2 = 2ps/(2p+1)$. The density operator of the CFs can then be described by the so-called preferred combination [45]

$$\bar{\rho}^p(\boldsymbol{q}) = \bar{\rho}(\boldsymbol{q}) - c^2\bar{\chi}(\boldsymbol{q}).$$

It is given explicitly in terms of CF creation- and annihilation operators as

$$\bar{\rho}^p(\boldsymbol{q}) = \sum_{j,j';m,m'} \langle m|e^{-i\boldsymbol{q}\cdot\boldsymbol{R}}|m'\rangle\langle j|\bar{\rho}^p(\boldsymbol{q})|j'\rangle c^\dagger_{j,m}c_{j',m'}.$$

The matrix elements of this operator are given by

$$\begin{aligned}
\langle m|e^{-i\boldsymbol{q}\cdot\boldsymbol{R}}|m'\rangle &= \sqrt{\frac{m'!}{m!}}\left(\frac{-iq^*l^*_B}{\sqrt{2}}\right)^{m-m'} L^{m-m'}_{m'}\left(\frac{q^2l^{*2}_B}{2}\right)e^{-q^2l^{*2}_B/4},\\
\langle j|\bar{\rho}^p(\boldsymbol{q})|j'\rangle &= \sqrt{\frac{j'!}{j!}}\left(\frac{-iql^*_Bc}{\sqrt{2}}\right)^{j-j'} e^{-q^2l^{*2}_Bc^2/4}\\
&\quad\times\left[L^{j-j'}_{j'}\left(\frac{q^2l^{*2}_Bc^2}{2}\right) - c^{2(1-j+j')}e^{-q^2/2c^2}L^{j-j'}_{j'}\left(\frac{q^2l^{*2}_B}{2c^2}\right)\right],
\end{aligned}$$

where we use the complex notation $q = q_x - iq_y$ and $L^{j-j'}_{j'}$ are the generalized Laguerre polynomials.

The quasiparticle and -hole excitation energies are then given respectively by [38]

$$\begin{aligned}
\Delta^n_{qp}(s,p) &= \frac{1}{2}\int_{\boldsymbol{q}} v_n(q)\langle p|\bar{\rho}^p(-\boldsymbol{q})\bar{\rho}^p(\boldsymbol{q})|p\rangle - \int_{\boldsymbol{q}} v_n(q)\sum_{j'=0}^{p-1}|\langle p|\bar{\rho}^p(\boldsymbol{q})|j'\rangle|^2,\\
\Delta^n_{qh}(s,p) &= -\frac{1}{2}\int_{\boldsymbol{q}} v_n(q)\langle p-1|\bar{\rho}^p(-\boldsymbol{q})\bar{\rho}^p(\boldsymbol{q})|p-1\rangle + \int_{\boldsymbol{q}} v_n(q)\sum_{j'=0}^{p-1}|\langle p-1|\bar{\rho}^p(\boldsymbol{q})|j'\rangle|^2,
\end{aligned}$$

where $\int_{\boldsymbol{q}} = \int d^2q/(2\pi)^2$ and $|p\rangle$ denotes a state with p completely filled Λ-levels.

5.4 Competition between phases

We have derived the energies of different possible electron phases. The competition between these energies will determine which phase will be the ground state. In Fig. 5.3a, we replotted from Ref. [38] the different energies in order to investigate the behavior of the system in the $n = 1$ Landau level. The energies for the quantum liquid, the Wigner

crystal phase (1-electron-bubble phase) and the 2-electron-bubble phase are shown. The energy for the striped phase, which we did not discuss here, is also indicated. Notice that we only plot the regime where $0 \leq \bar{\nu} < 0.5$, due to particle-hole symmetry. Fig. 5.3b shows measurements of the Hall resistance done by Eisenstein et al. [46], as a function of magnetic field strengths that correspond to a fractional filling of the $n = 1$ Landau level. At integer filling (when $\bar{\nu}$=0), the resistance is quantized as $R_{xy} = h/e^2\nu$, where $\nu = 3$ (notice that due to spin degeneracy, a completely filled lowest Landau level corresponds to a filling $\nu = 2$, hence a filling of $\nu = 3$ corresponds to the $n = 1$ Landau level). If we start increasing the filling, then the electrons in the slightly filled Landau level, will be individually pinned by impurities, which give rise to the integer quantum Hall plateau. As the filling increases further, the electrons will form a Wigner crystal, which remains collectively pinned by impurities. In the transport response, there is simply a plateau in the Hall resistivity, although at some point the physics changed from single-particle to collective (Wigner crystal) localization. At even higher filling, we can see from Fig. 5.3a that the quantum liquid has the lowest energy and the FQHE can be observed at $\bar{\nu} = 1/5$ in Fig. 5.3b. If we now increase the filling further, the Wigner crystal phase becomes again energetically favorable and the electrons solidify into a denser electron crystal. Since the lattice itself is pinned by impurities it cannot slide, such that there is no conductance of electrons in this partially filled Landau level. Hence, the only states that contribute to the conductance are the edge states of all the n filled Landau levels underneath. This will then give rise to the same value of the resistance as for the $\bar{\nu} = 0$ situation. Therefore, the resistance shoots back up to the integer value. As the filling is increased, the solid- and liquid phases are alternating, giving rise to the FQHE and the RIQHE.

In the lowest Landau level we expect no bubble phases to occur, but a Wigner crystal might be possible. From the blue solid line in Fig. 5.4a, we see that the Laughlin liquid always has the lowest energy, therefore there are no solid phases in the lowest Landau level. Disorder may nevertheless alter this picture because they may lower the energy of the Wigner crystal, especially at very low doping, whereas they let the energy of the Laughlin liquid unaltered. Indeed, in Section 5.2.1, we have shown that they may lower the cohesive energy of the crystals by an amount characterized by the dimensionless pinning energy parameter $E_{pin} = (V_0/\xi)/(e^2/\epsilon l_B^2)$. In Fig. 5.4a, the dashed lines show the effect of impurities for $E_{pin} = 2.5 \cdot 10^{-5}$ and $E_{pin} = 10^{-4}$. From this graph, we can conclude that the qualitative behavior of the phase diagram remains roughly the same, the only difference is that some of the occurrences of the FQHE may be washed out by the impurities. For example, in both the $n = 0$ and $n = 1$ Landau level, the Laughlin liquid is the ground state for $\bar{\nu} = 1/7$ if we ignore the impurities, while the Wigner crystal is the lowest in energy if the impurity potential is very strong (blue dashed line in Fig. 5.4b). Furthermore, the width of the plateaus in the Hall resistivity may be changed under the influence of impurities, since the melting- and freezing points are shifted.

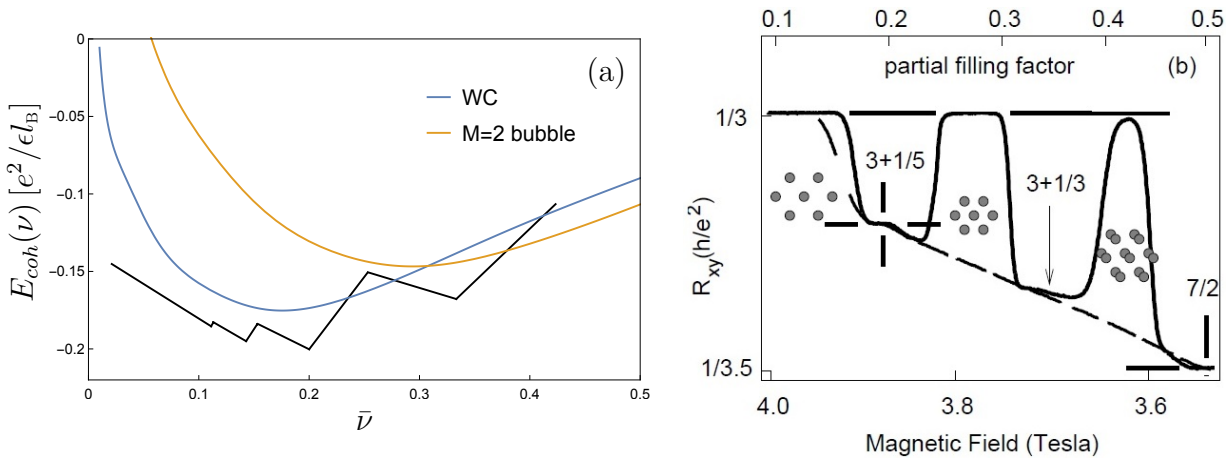

Figure 5.3: (a) Cohesive energies for $M = 1$ and $M = 2$ bubble phases and for the quantum liquid. (b) Experimental data for the Hall resistance as a function of the filling. It shoots back up to the integer value at the regions where the solid phase is energetically favorable. Figures from Ref. [38]

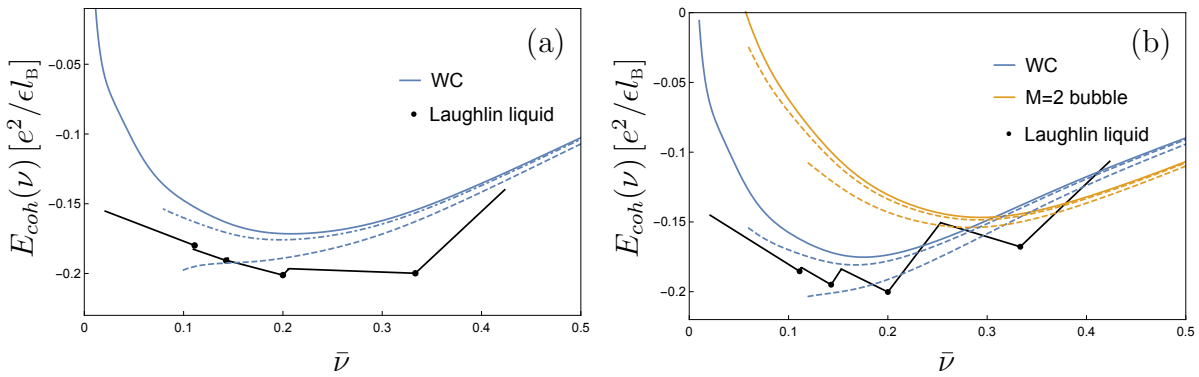

Figure 5.4: Cohesive energies of the liquid phase (black), the Wigner crystal (solid blue) and 2-electron bubble (solid orange). Dashed (dashed-dotted) lines represent the phases with a strong (weak) impurity potential taken into account, in the $n = 0$ (a) and $n = 1$ (b) Landau level.

Chapter 6

Electron phases in graphene

In order to generalize the theory of electron-solid and liquid phases in Chapter 5 to graphene, we must investigate which properties of the electrons change with respect to those in GaAs. As we have seen in Chapter 4, there are two major characteristics that distinguish graphene from other two-dimensional electron systems. First of all, the dispersion is different. Electrons in graphene have a linear (or relativistic) dispersion, in contrast to the parabolic dispersion of electrons in a normal 2DEG. The change in dispersion is reflected in the Landau-level structure as well. In graphene, the energy levels of electrons in a magnetic field scale with $\sqrt{Bn}$, as opposed to Bn for non-relativistic electrons. However, this is not relevant for the purpose of this chapter, because we will only consider interactions between the electrons when a Landau level is partially filled. In that case, the kinetic energy is the same for all electrons and becomes just an irrelevant constant. Hence, it does not matter what the Landau levels look like, since all electrons are in the same Landau level. The story becomes more complicated when we include Landau-level mixing. In our analysis we will ignore it, but we will comment on the effect it can have when we investigate the different phases in graphene.

The second difference between graphene a usual 2DEG is the fact that graphene has a multi-component wave function, as elaborated on in Section 4.2. When ignoring the spin degeneracy, graphene still has an extra degree of freedom due to the sublattice symmetry that it possesses. In reciprocal space, this symmetry manifests itself as the existence of two valleys. These are the two inequivalent points in the Brillouin zone where the Dirac cones are located. The wave function of the electrons correspondingly has two components. In the following sections, we will show that this leads to a change in the form factor and subsequently also in the effective electron-electron interaction. We will investigate how this will alter the results for the charge-density waves and the Laughlin-liquid, which we obtained in Chapter 5.

6.1 Change of the form factor

We want to set up a model for the interaction between the electrons in graphene similar to the one in Chapter 5. In this section, we follow the calculations done in Ref. [47].

We start by writing out the density operator, using the two-component wave functions in the Landau gauge. As derived in Section 4.3, the real space wave function of electrons in graphene under a perpendicular magnetic field reads

$$\psi_\sigma(\boldsymbol{r}) = e^{i\sigma \boldsymbol{K}\cdot\boldsymbol{r}}\chi_\sigma(\boldsymbol{r}), \tag{6.1}$$

where $\sigma = \pm 1$ denotes the valley at the point $\pm\boldsymbol{K}$ and the two components of $\chi_\sigma(\boldsymbol{r})$ represent the two sublattices,

$$\chi_+(\boldsymbol{r}) = \frac{1}{\sqrt{2}} \sum_{n,m} \begin{pmatrix} i\sqrt{1+\delta_{n,0}}\,\langle \boldsymbol{r}||n|,m\rangle \\ \mathrm{sgn}(n)\langle \boldsymbol{r}||n|-1,m\rangle \end{pmatrix}, \quad \chi_-(\boldsymbol{r}) = \frac{1}{\sqrt{2}} \sum_{n,m} \begin{pmatrix} \mathrm{sgn}(n)\langle \boldsymbol{r}||n|-1,m\rangle \\ i\sqrt{1+\delta_{n,0}}\,\langle \boldsymbol{r}||n|,m\rangle \end{pmatrix}. \tag{6.2}$$

Here, $\mathrm{sgn}(n) = 0$ for $n = 0$ and $\langle \boldsymbol{r}||n|,m\rangle$ are the usual (non-relativistic) one-particle wave functions [47]. As mentioned before, we ignore Landau level mixing and therefore the density operator projected onto a Landau level n on a sublattice α is

$$\rho^n_\alpha(\boldsymbol{r}) = \sum_{\sigma,\sigma'} \psi^\dagger_{\alpha,\sigma}(\boldsymbol{r})\psi_{\alpha,\sigma'}(\boldsymbol{r}).$$

In reciprocal space, the total density operator is then the Fourier transform of the density in real space, summed over the two sublattices. It can be expressed in terms of a projected density operator and a form factor.

$$\rho^n(\boldsymbol{q}) = \rho^n_1(\boldsymbol{q}) + \rho^n_2(\boldsymbol{q}) = \sum_{\sigma,\sigma'} F^{\sigma,\sigma'}_n(\boldsymbol{q})\bar{\rho}^{\sigma,\sigma'}(\boldsymbol{q}),$$

where the projected density operators are given by

$$\bar{\rho}^{\sigma,\sigma'}(\boldsymbol{q}) = \sum_{m,m'} \langle m|e^{-i[\boldsymbol{q}+(\sigma-\sigma')\boldsymbol{K}]\cdot\boldsymbol{R}}|m'\rangle c^\dagger_{n,m,\sigma} c_{n,m',\sigma'}.$$

Notice that for $\sigma = \sigma'$ they reduce to the normal non-relativistic projected density operators. The form factors are given by

$$\begin{aligned} F^{\sigma,\sigma}_n &= \frac{1}{2}\left[L_{|n|}\left(\frac{q^2 l_B^2}{2}\right) + L_{|n|-1}\left(\frac{q^2 l_B^2}{2}\right)\right] e^{q^2 l_B^2/4}, \\ F^{\sigma,-\sigma}_n &= \frac{\lambda i l_B[q + q^* - \sigma(K+K^*)]}{2\sqrt{2|n|}} L^1_{|n|-1}\left(\frac{l_B^2|\boldsymbol{q}-\sigma\boldsymbol{K}|^2}{2}\right) e^{-l_B^2|\boldsymbol{q}-\sigma\boldsymbol{K}|^2/4}, \end{aligned}$$

where we used the complex notation $q = q_x - iq_y$ and $K = K_x - iK_y$. A detailed derivation of these results is presented in Appendix C.1. The interaction Hamiltonian given in Eq. (5.1) then becomes, in reciprocal space,

$$H = \frac{1}{2} \sum_{\sigma_1,\cdots,\sigma_4} \sum_{\boldsymbol{q}} v^{\sigma_1,\cdots,\sigma_4}_n(\boldsymbol{q}) \bar{\rho}^{\sigma_1\sigma_3}(-\boldsymbol{q})\bar{\rho}^{\sigma_2\sigma_4}(\boldsymbol{q}),$$

where the effective interaction is given by

$$v^{\sigma_1,\cdots,\sigma_4}_n(\boldsymbol{q}) = v(q) F^{\sigma_1\sigma_3}_n(-\boldsymbol{q}) F^{\sigma_2\sigma_4}_n(\boldsymbol{q}), \tag{6.3}$$

with $v(q) = 2\pi e^2/\epsilon q$ the usual Coulomb potential in two dimensions. It can be shown (see Appendix C.1) that terms of the form $F^{\sigma,\sigma}_n(\mp\boldsymbol{q})F^{\sigma',-\sigma'}_n(\pm\boldsymbol{q})$ or $F^{\sigma,-\sigma}_n(-\boldsymbol{q})F^{\sigma,-\sigma}_n(\boldsymbol{q})$ are exponentially small in a/l_B. Furthermore, backscattering terms of the form $F^{\sigma,-\sigma}_n(-\boldsymbol{q})F^{-\sigma,\sigma}_n(\boldsymbol{q})$ are algebraically small in a/l_B. Thus, up to leading order in perturbation theory, we may write the interaction Hamiltonian as

$$H = \frac{1}{2} \sum_{\sigma,\sigma'} \sum_{\boldsymbol{q}} v^g_n(q)\bar{\rho}_\sigma(-\boldsymbol{q})\bar{\rho}_{\sigma'}(\boldsymbol{q}), \tag{6.4}$$

where $\bar{\rho}_\sigma(\boldsymbol{q}) \equiv \bar{\rho}^{\sigma\sigma}(\boldsymbol{q})$ and $v_n^g(q)$ is the effective interaction in graphene, given by

$$v_n^g(q) = v(q)[F_n^g(q)]^2, \tag{6.5}$$

with $F_n^g(q)$ the graphene form factor

$$F_n^g(q) = \begin{cases} \frac{1}{2}\left[L_{|n|}\left(\frac{q^2 l_B^2}{2}\right) + L_{|n|-1}\left(\frac{q^2 l_B^2}{2}\right)\right] e^{q^2 l_B^2/4} & n \neq 0, \\ e^{q^2 l_B^2/4} & n = 0. \end{cases} \tag{6.6}$$

Notice that if graphene is valley polarized (i.e., if we only consider one particular valley), the effective Hamiltonian in Eq. (6.4) reduces to the one for the usual 2DEGs defined in Eq. (5.6), apart from the different form factor. Furthermore, for $n = 0$ the form factor of graphene coincides with the one from the conventional 2DEGs. Hence, the special characteristics of graphene do not change the structure of the lowest Landau level.

6.2 Effective interaction in graphene

From the effective interaction, we can already gain some information about the possible electronic phases of the system. In Chapter 5, we have shown that for normal 2DEGs there is some universal behavior in the effective interaction in real space. When we scale the potential by l_B/R_C and the coordinates by R_C, the curves for the potential become quasi-universal and a characteristic length scale emerges. The presence of this length scale gives rise to the formation of electron bubbles. The question arises whether such universal behavior also occurs in graphene and whether we can reveal a length scale in the system. To this end, we plot the effective potential (6.5) in real space, together with the scaled potential $\tilde{v}_n(r/R_C) = v_n(r)\sqrt{2n+1}$, as shown in Fig. 6.1. Indeed, here we also see this universal length scale emerging in the scaled potential. However, this does not seem to hold for the $n = 1$ Landau level, which remains scale free. This can be understood because the form factor in graphene in the n-th Landau level is a combination of the normal form factors in the n-th and $(n-1)$-th Landau level. Since the effective potential for normal electrons in the lowest Landau level is scale free, we might expect that this characteristic also shows up in the $n = 1$ Landau level in graphene, which indeed seems to be the case. Hence, there are can only be a Wigner crystal or a liquid phase in the $n = 1$ Landau level, since the existence of bubbles is intrinsically linked to the effective attractive interaction at length scales $R_C < r < 2R_C$, which manifest as a shoulder (a plateau) in the effective rescaled potential for $n > 1$.

Another remark that can be made about Fig. 6.1 is that the scaled potential still looks as if the various graphs are not all scaled to the same length scale. Notice that we have scaled both the potential and the distance by $\sqrt{2n+1}$. However, since the potential in graphene mixes the n-th and $(n-1)$-th Landau level, we may assume that the scaling should also incorporate this mixing. If we scale the distance by the average cyclotron radius, that is,

$$\bar{R}_C = \frac{l_B}{2}\left(\sqrt{2n+1} + \sqrt{2(n-1)+1}\right), \tag{6.7}$$

and the potential by $l_B/\bar{R}_C$, then we obtain the results shown in Fig. 6.2. We can conclude that scaling by this average cyclotron radius yields a better universal result and that there is a length scale of approximately $2\bar{R}_C$ emerging in the system.

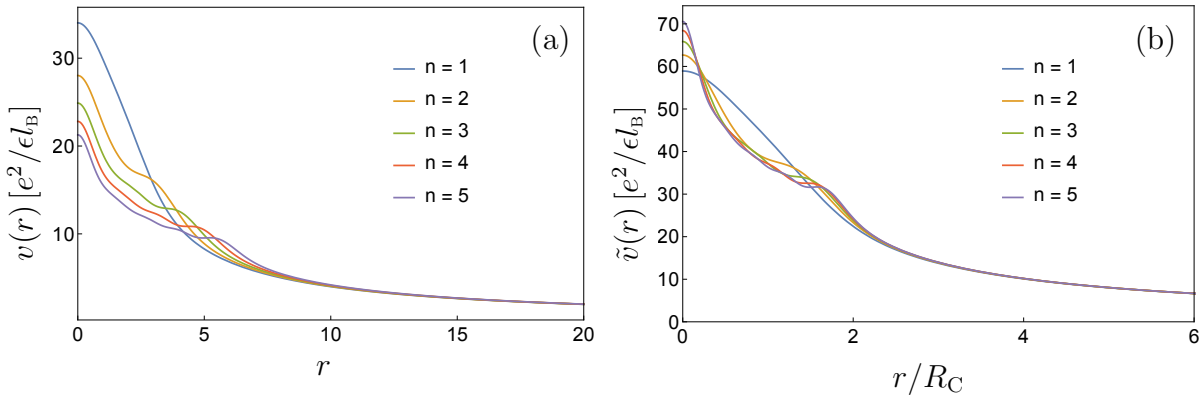

Figure 6.1: (a) Effective real space potential in various Landau levels. (b) The rescaled potential. A universal length scale emerges, except in the $n = 1$ Landau level.

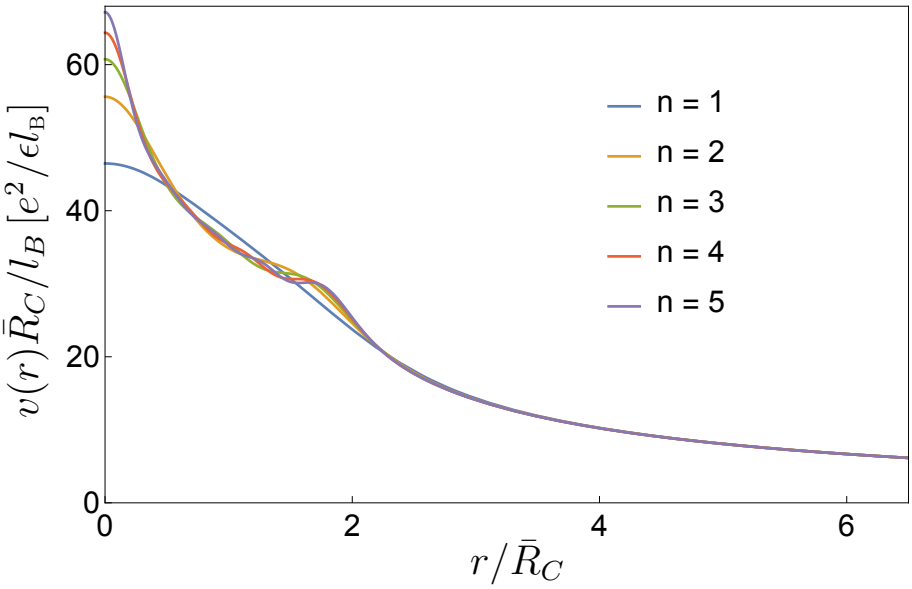

Figure 6.2: Effective scaled potential in graphene, using the most appropriate $\bar{R}_C$, which takes into account the mixing of Landau levels in graphene. The scaling parameters are defined in Eq. (6.7).

6.3 Electron-solid phases in graphene

As a first step in describing electron-solid phases in graphene, we consider a fully spin and valley polarized state, such that the interaction Hamiltonian reads

$$H = \frac{1}{2}\sum_{\boldsymbol{q}} v_n^g(q)\bar{\rho}(-\boldsymbol{q})\bar{\rho}(\boldsymbol{q}),$$

where $v_n^g(q)$ was defined in Eq. (6.5). Since the only difference between this Hamiltonian and the one we considered in the case of GaAs is captured by the effective potential, we can use precisely the same derivation as before to arrive at the Hartree-Fock Hamiltonian

$$H_{HF} = \frac{1}{2}\sum_{\boldsymbol{q}} u_n^{HF}(\boldsymbol{q})\langle\bar{\rho}(-\boldsymbol{q})\rangle\bar{\rho}(\boldsymbol{q}),$$

where

$$u_n^{HF}(\boldsymbol{q}) = v_n^g(q) - u_n^F(\boldsymbol{q}) \\ = v_n^g(q) - \frac{1}{N_B}\sum_{\boldsymbol{p}} v_n^g(p) e^{-i(p_y q_x - q_y p_x) l_B^2}. \tag{6.8}$$

The Fock exchange potentials $u_n^F(q)$ will also be different, since they depend on $v_n^g(q)$. The calculation of these potentials is straightforward, just like before and the explicit results are given in Appendix C.2. From this Hamiltonian, we can again calculate the cohesive energy and the expression will be the same as before in Eq. (5.14), apart from the Hartree-Fock potential that we have established already.

We can then plot the energies for the electronic phases in graphene. In Fig. 6.4, the Wigner crystal and the 2-electron-bubble phase are shown and compared with the usual results for GaAs in the $n = 1$ Landau level. The Wigner crystal phase (1-electron bubble) clearly has lower in energy in graphene than in GaAs for filling factors larger than 0.1, whereas the 2-electron-bubble phase in graphene has a higher energy for small filling factors and a lower energy for filling factors larger than 0.3, approximately. In Fig. 6.5, the relevant bubble phases in the $n = 2$ and $n = 3$ Landau levels in graphene are also shown. One common feature with the GaAs electronic phase diagram is that they seem to obey the empirical observation that in the n-th Landau level, there are $n + 1$ bubble phases, although this might be spoiled by other phases that can become the ground state near half filling. For example, in Fig. 6.5b, the 4-electron bubble is the ground state only in a very small regime near $\bar{\nu} = 0.5$. However, in that region, the striped phase often turns out to be the ground state and this could completely wash out the 4-electron-bubble phase in this Landau level.

One important comment regarding the energies near a filling of $\bar{\nu} = 1/2$ should be made. Recall that for the $n = 1$ Landau level in graphene, the effective potential was scale free and we concluded that there are then no bubble phases present. However, from Fig. 6.4, one might argue that the 2-electron-bubble phase has a lower energy than the Wigner crystal for filling factors slightly below 0.5. This contradiction arises from the fact that the system is in a very special regime near half-filling, where there can arise other kinds of solid phases that we have not discussed here, like a striped phase, or phases that need a whole different theory to describe them. To understand why the latter emerge, remember the composite fermion approach to describe states of fractional filling described in Section 3.5.2. We can make a composite fermion by attaching an even number of flux quanta to one electron. We then get an IQHE of composite fermions in an effective magnetic field $B^* = B - 2s\phi_0 n_{el}$, where $2s$ is the number of attached flux quanta. However, for a filling of $\bar{\nu} = 1/2$ there are two flux quanta for each electron, hence by forming composite fermions, there are no flux quanta left and we obtain an effective magnetic field $B^* = 0$. The system will behave as a Fermi liquid then, at least, in the lowest Landau level (for fillings $\nu = 1/2$ and $\nu = 3/2$). The projected Fermi-liquid state wave function was first written down by Rezayi and Read [48]. Since this wave function described a compressible state, there is no quantization of the Hall resistance at half filling in the lowest Landau level, which is in accordance with experiments [11]. In higher Landau levels, the Fermi liquid is unstable due to the wave function overlap of two interacting particles. Particles will tend to pair up, similar to Cooper pairing in superconductors. A wave function for this system was proposed by Moore and Read [49] and it includes a Pfaffian, which makes that these half-filled states in higher Landau

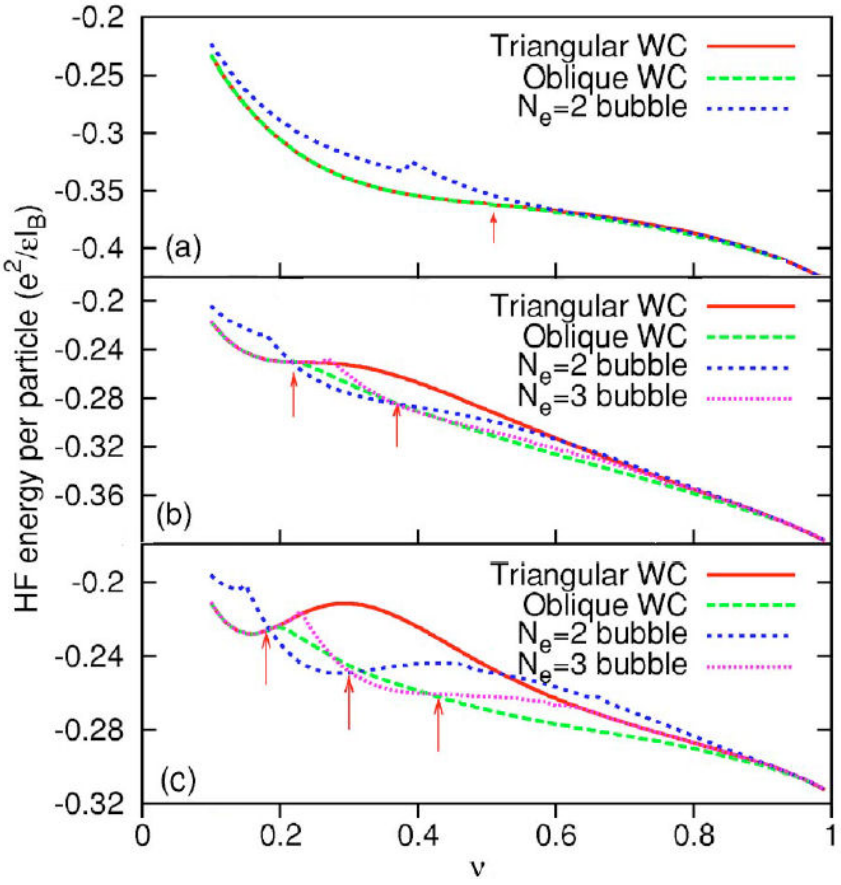

Figure 6.3: Numerical calculations of various electron-solid phases done by Zhang et al. [50] for graphene in the $n = 1$ (a), $n = 2$ (b) and $n = 3$ (c) Landau level. Figure extracted from Ref. [50].

levels are also referred to as Pfaffian states. A more rigorous description of these states is outside the scope of this thesis. We must just keep in mind that our theories do not apply in the half-filling regime.

When comparing our results to numerical calculations of the bubble energies using Green's functions [50], we can conclude that the results are in excellent agreement, as shown in Fig. 6.3. The transition points between the Wigner crystal and the various bubble phases are at the same filling factors. They also considered the oblique Wigner crystal, which becomes the ground state near half filling.

In Section 6.5, we will compare the results for the liquid phase and for all the solid phases in graphene to determine which phase has the lowest energy.

6.4 Electron-liquid phase in graphene

In order to derive the cohesive energy of the liquid phase in graphene, we follow the derivation done in Section 5.3. Two important ingredients in the derivation are the Laughlin wave function ψ_M and the plasma analogy that identifies $|\psi_M|^2$ with the Boltzmann factor. The energy is then straightforwardly derived like in classical, statistical physics. The question is now how this derivation will change if the electrons in consideration are those in graphene.

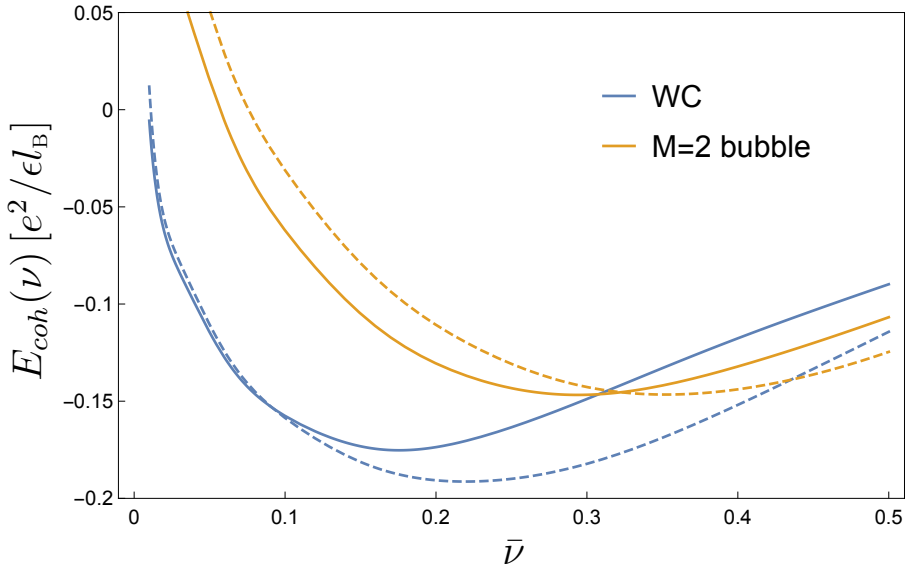

Figure 6.4: Cohesive energy of the $M = 1$ (Wigner crystal) and $M = 2$ bubble phases for normal 2DEGs (solid line) and graphene (dashed line) in $n = 1$ Landau level.

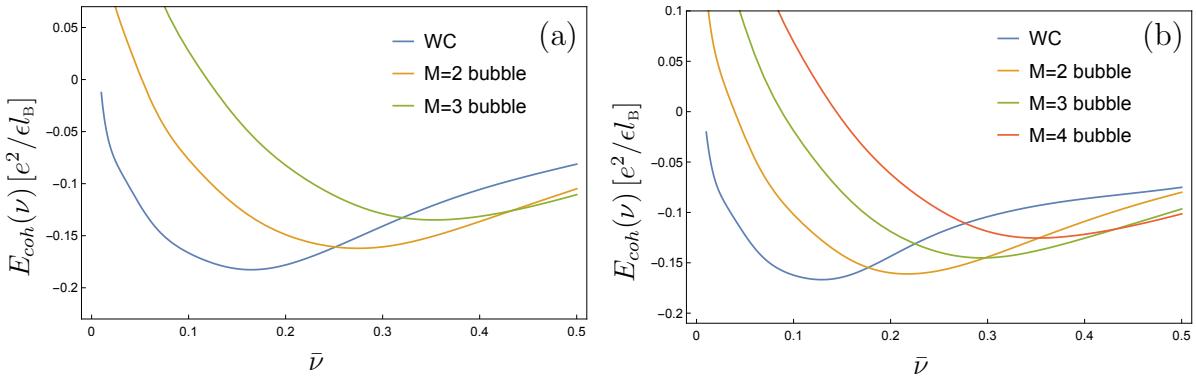

Figure 6.5: Various bubble phases in the $n = 2$ (a) and $n = 3$ (b) Landau level in graphene.

We expect that the Laughlin wave function will be the same in graphene, since it was postulated based on only a few general symmetry arguments, which are also present in graphene. In particular, in the derivation of this wave function, Laughlin did not use the fact that the electrons are either Schrödinger or Dirac electrons. We might expect that the wave function is thus just as valid in graphene as in GaAs. Furthermore, we can then employ the plasma analogy argument again to derive the cohesive energy in the same manner as before. The only thing that will change is the effective potential in Eq. (5.15). Thus, a change in the form factor is the only thing necessary to adjust the cohesive energy of the Laughlin liquid to the case of graphene, just like in the solid phase. Our results for the ground-state Laughlin-liquid energies in graphene are shown in Table 6.1. To be able to compare our findings to numerical calculations, we also compute the total ground-state energies, given by

$$E_{tot}(\nu) = E_{coh}(\nu) - \frac{\bar{\nu}}{2}\int dq\, F_n^2(q),$$

which was derived in Eq. (5.16). Table 6.2 shows the total ground-state energies calculated analytically for graphene in various Landau levels, compared with numerical calculations done by Zlatko Papic. Fig. 6.6 shows his exact diagonalization result in the $n = 0$, $n = 1$ and $n = 2$ Landau level. The $n = 0$ Landau level is the same as in GaAs, thus this can serve as a check to verify whether this numerical results also match with the GaAs case, which has been studied more extensively. Comparing these numerical results with our analytic calculations, we can conclude that they are in excellent agreement with each other, except for the $\bar{\nu} = 1/3$ case in the $n = 2$ Landau level. Later on, we will see that this can be explained by the existence of a bubble phase at that particular filling. Hence, the numerical calculations may not be accurate to describe the liquid phase in this case because it is not the ground state. We will see in the next section that of all the energies calculated numerically, this is indeed the only filling at which we expect the solid phase to be lower in energy than the liquid phase. Altogether, we can conclude that this theory to describe the FQHE in graphene is very accurate.

	$\bar{\nu} = 1/3$	$\bar{\nu} = 1/5$	$\bar{\nu} = 1/7$	$\bar{\nu} = 1/9$
$n = 1$	-0.2263	-0.2247	-0.2098	-0.1958
$n = 2$	-0.1463	-0.2025	-0.2012	-0.1917
$n = 3$	-0.1244	-0.1549	-0.1833	-0.1822

Table 6.1: Cohesive energies of the ground state of the Laughlin liquid phase in graphene (in units of $e^2/\epsilon l_B$) at different partial filling factors.

For the energies of the quasiparticle- and quasihole gaps, the situation is somewhat more involved. Since they are based on a very elaborate Hamiltonian theory [44, 45], it is presumably not enough to just change the form factor. For example, the multi-component character of the wave function becomes relevant and many equations will acquire a matrix form, which makes the problem significantly more complicated. Another reason to doubt that our analytical result will match numerical calculations is that for the case of GaAs, which was studied in Ref. [38], and which we have described in Chapter 5, it is known that the quasiparticle and quasihole energies calculated analytically using Murthy and Shankar's theory are actually quite far off numerical calculations. In Fig. 6.7, this is illustrated by a comparison of the gaps $\Delta = \Delta_{qp} + \Delta_{qh}$ calculated analytically by the Hamiltonian theory of Murthy and Shankar [45] and numerically by Park et al. [51] for a normal 2DEG in the lowest Landau level. It is plotted as a function of the thickness parameter λ, which appears in the so-called Zhang-Das Sarma potential as $v(q) = (2\pi e^2/\epsilon q)e^{-ql_B\lambda}$ [44]. It is basically a Coulomb interaction that takes into account the thickness of the sample. In the whole scope of this thesis, we use $\lambda = 0$, and evidently in graphene λ must be particularly small. From this figure, we see that for $\lambda = 0$

	$\bar{\nu} = 1/3$		$\bar{\nu} = 1/5$		$\bar{\nu} = 1/7$	
	analytic	numerical	analytic	numerical	analytic	numerical
$n = 0$	-0.409	-0.409 ± 0.001	-0.327	-0.327 ± 0.002	-0.280	-0.281 ± 0.003
$n = 1$	-0.370	-0.369 ± 0.001	-0.311	-0.311 ± 0.002	-0.271	-0.271 ± 0.004
$n = 2$	-0.265	-0.290 ± 0.002	-0.273	-0.273 ± 0.003	-0.252	-0.251 ± 0.005

Table 6.2: Comparison of our analytic results for the total ground state energies of the Laughlin liquid phase in graphene (in units of $e^2/\epsilon l_B$), with numerical results of Z. Papic.

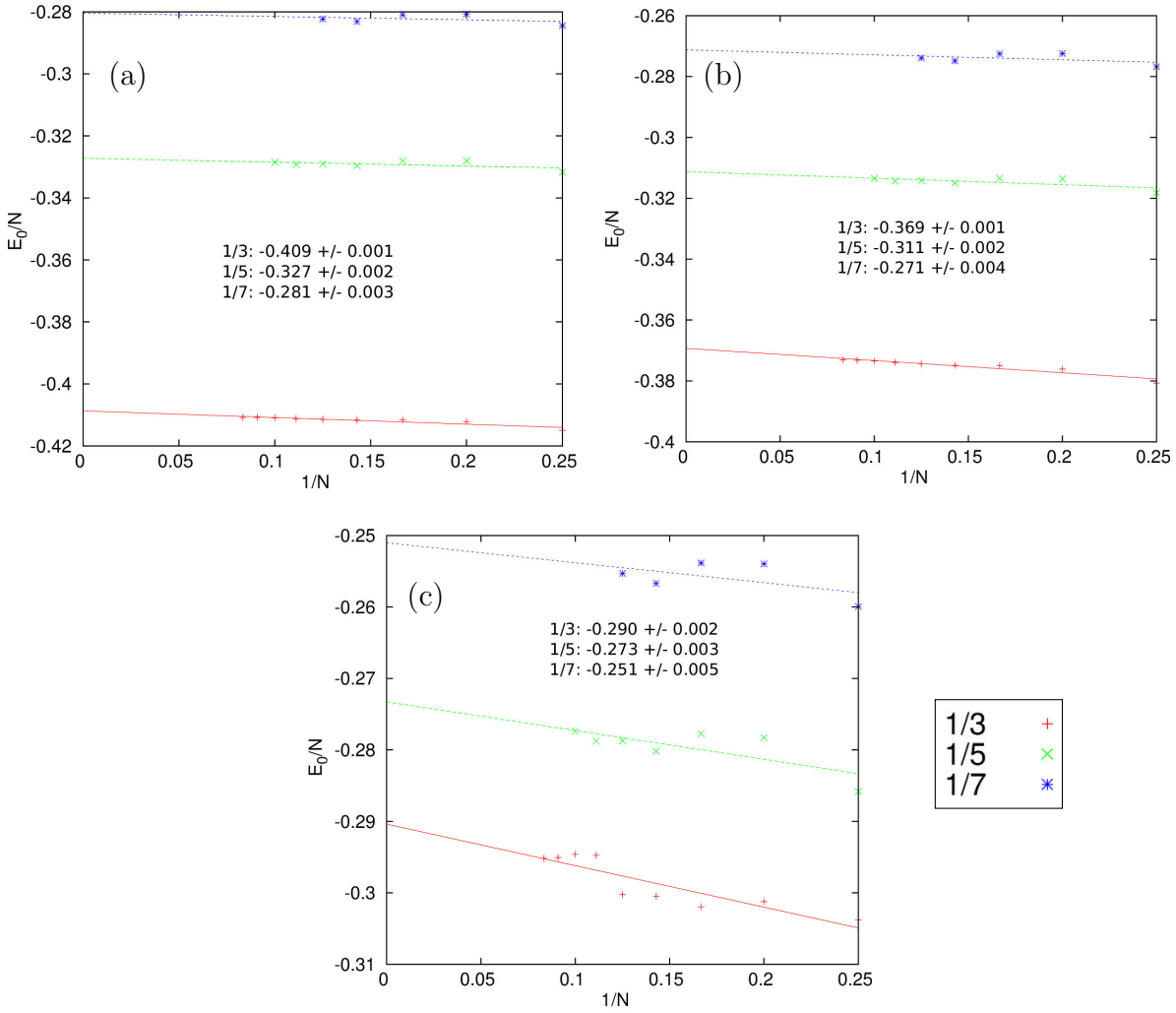

Figure 6.6: Numerical calculations for the ground state energy of the Laughlin liquid state in the $n = 0$ (a), $n = 1$ (b) and $n = 2$ (c) Landau levels. Inset values are obtained from extrapolations to the thermodynamic limit. Courtesy of Zlatko Papic.

the gap calculated with the Hamiltonian theory is twice as large as the numerical one. Remarkably though, the theory explained in Chapter 5 that uses the analytic results to compute the quasiparticle and quasihole energies agrees extremely well with experimental measurements [52]. This is the main reason why we attempt at these calculations, in any case.

In the next section, we will plot all the energies for the various phases and we will also include the quasiparticle and quasihole gaps that we calculated, keeping in mind that they may not be very accurate.

6.5 Competition between electron-phases in graphene

We will now compare the energies of the solid phases with those of the liquid phase to determine the phase diagram in various Landau levels. Remember that in the lowest Landau level the form factor in graphene is the same as in GaAs. Since the energies were calculated using an effective theory, in which the special behavior of the electrons

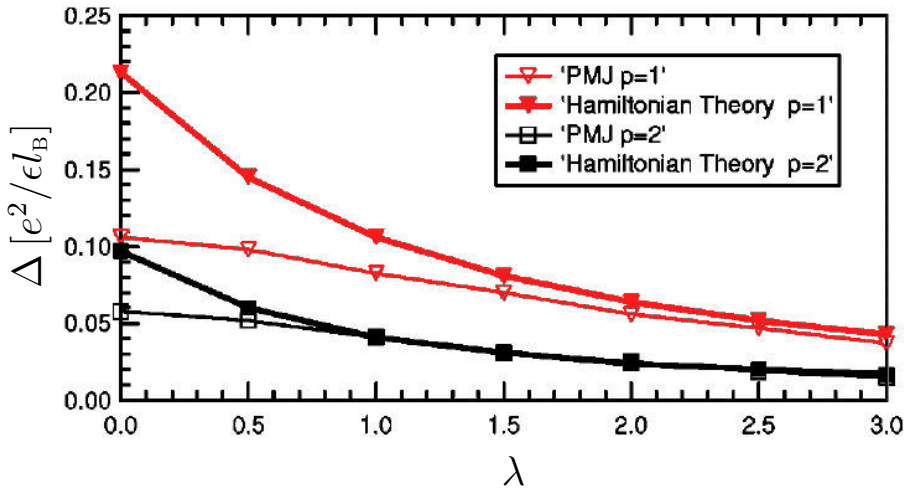

Figure 6.7: Quasiparticle-/hole gaps in the lowest Landau level calculated analytically using the Hamiltonian theory of Murthy and Shankar and numerically by Park et al. The $p = 1$ case corresponds to a filling $\bar{\nu} = 1/3$. Figure from Ref. [44].

in graphene was completely captured by the form factor, the phase diagram in the lowest Landau level in graphene is the same as in GaAs (see Fig. 5.4).

For the $n = 1$ Landau level, the results are shown in Fig. 6.8. In principle, the Laughlin liquid energies are always lower than those for the Wigner crystal (blue solid line) or bubble phase (orange solid line). Away from the filling factors $\bar{\nu} = 1/(2s + 1)$, the liquid energies might be a bit higher, but it is very unlikely that they will exceed the electron-solid energies. However, as we have seen before, impurities in the sample lower the energy of the electron-solid phases, while letting the energies of the electron-liquid phase basically untouched. This is depicted in Fig. 6.8 by the dashed lines, for the same impurity potential strengths as we considered before ($E_{pin} = 2.5 \cdot 10^{-5}$ and $E_{pin} = 10^{-4}$). The $\bar{\nu} = 1/3$ and $\bar{\nu} = 1/5$ liquid state are nevertheless still lower in energy. However, for a strong impurity potential the Wigner crystal phase can become the lowest in energy for small filling factors. a reentrant behavior, where solid and liquid phases alternate with each other, is also conceivable if the impurity potential is very strong, but it is most likely that there are no solid phases whatsoever in this Landau level. This case is actually quite similar to the lowest Landau level. This resemblance is understandable because the form factor in graphene is a combination of the n-th and the $(n-1)$-th form factor of GaAs, hence the lowest Landau level behavior may dominate in this case.

For the $n = 2$ Landau level (see Fig. 6.9), the FQHE does not occur at $\bar{\nu} = 1/3$, since the 2-electron-bubble phase is lower in energy. The other FQH states might be visible, but the dashed lines in Fig. 6.9 show that if there are a lot of impurities in the sample, the FQH states at low fillings might be dominated by the Wigner crystal. The $\bar{\nu} = 1/5$ state seems to be the most likely to occur in the $n = 2$ Landau level. For filling factors within the range $0.2 - 0.32$ there might also be a Wigner crystal coexisting with a 2-electron bubble.

For the $n = 3$ Landau level, the $\bar{\nu} = 1/3$ and the $\bar{\nu} = 1/5$ Laughlin states are always higher in energy than the bubble phases, thus they will not be visible. The FQH states at lower fillings may only be seen in very clean samples, as indicated by the dashed lines in Fig. 6.10. At higher filling factors, there are 2-electron-, 3-electron- and possibly 4-electron bubbles appearing and perhaps also coexisting.

Although charge-density waves have been observed in graphene, the underlying mechanisms are very different to the one described in this thesis. For example, charge-density waves were observed in twisted graphene layers [53]. However, in graphene, there have been no experimental signs thus far of a charge-density wave that arises due to electronic interactions in a quantum Hall system. This is expected for the lowest two Landau levels, but in the $n = 2$ Landau level, we certainly expect crystal phases at filling factors above about 0.3.

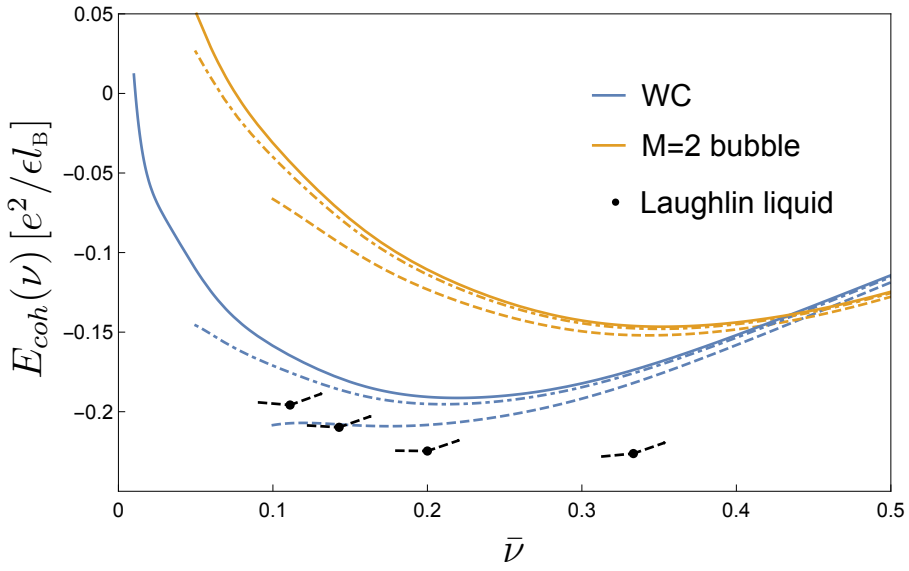

Figure 6.8: Solid and liquid phases in the $n = 1$ Landau level in graphene. The dashed lines are the energies when taking impurities into account.

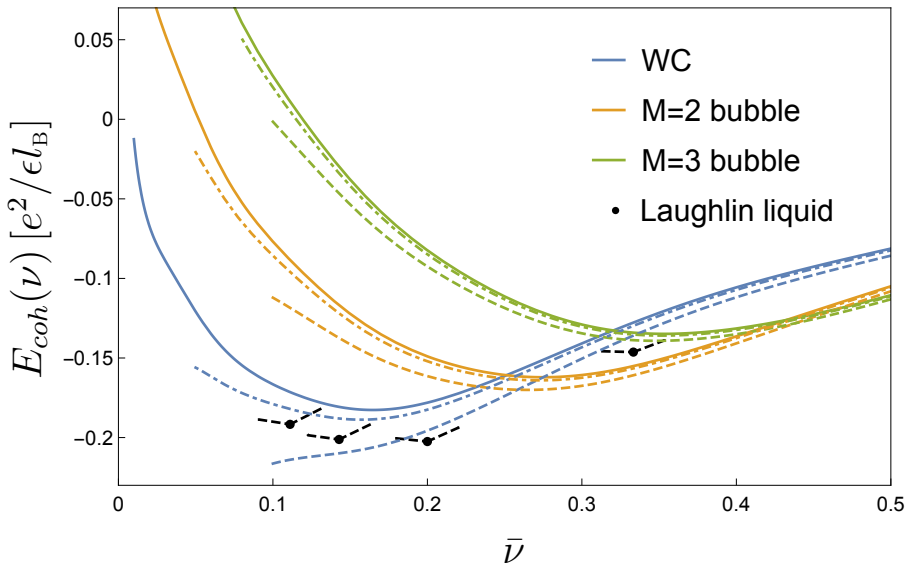

Figure 6.9: Solid and liquid phases in the $n = 2$ Landau level in graphene. The dashed lines are the energies when taking impurities into account.

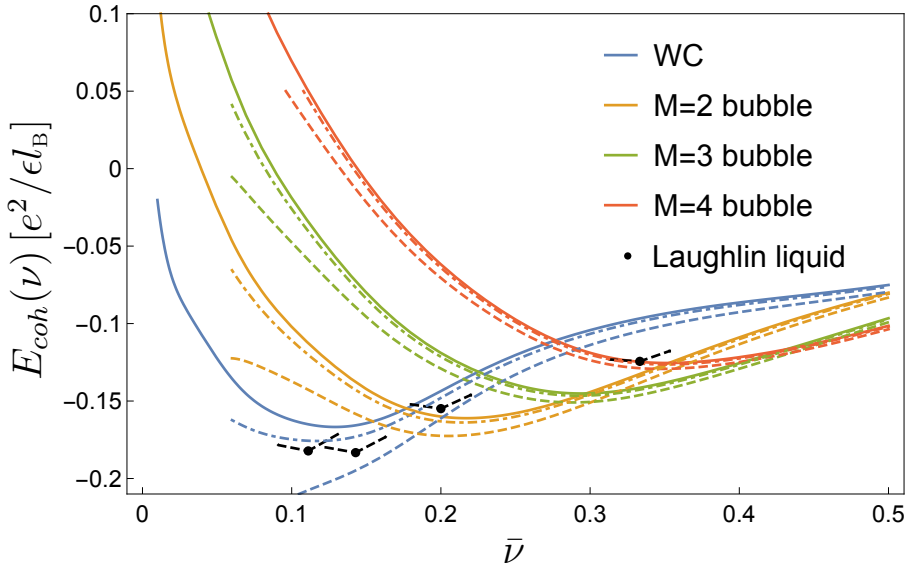

Figure 6.10: Solid and liquid phases in the $n = 3$ Landau level in graphene. The dashed lines are the energies when taking impurities into account.

6.5.1 The effect of Landau level mixing

Besides sample impurities, there are some other factors that can have an influence on the energies of the liquid- and solid phases. One of them is Landau level mixing. Thus far, we have assumed that there are no inter-Landau-level excitations. All dynamics is restricted to one single Landau level. However, if the Coulomb interaction energy becomes of the same order as the inter-Landau-level separation $\hbar v_F/l_B$, then these excitations can have a considerable probability, even if the a Landau level is only partially filled. This probability is related to the mixing parameter κ, defined by

$$\kappa = \frac{e^2/\epsilon l_B}{\hbar v_F/l_B} = \frac{e^2}{\epsilon \hbar v_F}.$$

The only parameters that determine the value of κ are the Fermi velocity v_F and the dielectric constant ϵ. These are material properties, which depend on the substrate. For free-standing graphene, $\kappa \approx 2.2$, while on substrates, such as SiO_2 or BN, it takes slightly lower values $\kappa \approx 0.9$ and $\kappa \approx 0.5 - 0.8$ respectively [54]. In Ref. [54], the effect of Landau level mixing in graphene on the Laughlin liquid states in the $\bar{\nu} = 1/3$ case is investigated in the $n = 0$ and $n = 1$ Landau level. This effect turns out to be negligible for $\kappa \lesssim 2$ in the lowest Landau level and for $\kappa \lesssim 1$ in the $n = 1$ Landau level. Hence, for not too large values of κ most states will be unaffected. However, this Landau level mixing breaks particle-hole symmetry, thus the presence of a FQH state at $\bar{\nu} = 1/3$ does not automatically imply one at $\bar{\nu} = 2/3$.

For the solid phases, we resort to Ref. [55], in which the authors have investigated the validity of the single-Landau-level approximation. In turns out that there are no qualitative changes in the phase diagram, e.g., in the $n = 2$ Landau level there are still phase transitions from Wigner crystal to 2-electron bubble and then to 3-electron bubble, but these transitions might occur at slightly different filling factors. Furthermore, the cohesive energies stay in the same range as they were (within about 10%). As a last remark, we note that the inter-Landau-level spacing becomes smaller for higher Landau

levels, since it scales like $\sqrt{n+1}-\sqrt{n}$, which goes to zero for increasing n, and we might argue that Landau-level mixing then becomes dominant. However, in Ref. [55] it was also shown that this argument is too simplistic, and it turns out that the single-Landau-level approximation stays in fact applicable, even for large n.

Lastly, it is important not to confuse the notion of Landau-level mixing with the fact that the form factor in graphene is a sum of the usual form factors in the n-th and $(n-1)$-th Landau level. In a sense, it mixes two consecutive Landau levels, but this is not the kind of mixing that we refer to in the previous arguments. Even if the form factor has these two terms, it still assumes that there are no inter-Landau-level excitations.

6.6 Conclusion

We have seen that graphene placed in a perpendicular magnetic field has a different wave function than a usual 2DEG. Due to the two valleys in graphene, the wave function has two components, which is reflected in the fact that the effective form factor in graphene consists of a sum of the regular form factors in the n-th and $(n-1)$-th Landau level. To derive the phase diagram of a partially filled Landau level in graphene, it is sufficient to adjust only the form factor and use the same methods as for normal 2DEGs. Since we ignore inter-Landau-level excitations, the kinetic energy is constant and thus we can model the system solely by the Coulomb interaction between the electrons. The different dispersion of graphene therefore does not play an important role. By deriving the cohesive energies of the Wigner crystal phase, various bubble phases and the Laughlin liquid phases, we were able to compare them and construct the phase diagram in the first four Landau levels.

In the lowest Landau level, the form factor of graphene is the same as in usual 2DEGs, and hence the phase diagram is the same. The absence of a length scale in the effective potential ensures that there are no bubble phases. Furthermore, the liquid state is always lower than the Wigner crystal, hence in the lowest Landau level there are no solid phases.

In the $n=1$ Landau level, the liquid phase is in principle lower in energy than the solid phases. However, impurities in the sample might lower the solid energies and Wigner crystal formation might be possible at low filling factors ($\bar{\nu} \lesssim 0.15$), which should simply enlarge the IQH plateau. Since the effective potential for graphene is also scale free for $n=1$, there are no bubbles phases.

In the $n=2$ Landau level, the 2-electron-bubble phase is lower in energy than the $\bar{\nu}=1/3$ Laughlin liquid state. The other FQH states can be seen if the sample has not too many impurities. The $\bar{\nu}=1/5$ is expected to be the most stable. In this Landau level, we certainly expect to see a 2-electron-bubble phase, liquid phase and possibly a Wigner crystal for low fillings and perhaps a 3-electron bubble around half-filling, although we cannot say much about that regime due to its special character.

In the $n=3$ Landau level, we expect a 2-electron bubble, a 3-electron bubble and possibly a 4-electron bubble in the regime $0.18 < \bar{\nu} < 0.5$. For small fillings, it is likely that the FQH states at $\bar{\nu}=1/7$ and $\bar{\nu}=1/9$ might be present if the sample is clean enough. Otherwise, the Wigner crystal will be lower in energy.

Chapter 7

Hydrodynamical description of a quantum Hall system

Having explained the electronic properties of graphene and the phenomena that can arise in two-dimensional electron systems due to interactions between electrons, we will now focus on the hydrogenated graphene experiment. As explained in Chapter 2, an AFM measurement of the sample reveals islands with fractal-like structures. The origin of these islands is not evident yet. However, we have reasons to perceive them as patterns in the charge distribution (see Chapter 2), meaning that there is some mechanism that causes the electrons to cluster into islands and form these fingered patterns. An additional motivation for this belief stems from an article by Agam et al. [4], which provides a theory that could explain this underlying mechanism. In short, they prove that an electronic droplet in the quantum Hall regime can form these fingered islands if there is an additional inhomogeneous magnetic field outside the droplet. This system behaves similar to two classical fluids confined in a two-dimensional geometry, one with a small viscosity that is injected into a more viscous one (see Fig. 7.1). The growth process of these fingered structures is called Laplacian growth. In the hydrogenated graphene experiment, this inhomogeneous magnetic field can be provided by a pseudo-magnetic field that arises from deformations in the graphene sheet. The hydrogen, together with the underlying substrate, can cause these deformations.

In Section 7.1, we will elaborate on the process of viscous fingering and explain the theory that connects this classical problem to quantum Hall liquids. In Section 7.2, we will show how this theory can be applied to predict the shape of these electronic droplets. Lastly, in Section 7.3, we will explain in more detail how deformations in graphene can lead to pseudo-magnetic fields.

Figure 7.1: Viscous fingering in a Hele-Shaw cell. Figures from Ref. [1].

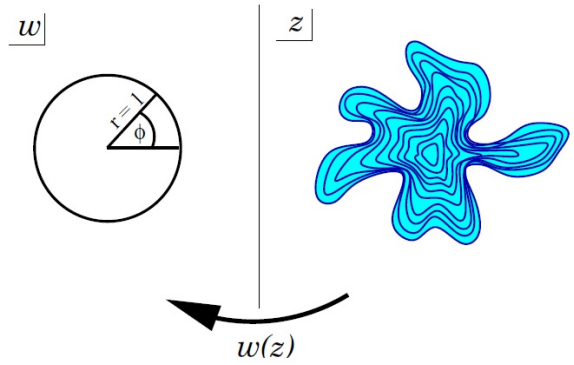

Figure 7.2: The map $w(z)$ maps the exterior of the droplet to the exterior of the unit disk.

7.1 Viscous fingering of electronic droplets

The fingering patterns that arise in the experiment illustrate a Laplacian growth process. This phenomenon is ubiquitous in nature and can be found, for instance, in the formation of snow flakes, riverbeds or bacterial colonies. The underlying mechanism that generates this growth process can be different in each case. The class of viscous fingering is one of the most studies forms of Laplacian growth. It is also referred to as the Saffman-Taylor problem. In the classical version, a viscous fluid is confined between two glass plates called a Hele-Shaw cell, and a less viscous fluid is then injected into the more viscous one. The velocity with which the injected fluid propagates is proportional to the gradient of the pressure. This relation is called D'Arcy's law: $\boldsymbol{v} = -\nabla p$, and it characterizes Laplacian growth. Indeed, if we assume incompressibility of the fluids, then the density $\rho(\boldsymbol{r}, t) = \rho$ is constant and hence we can use the continuity equation

$$-\nabla \cdot [\rho(\boldsymbol{r}, t)\boldsymbol{v}(\boldsymbol{r}, t)] = \partial_t \rho(\boldsymbol{r}, t),$$

to derive that $\nabla \cdot \boldsymbol{v} = 0$. Using D'Arcy's law, we then obtain the Laplace equation $\nabla^2 p = 0$. If we assume that the difference between the viscosities is large and if we ignore surface tension, then the pressure is constant in the less viscous fluid and on the interface $\mathcal{C}$. Hence, $v_n(z) = -\delta_n p(z)$ for $z \in \mathcal{C}$ and n denoting the outward direction normal to the interface. We will present the ingredients to proof that D'Arcy's law also holds for an electronic droplet in the quantum Hall regime under the influence of an inhomogeneous magnetic field outside the droplet. For the complete proof, we refer to Ref. [4].

Firstly, we consider the case of two classical fluids. To model the shape of the droplet, it is common to use complex coordinates $z = x + iy$ and a conformal map $w(z)$. As shown in Fig. 7.2, $w(z)$ maps the exterior of the droplet (which we call D_{ex}) to the exterior of the unit disk (called U_{ex}), which can be done according to the Riemann mapping theorem. At a certain time t, the boundary of the droplet can be parametrized by a curve $\gamma_t : [a, b] \subset \mathbb{R} \to \mathbb{C}$. The map $w(z, t)$ maps, at time t, each point z in D_{ex} to some point $w(z)$ in U_{ex}. It can be shown that $w(z)$ extends continuously to the boundary of its domain[1], such that the interface of the droplet is mapped to the unit circle.

[1]This is Carathéodory's theorem, which states that if U is a simply connected open subset of the complex plane $\mathbb{C}$, whose boundary is a Jordan curve Γ, then the Riemann map $f : U \to D$ from U to the unit disk D extends continuously to the boundary, giving a homeomorphism $F : \Gamma \to S^1$ from Γ to the unit circle S^1.

One important tool in handling Laplacian growth problems are harmonic moments. These are integrals of integer powers of z over some domain. In this case, the harmonic moments of the exterior of the droplet are given by

$$t_k = -\frac{1}{\pi k} \int_{D_{ex}} z^{-k} d^2 z.$$

One of the reasons why we use these integrals is that they characterize the shape of the droplet, which is what we are interested in, since we want to investigate how the droplet grows. Secondly, it can be shown that D'Arcy's law holds if and only if the harmonic moments are constants of motion, i.e., $\partial_t t_k = 0$ [4]. Hence, if we want to show that an electronic droplet in the quantum Hall regime under the influence of an inhomogeneous magnetic field outside of the droplet satisfies D'Arcy's law, it is sufficient to show that the harmonic moments of the droplet do not depend on time. This problem can then be seen as a quantum mechanical version of the Saffman-Taylor problem.

Next, we will set up the quantum mechanical problem, as done in Ref. [4]. We consider a constant magnetic field B_0 perpendicular to the plane, situated in a disk of radius R_0. The disk is surrounded by an annulus $R_0 < |z| < R_1$, in which there is a magnetic field B_1, which is directed opposite to B_0, such that the total flux Φ of the whole disk $|z| < R_1$ is equal to $N\phi_0$, where ϕ_0 is the elementary flux quantum. Inside the inner disk, there is some potential that confines N electrons in a circular droplet, such that the lowest Landau level is completely filled. Here, we neglect the interactions between the electrons. One can tune the magnetic field B_1 to ensure that the radius of the droplet R_D is much smaller than R_0 (see Fig. 7.3). In Section 3.3.3, we have derived that electrons in a perpendicular magnetic field in the lowest Landau level are performing a cyclotron motion around a guiding center, which is located on a circle with radius $l_B\sqrt{2m+1}$, where m is the quantum number associated to the degeneracy of the Landau level. We have shown that the maximum value that m can take is N_B. If the lowest Landau level is completely filled, the total filling $\nu = N/N_B$ is equal to 1, which implies that $N_B = N$. We can thus write the radius of the droplet as $R_D = l_B\sqrt{2N+1}$, where N is the number of electrons. Next, one places a nonuniform magnetic field δB inside the disk, but away from the droplet ($\delta B = 0$ inside the droplet), such that the total flux is unchanged by this field, i.e., $\int d^2z\, \delta B(z) = 0$. Note that this nonuniform magnetic field must thus have both positive and negative components. The number of states per Landau level is $N_B = AB/\phi_0$, where A is the area of the total disk. We assume that the lowest Landau level always stays completely filled, thus by tuning B_1, while keeping the other fields fixed, one can then increase the number of electrons.

Consider the Hamiltonian of these spin polarized electrons in a perpendicular magnetic field,

$$H = \frac{1}{2m}(-i\hbar\nabla - e\boldsymbol{A})^2 - \mu_B B.$$

The wave functions can be written in the Coulomb gauge (i.e., $\nabla \cdot \boldsymbol{A} = 0$) as $\psi_n(z) = P_n(z)e^{-W(z)/\hbar}$, where $W(z)$ is the potential that obeys $B = -\nabla^2 W$ and $P_n(z)$ is some holomorphic polynomial [4]. The total wave function of the droplet can then be written as

$$\Psi(z_1, \cdots, z_N) = \frac{1}{\sqrt{N!\tau_N}} \prod_{n<m<N} (z_n - z_m)\, e^{\frac{1}{\hbar}\sum_n W(z_n)},$$

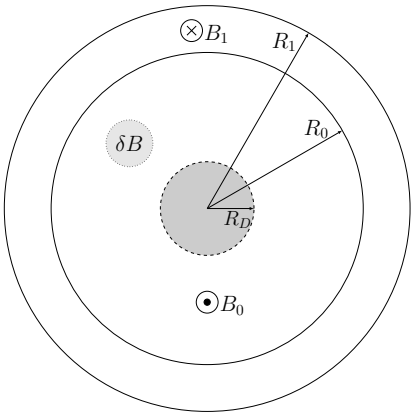

Figure 7.3: Schematic set-up of the electronic droplet with radius R_D, placed in a disk of radius R_0 (with magnetic field B_0), surrounded by an annulus $R_0 < |z| < R_1$ (with magnetic field B_1). Outside the droplet there is an inhomogeneous magnetic field δB.

where τ_N is some proportionality constant. To take into account the nonuniform part of the magnetic field, one considers its potential V, defined by $\delta B = -\nabla^2 V$. The following equations that determine this potential will be the most important ones in understanding the fingering problem:

$$V(z) = \frac{1}{2}\mathrm{Re}\sum_{k\geq 1} t_k z^k \qquad \text{for } z \in D_{in} \tag{7.1}$$

$$t_k = \frac{1}{\pi k}\int_{D_{ex}} \delta B(z) z^{-k} d^2 z \tag{7.2}$$

From this equations, one can see how the nonuniform magnetic field influences the shape of the droplet. Notice that t_k are the harmonic moments of the deformed part of the magnetic field. The integral runs over the exterior of the droplet. Furthermore, we can see that although $\delta B = 0$ *inside* the droplet[2], $V(z)$ is non-zero there and depends on the harmonic moments of the region *outside* the droplet. The electrons in the droplet are thus influenced by this potential $V(z)$ that arises due to distant homogeneities in the magnetic field. This effect is called the Aharonov-Bohm effect and is purely quantum mechanical [56]. Intuitively, one can say that in the quantum-mechanical description, the electrons are not completely localized inside the droplet, but they also have a small, yet finite, probability of exploring the regions outside the droplet. Hence, they can indeed be influenced by the nonuniform magnetic field far away from the droplet.

Here, we will not go into details of the proof that these harmonic moments t_k are constants of motion (which prompts D'Arcy's law), but refer the reader to Ref. [4]. We will rather use Eqs. (7.1) and (7.2) to make some more explicit calculations regarding the evolution of the droplet's shape, in the following section.

7.2 The shape of the droplet

Having set up the theoretical tools to handle Laplacian growth problems, we proceed to work out an explicit example, to obtain a better intuition about how these fingering

[2]This can indeed be verified by calculating $\delta B = -\nabla^2 V = -4\partial_z\partial_{\bar{z}} V(z,\bar{z}) = -\partial_z\partial_{\bar{z}}\sum_{k\geq 1}(t_k z^k + t_k \bar{z}^k) = 0$.

patterns emerge. In this section, we will follow Ref. [57].

We consider a potential of the form

$$V(z) = \frac{1}{2}\mathrm{Re}\left(t_{M+1} z^{M+1}\right), \tag{7.3}$$

where M is some positive integer. By choosing a simple potential, the corresponding conformal map that sends the boundary of the droplet to the unit circle also has a simple form [57],

$$z(w) = r_M w + u_M w^{-M}, \tag{7.4}$$

where r_M and u_M are real functions of N, which can be related to Eq. (7.3) by

$$t_{M+1} = \frac{u_M}{(M+1) r_M^M}, \qquad N = \frac{r_M^2 - M u_M^2}{2}. \tag{7.5}$$

If the potential $V(z)$ is given, i.e., if t_{M+1} is fixed, Eq. (7.4), together with Eq. (7.5), are sufficient to describe the evolution of the droplet, as the number of electrons N is increasing. We will consider the cases $M = 1$ and $M = 2$ explicitly and subsequently prove some statements about the evolution of the droplet for general M.

First, consider $M = 1$. We will show that this corresponds to an ellipse with constant eccentricity. For this case, Eq. (7.5) reads

$$t_2 = \frac{u_1}{2r_1}, \qquad N = \frac{r_1^2 - u_1^2}{2}.$$

From this, we can derive $r_1(N)$ and $u_1(N)$ as function of N for constant t_2,

$$r_1(N) = \frac{\sqrt{2N}}{\sqrt{1 - 4t_2^2}}, \qquad u_1(N) = \frac{2t_2\sqrt{2N}}{\sqrt{1 - 4t_2^2}}.$$

The shape of the droplet is given by Eq. (7.4). Its maps the unit circle into the boundary of the droplet. The unit circle can be parametrized as $w(t) = e^{it}$, for $0 \leq t \leq 2\pi$. The interface of the droplet is then parametrized by

$$z^B_{M=1}(N) = [r_1(N) + u_1(N)]\cos(t) + i[r_1(N) - u_1(N)]\sin(t), \qquad 0 \leq t \leq 2\pi.$$

In Fig. 7.4, the interface is shown for various values of N. Be careful not to confuse t with time. Here, t is used to parametrize the boundary of the droplet, whereas the number of electrons N basically serves as the time variable, since electrons are injected into the droplet at a constant rate.

For $M = 2$, the droplet grows in a more irregular way. We will see that it starts developing cusps, i.e., singularities appear at the boundary of the droplet. Repeating the same procedure as in the previous case, we obtain

$$z^B_{M=2}(N) = [r_2(N)\cos(t) + u_2(N)\cos(2t)] + i[r_2(N)\sin(t) - u_2(N)\sin(2t)], \qquad 0 \leq t \leq 2\pi,$$

where

$$r_2(N) = \frac{\sqrt{1 - \gamma(N)}}{6t_3}, \qquad u_2(N) = \frac{1 - \gamma(N)}{12t_3},$$

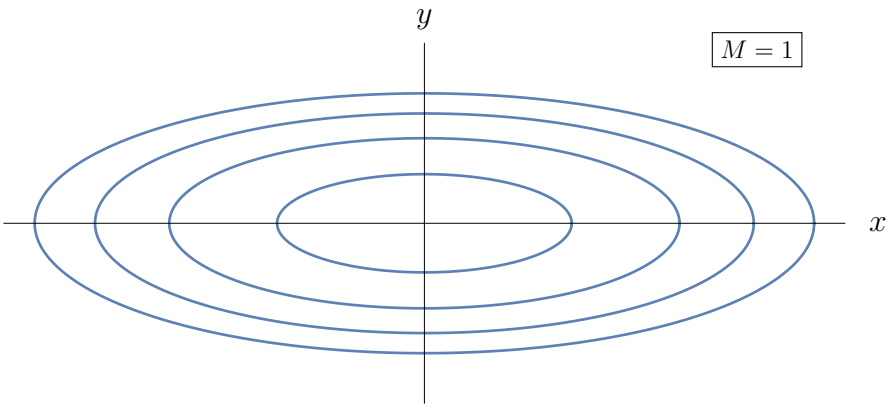

Figure 7.4: For $M = 1$, the droplet is an ellipse that grows as the number of electrons in increased.

with $\gamma(N) = \sqrt{1 - 144t_3^2 N}$. In Fig. 7.5, the evolution of the boundary of the droplet into cusps is shown.

For general $M \geq 2$, it turns out that the boundary simultaneously develops $M + 1$ cusps at some critical number of electrons N^*, such that it has an $(M+1)$-fold rotational symmetry. In Appendix D.1, we derive this critical point to be

$$N^* = \frac{1}{2}(M-1)M^{-(M+1)/(M-1)}[(M+1)t_{M+1}]^{-2/(M-1)}. \tag{7.6}$$

Furthermore, it can also be shown that a finger at position $x(N)$ for $N \lesssim N^*$, grows into a cusp at position $x^* = x(N^*)$,

$$x^* - x(N) = \frac{2}{\sqrt{M-1}}\sqrt{N^* - N} + \mathcal{O}(N^* - N). \tag{7.7}$$

The speed dx/dN at which the finger approaches the singularity is universal, in the sense that is does not depend on t_{M+1}.

For $M > 2$ it is very difficult, if not impossible, to derive an analytic expression for the boundary $z_M^B(t)$. However, it is possible to reconstruct the growth process by Monte Carlo simulations. This can be done by using the plasma analogy, which we have introduced already in Section 3.5.1. We identify the probability density of the electron droplet $|\Psi_M|^2$ with the Boltzmann factor $e^{\beta U_{cl}}/N!\tau_N$, where

$$U_{cl} = -\sum_{i<j} \ln|z_i - z_j| + \sum_{i=1}^{N} \left[|z_i|^2/4 - V(z_i)\right].$$

Thus, if the potential $V(z)$ is known, we can in principle determine the evolution of the droplet by using Monte Carlo simulations.

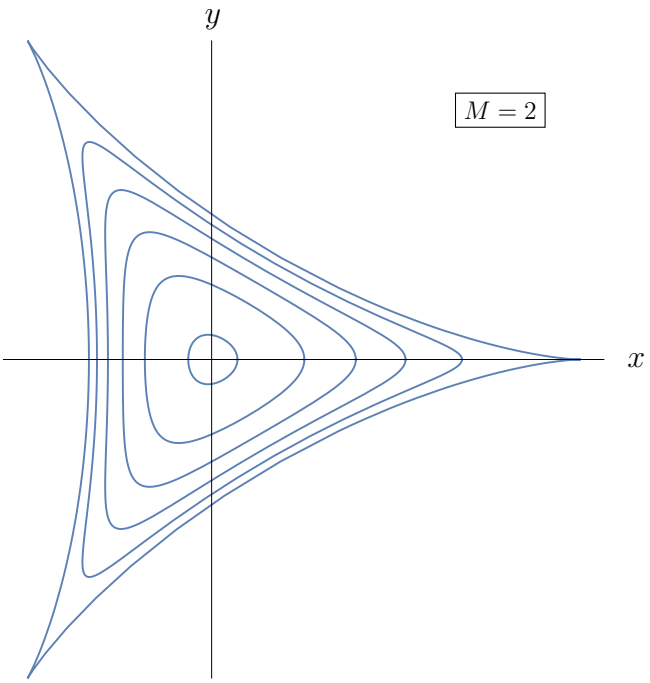

Figure 7.5: As the number of electrons in the droplet is increasing, the boundary develops cusps at some critical N^*.

7.3 Pseudomagnetic fields in graphene

Before we can apply any of these theories to the hydrogenated graphene experiment, we must first investigate how corrugations in graphene, which arise due to a combination of the hydrogen atoms and the substrate, can lead to a pseudo-magnetic field. Indeed, in 2010, it was experimentally shown that the strain from a nanobubble in an otherwise flat sheet of graphene may lead to a pseudo-magnetic field with a strength greater than 300 T [58].

Each site x_α of the graphene unperturbed lattice is shifted by $u_\alpha(\{x_\beta\})$, such that the total displacement is small in comparison with the inter-atomic distance, $|\boldsymbol{u}| \ll a$. The deformed coordinates are given by

$$x'_\alpha = x_\alpha + u_\alpha, \tag{7.8}$$

for $\alpha = x, y, z$. The distance between infinitesimally distant points changes then from

$$dl^2 = dx_\alpha dx_\alpha$$

to

$$\begin{aligned} dl'^2 &= dx'_\alpha dx'_\alpha \\ &= \frac{\partial x'_\alpha}{\partial x_\beta}\frac{\partial x'_\alpha}{\partial x_\gamma} dx_\beta dx_\gamma, \end{aligned}$$

where $\beta, \gamma = x, y$ since they correspond to the coordinates of the original, flat graphene surface, which has no dz component. Furthermore, we sum over repeated indices. Sub-

stituting Eq. (7.8) for x'_α, we obtain

$$\begin{aligned} dl'^2 &= \left(\frac{\partial x_\alpha}{\partial x_\beta} + \frac{\partial u_\alpha}{\partial x_\beta}\right)\left(\frac{\partial x_\alpha}{\partial x_\gamma} + \frac{\partial u_\alpha}{\partial x_\gamma}\right) dx_\beta dx_\gamma \\ &= \left(\frac{\partial x_\alpha}{\partial x_\beta}\frac{\partial x_\alpha}{\partial x_\gamma} + \frac{\partial x_\alpha}{\partial x_\beta}\frac{\partial u_\alpha}{\partial x_\gamma} + \frac{\partial u_\alpha}{\partial x_\beta}\frac{\partial x_\alpha}{\partial x_\gamma} + \frac{\partial u_\alpha}{\partial x_\beta}\frac{\partial u_\alpha}{\partial x_\gamma}\right) dx_\beta dx_\gamma \\ &= dl^2 + \left(\delta_{\alpha,\beta}\frac{\partial u_\alpha}{\partial x_\gamma} + \delta_{\alpha,\gamma}\frac{\partial u_\alpha}{\partial x_\beta} + \frac{\partial u_\alpha}{\partial x_\beta}\frac{\partial u_\alpha}{\partial x_\gamma}\right) dx_\beta dx_\gamma \\ &= dl^2 + \left(\frac{\partial u_\beta}{\partial x_\gamma} + \frac{\partial u_\gamma}{\partial x_\beta} + \frac{\partial u_\alpha}{\partial x_\beta}\frac{\partial u_\alpha}{\partial x_\gamma}\right) dx_\beta dx_\gamma. \end{aligned}$$

By interchanging the dummy indices α and γ, we can write this results as

$$dl'^2 = dl^2 + 2u_{\alpha\beta} dx_\alpha dx_\beta,$$

where

$$u_{\alpha\beta} = \frac{1}{2}\left(\frac{\partial u_\alpha}{\partial x_\beta} + \frac{\partial u_\beta}{\partial x_\alpha} + \frac{\partial u_\gamma}{\partial x_\alpha}\frac{\partial u_\gamma}{\partial x_\beta}\right) \tag{7.9}$$

is the deformation tensor.

Since each point in the graphene lattice is shifted, the hopping amplitudes for the three nearest neighbors will not be a constant. It will in fact be a different value for each nearest neighbor (ignoring next-nearest-neighbor hoppings). The change in the hopping amplitudes can be included in the Hamiltonian by writing [59]

$$H = \boldsymbol{\sigma} \cdot \left(-i\hbar v_F \nabla - \boldsymbol{A}\right), \tag{7.10}$$

where $\boldsymbol{\sigma}$ is a vector of Pauli matrices. The first term in this Hamiltonian is the usual Hamiltonian for flat graphene, as derived in Eq. (4.16). The second term is the contribution to the Hamiltonian from the deformations. Its components relate to the deformation tensor by [59]

$$A_x = c\beta t \left(u_{xx} - u_{yy}\right), \tag{7.11}$$

$$A_y = -2c\beta t\, u_{xy}, \tag{7.12}$$

where $\beta = -\partial \ln t / \partial \ln a$ is the so-called electron Grüneisen paramter. It is a dimensionless property of the crystal and for graphene it is approximately $\beta \approx 2 - 3$ [60]. Furthermore, c is some numerical constant, which depends on the details of the chemical bonding. Since it is not relevant for the physics, we will absorb it in β from now on. Lastly, t is the hopping amplitude and a the lattice spacing. Notice that the Hamiltonian (7.10) has the same form as that of flat graphene in a magnetic field B that is generated by a vector potential $\boldsymbol{A}$. In that light, we can compute the pseudo-magnetic field corresponding to the vector potential of the deformations, which is given by

$$ev_F B_{ps} = \frac{\partial A_y}{\partial x} - \frac{\partial A_x}{\partial y}, \tag{7.13}$$

where the factor ev_F is to ensure that B_{ps} has indeed units of magnetic field.

One important property of these pseudo-magnetic fields is that they preserve time-reversal symmetry, unlike real magnetic fields. What this means, is that the two valleys

in graphene feel an opposite magnetic field. Remember that the valleys represent point in momentum space, so they are in fact related to each other by time reversal (since $K' = -K$). By explicit calculation, it can be shown that

$$B_K = -B_{K'},$$

which always follows intuitively, because deformations alone can not break time-reversal symmetry [59].

Chapter 8

Hydrodynamical theory applied to graphene

The aim of this section is to create a model that can be used to apply the theory from Chapter 7 to the experimental set-up described in Chapter 2. Although the experiment is the starting point of our derivations, we will not use the model to draw detailed conclusions about the experiment, since the model just serves as a rough way to bridge the gap between the theory of Chapter 7 and the experiment at hand.

Furthermore, we should remark that in the experiment, it was shown that not the mechanical deformations themselves produce the pseudo-magnetic field, but actually the chemical strain that is imposed by the hydrogen atoms on the bonds between the carbon atoms. However, this model serves in the first place as an example of a system where the pseudo-magnetic fields are generated by mechanical strain. In practice, this means that the deformations should be sufficiently large to be able to produce pseudo-magnetic fields.

In this model, we attempt to calculate the harmonic moments t_k, which appear as the coefficients in the expansion of the potential $V(z)$, as shown in Eqs. (7.1) and (7.2). By using the first order approximation for $V(z)$, given by Eq. (7.3), it is then in principle possible to perform Monte Carlo simulations, in order to model the fingering process of the electron droplets.

First of all, the question that arises is how to model the deformations in the graphene sample, which emerge due to the hydrogen atoms and the SiC substrate, such that we can calculate the pseudo-magnetic fields associated to these corrugations. In Section 8.1, we will present a toy model that provides a way to capture the effect of one hydrogen atom. Subsequently, we will derive the corresponding pseudo-magnetic field in Section 8.2 and, as an example, calculate the harmonic moments for different values of the parameters in the system.

8.1 The model

Let us start by considering the effect of the substrate. In Chapter 2, we explained that not every silicon atom in the SiC substrate binds to a carbon atom from the graphene buffer layer. Some of them are left freely 'dangling'. The actual sheet of graphene on top of the buffer layer still feels the effect of these unsaturated bonds. This causes the graphene to form little bumps above them. Since these dangling bonds emerge in a triangular lattice with a lattice spacing of 2 nm, the bumps will form the same triangular lattice. In

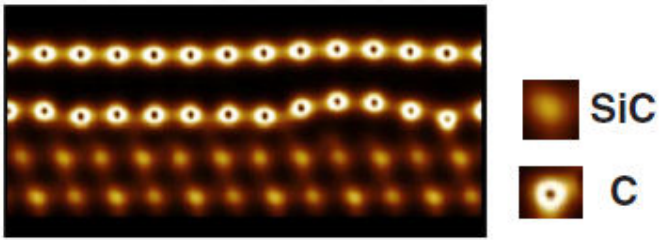

Figure 8.1: Cross-section of buffer layer and actual graphene layer on top of the SiC substrate. The bumping effect is the largest in the buffer layer, but it is still visible in the top graphene layer. Figure from Ref. [8].

Fig. 8.1, we can see that the height of the bump is small in comparison with the spacing between the bumps. This ensures that the deformation is smooth enough to generate a pseudo-magnetic field without distorting the structure of the graphene too much. The hydrogen that is then applied on top of the corrugated graphene layer occupies preferably the sites in one sublattice op top of the bumps. They will increase the bump and allow for the formation of the pseudo-magnetic fields. We choose to model these bumps by the following height profile:

$$h(x,y) = \frac{h_0}{3} + \frac{2h_0}{9}\left[\cos\left(\frac{2\pi x}{\sqrt{3}\lambda} - \frac{2\pi y}{\lambda}\right) + \cos\left(\frac{2\pi x}{\sqrt{3}\lambda} + \frac{2\pi y}{\lambda}\right) + \cos\left(\frac{4\pi x}{\sqrt{3}\lambda}\right)\right], \quad (8.1)$$

where h_0 is the height of a bump and λ is the lattice spacing. This function is a simple example of a triangular lattice of bumps, which have the shape of cosines. Note that there are more ways to model the bumps and we just chose a simple one.

The set-up of the theoretical model in Section 7.1 is based on an electronic droplet in a constant magnetic field, which serves to quantize the kinetic energy, together with a nonuniform magnetic field outside the droplet. Hence, we have to determine which parts of the pseudo-magnetic fields will fulfill which role. In this model, we assume that the pseudo-magnetic field that is generated by the periodic deformations due to the substrate and the hydrogen atoms acts as the uniform field. Although the field is not exactly uniform, the bumps are uniformly distributed over the graphene layer. Hence, it can indeed play the role of the uniform part of the magnetic field $B_0(z)$. For the nonuniform part, we consider one extra hydrogen atom that sits on top of one of the bumps, next to an already present hydrogen atom, thereby increasing the bump even further. The pseudo-magnetic field of that configuration, minus the overall field, will serve as the nonuniform part $\delta B(z) = B(z) - B_0(z)$. Since the effect of the hydrogen atom is to increase the height of one of the bumps, we model it by a Gaussian function with a standard deviation equal to $\lambda/4$, in order to keep the radius of the bump roughly the same. The height profile of the Gaussian bump is thus

$$h_H(x,y) = \frac{h_0}{H} e^{-8\left[(x-x_0)^2+(y-y_0)^2\right]/\lambda^2}, \quad (8.2)$$

where (x_0, y_0) is the position of the hydrogen atom and $H = h_0/H_0$ is defined as the ratio between the height h_0 of the deformations due to the substrate and the height H_0 of the additional Gaussian bump.

For the electronic droplet, we assume that there is a circular droplet of radius R_D. In the experiment, the droplet could be confined by either impurities or by the deformations

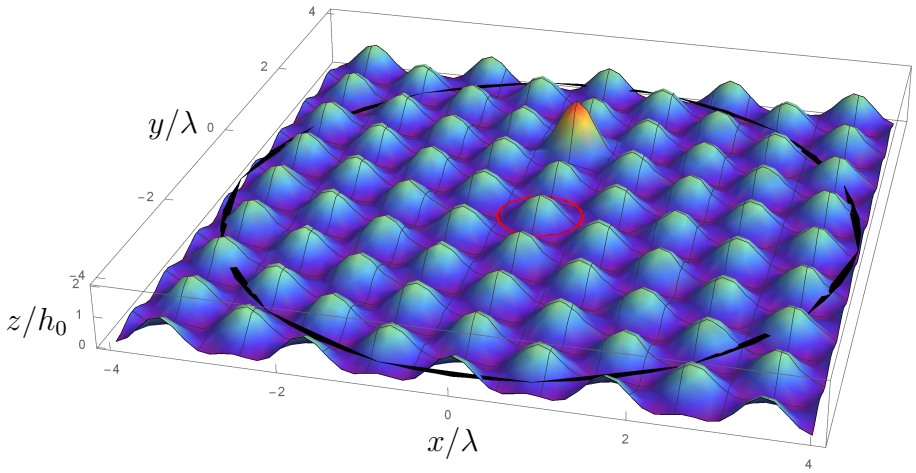

Figure 8.2: Bumps in a triangular lattice, due to the substrate. The peak is the deformation due to one hydrogen atom that is locate there. The red and black circles indicate respectively the position of the droplet and the radius R_0, as defined in Section 7.1.

of the graphene layer, but for now we just consider it to be there and do not worry about the origin of its formation. In Fig. 8.2, the configuration of this toy model is shown for $H = 1$.

8.2 Results

We will proceed to derive the pseudo-magnetic field that arises due to the deformations formed by the silicon dangling bonds, using the height profile given in Eq. (8.1). Notice that, in the absence of in-plane deformations, the deformation tensor (7.9) is of the form

$$u_{\alpha\beta} = \frac{1}{2}\frac{\partial h}{\partial x_\alpha}\frac{\partial h}{\partial x_\beta}. \tag{8.3}$$

Using Eqs. (7.11) and (7.12), together with Eq. (7.13), we can readily derive the pseudo-magnetic field due to the dangling bonds (see Appendix E.1 for derivation),

$$B^0_{ps} = \frac{\beta t}{e v_F}\frac{256\pi^3 h_0^2}{243\lambda^3}\left[\cos\left(\frac{2\pi y}{\lambda}\right) - \cos\left(\frac{2\sqrt{3}\pi x}{\lambda}\right)\right]\sin\left(\frac{2\pi y}{\lambda}\right). \tag{8.4}$$

In Fig. 8.3, this pseudo-magnetic field is shown, together with the deformed graphene sheet. The peaks of the pseudo-magnetic field are also arranged in a triangular lattice, with a lattice constant $1/\sqrt{3}$. We can see that the magnetic field has its peaks (either positive of negative) on the lowest points in the graphene sheet, while the magnetic field is zero in the middle of the bumps.

Next, we calculate the nonuniform part of the magnetic field $\delta B(x, y) = B(x, y) - B_0(x, y)$ (see Appendix E.1). For a hydrogen atom in the origin, it is given approximately by

$$\delta B(x, y) = 4096\frac{t\beta}{e v_F}\frac{H_0^2}{\lambda^6}(y^3 - 3x^2 y)\, e^{-16(x^2+y^2)/\lambda^2}.$$

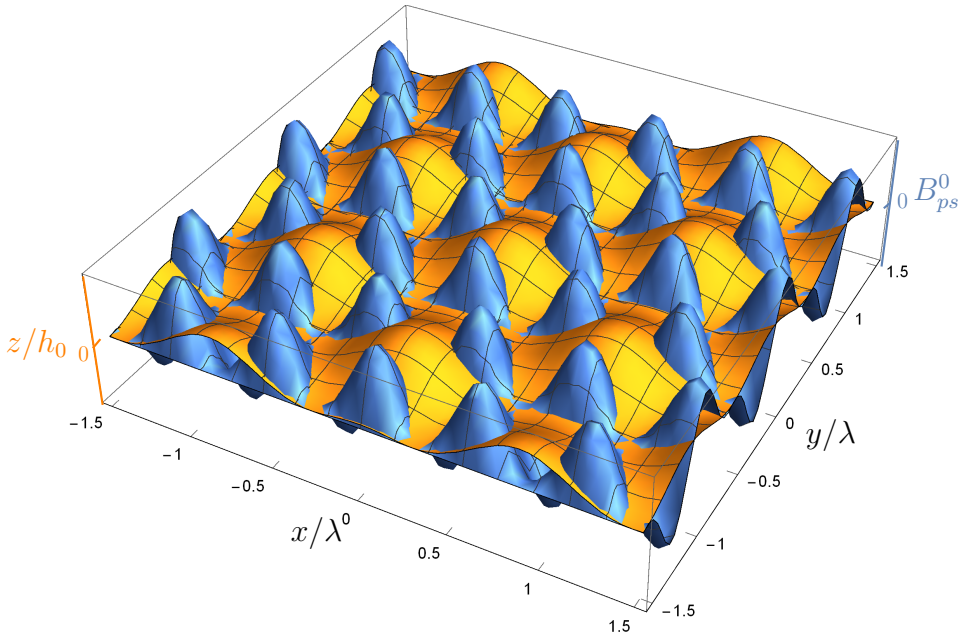

Figure 8.3: Pseudo-magnetic field in units of $\beta t h_0^2/ev_F\lambda^3$ (blue) of a period deformation of the graphene layer (orange) consisting of a triangular lattice of bumps.

This is exactly the pseudo-magnetic field that arises due to the single Gaussian bump defined in Eq. (8.2), which turns out to be the dominant term. In Fig. 8.4, this nonuniform pseudo-magnetic field is shown. It has a three-fold rotational symmetry. At first sight, this may seem counter intuitive, because it is the magnetic field that arises due to a configuration that possesses a full rotational symmetry. However, we must keep in mind that the formulas that are used to calculate these magnetic fields are specific for graphene. They originated from deformations of the hexagonal lattice. At a lattice point, graphene has precisely this three-fold rotational symmetry. Hence, even if we consider the system in the continuum limit, where typical distances are much larger than the lattice spacing of graphene, the system still 'remembers' the underlying lattice and its symmetry properties.

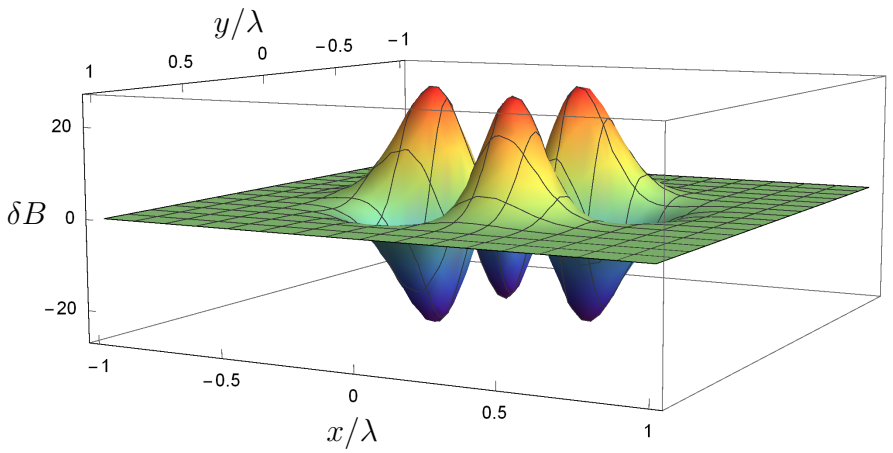

Figure 8.4: Pseudo-magnetic field that arises due to a Gaussian bump in the graphene layer. δB is given in units of $\beta t H_0^2/ev_F\lambda^3$.

Using this pseudo-magnetic field, we want to compute the harmonic moments t_k, as defined in Eq. (7.2),

$$\begin{aligned} t_k &= \frac{1}{\pi k}\int_{D_{ex}} \delta B(z) z^{-k} d^2 z \\ &= -\frac{2i}{\pi k}\int_{D_{ex}} dxdy\, \delta B(x,y)(x+iy)^{-k} \\ \\ &= -\frac{2i}{\pi k}\,\lambda^{2-k}\int_{D_{ex}} dx'dy'\, \delta B(x',y')(x'+iy')^{-k}, \end{aligned}$$

where $x' = x/\lambda$ and $y' = y/\lambda$. If we consider the model, as described in the previous section, there are two parameters that we can tune: the radius of the droplet R_D and the distance from the droplet to the hydrogen atom, which we will call L. They enter in the integral for t_k as

$$t_k = -\frac{2i}{\pi k}\,\lambda^{2-k}\int_0^{2\pi}\int_{R_D}^{\infty} d\phi dr\, \delta B(r\cos(\phi-\phi_0)-L, r\sin(\phi-\phi_0)) r^{1-k} e^{-ik\phi},$$

where we wrote the integral in polar coordinates and places δB at a distance L from the origin under an arbitrary angle ϕ_0. In principle, the r-integral has to run to infinity, but in practice it is sufficient to integrate up to some cut-off radius R_C, which has to be larger than $L+\lambda$ in any case, since the field quickly falls off to zero away from δB, which has a typical radius of approximately λ.

We calculate t_k in units of $h_0^2\beta t/ev_F\lambda$, such that the integral only depends on the parameter H, which we will set equal to 2. Furthermore, the factor λ^{-k} that appears in front of t_k will be absorbed in z_k when we substitute t_k in the potential $V(z) = \mathrm{Re}\sum_{k\geq 1} t_k z^k/2$, such that z is dimensionless and all t_k have the same units. To compute t_k, we use the full nonuniform magnetic field given in Eq. (E.1).

First, we will set the distance from the hydrogen atom to the center of the droplet to $L = 3$ (we will represent space in units of λ in the rest of this chapter) and fix $\phi_0 = 0$. In Table 8.1 the values for t_k are shown for various k and R_D. Note that R_D can maximally go up to about 2, otherwise the magnetic field starts to overlap with the droplet, which violates the assumption that δB is outside the droplet. We repeat the same calculations for $L = 2$. From both results, we can conclude that for large separations t_k does not change if you bring the hydrogen atom closer to the droplet. Only when the electronic droplet is almost touching the magnetic field, i.e., $L - R_D \approx 1$, it starts to 'feel' its effect. We can also say that if R_D is decreased below $L-1$, the corresponding t_k does not change.

On the other hand, if we fix R_D and vary L, there is not such a clear point where the effect of the magnetic field kicks in, as can be seen from Table 8.2. Rather, t_k changes smoothly as L is increased. It converges slowly to zero, unlike in the previous case where t_k converged to some finite value upon decreasing R_D.

Lastly, we investigate the dependence of t_k of the angle ϕ_0 at which the hydrogen atom is places. We fix $L = 2$ and $R_D = 1$, such that we consider the point where the droplet really start to feel the effect of the magnetic field. In Table 8.3, the values for t_k are shown for various values of ϕ_0 between 0 and π. For $\pi < \phi_0 \leq 2\pi$, the results are the same as for $2\pi - \phi_0$. We notice that they take values in the range $[-t_k^0, t_k^0]$ for some t_k^0.

Notice that we can not draw any

$L = 3$

t_k \ R_D	1.5	1.6	1.7	1.8	1.9	2	2.1	2.2
t_1	2.55	2.55	2.55	2.55	2.56	2.59	2.76	3.44
t_2	1.70	1.70	1.70	1.70	1.70	1.72	1.80	2.11
t_3	0.942	0.942	0.942	0.943	0.944	0.953	0.992	1.14

$L = 2$

t_k \ R_D	1.5	1.6	1.7	1.8	1.9	2	2.1	2.2
t_1	12.9	12.9	12.9	12.9	12.9	13.0	13.6	15.6
t_2	12.8	12.8	12.8	12.8	12.8	13.0	13.5	15.2
t_3	10.5	10.5	10.5	10.5	10.6	10.7	11.2	12.7

Table 8.1: t_k (in units of $10^{-3}\, h_0^2 \beta t / e v_F \lambda$) for various values of R_D. t_k starts to change round $R_D \approx 2$ for $L = 3$ and $R_D \approx 1$ for $L = 2$.

$R_D = 1$

t_k \ L	1.8	1.9	2	2.1	2.2	2.5	2.75	3
t_1	19.4	14.6	11.7	10.1	9.65	5.72	4.18	2.55
t_2	25.6	17.4	13.0	10.1	7.97	4.22	2.62	1.70
t_3	23.8	15.2	10.7	7.92	6.00	2.80	1.59	0.942

$R_D = 2$

t_k \ L	2.8	2.9	3	3.1	3.2	3.5	3.75	4
t_1	4.42	3.15	2.59	2.24	1.97	1.38	1.04	0.807
t_2	2.95	2.13	1.72	1.44	1.23	0.786	0.557	0.403
t_3	1.71	1.22	0.953	0.776	0.640	0.374	0.247	0.168

Table 8.2: t_k (in units of $10^{-3}\, h_0^2 \beta t / e v_F \lambda$) for various values of L.

$R_D = 1$, $L = 2$

t_k \ ϕ_0	0	$\pi/8$	$\pi/4$	$3\pi/8$	$\pi/2$	$5\pi/8$	$3\pi/4$	$7\pi/8$	π
t_1	2.55	2.35	1.80	0.975	0	-0.975	-1.80	2-.35	-2.55
t_2	1.70	1.20	0	-1.20	-1.70	-1.20	0	1.20	1.70
t_3	0.942	0.360	-0.666	-0.871	0	0.871	0.666	-0.496	-1.30

Table 8.3: t_k (in units of $10^{-3}\, h_0^2 \beta t / e v_F \lambda$) for various values of ϕ_0.

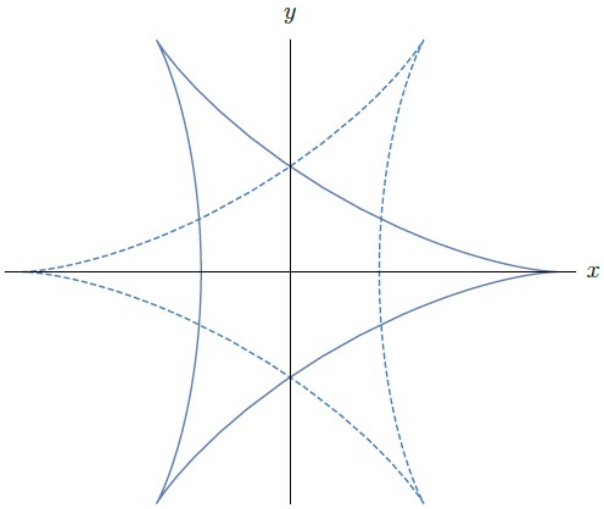

Figure 8.5: The superposition of the K (solid line) and K' (dashed line) electrons leads to a doubling in the number of cusps.

8.2.1 The formations of cusps in pseudo-magnetic fields

Until thus far, we have not taken into account the special feature of pseudo-magnetic fields that they preserve time-reversal symmetry, unlike real magnetic fields, as discussed in Section 7.3. When we do, we notice that the electrons in the, say, K valley experience a non-uniform magnetic field δB, while the electrons in the K' valley then feel a field $-\delta B$. Through Eqs. (7.1) and (7.2), which relate $\delta B(z)$ to the potential $V(z)$, we can deduce that the potential that influence the electrons is also opposite in the two valleys. Since we cannot distinguish between the K and K' electrons, the superposition of the two potentials will give rise to an increase in the number of cusps, as shown in Fig. 8.5.

8.3 Discussion of the results

We have shown a way to set up a model that can apply the theory described in Chapter 7 to the experiment from Chapter 2. We have used the pseudo-magnetic fields that arise in graphene due to deformations as the driving mechanism for the fingering of an electronic droplet. By identifying the field generated by deformations due to the substrate as the uniform part and the effect of one additional hydrogen atom on top op the graphene layer as the non-uniform part, we were able to calculate some of the harmonic moments t_k for various values of the radius of the droplet R_D and the distance between the droplet and the hydrogen atom L. It turns out that if we fix L and compute t_k for increasing values of R_D, it is only from the moment that $R_D \approx L - 1$ (in units of λ) that the values start to change, which happens independent of k. Hence, the droplet 'feels' the magnetic field when they are (almost) touching, since the radius in which the magnetic field is essentially non-zero is approximately 1. When you increase the radius of the droplet even further, the magnitude of t_k becomes even larger, but it is a bit tricky to do this, since it violates the assumption that the magnetic field is outside of the droplet.

Similarly, if we fix R_D an vary L, t_k starts to change when the magnetic field is in the vicinity of the boundary of the droplet. Hence, it is the parameter $L - R_D$ which determines when the magnitude of t_k starts to grow, which should be around $L - R_D \approx 1$. Furthermore, the larger L is, the smaller the magnitude of t_k. This makes sense because

of the r^{1-k} term in the integral, which becomes smaller for increasing r.

We must remark that we cannot draw any conclusions from the actual values of t_k. We can merely compare them for different values of the parameters. For example, consider the angle ϕ_0, which determines the position (L, ϕ_0) of the hydrogen atom. We certainly expect it to influence the shape of the droplet (and hence t_k), since we can intuitively suspect that the droplet will form a finger towards the magnetic field (or away from it if the magnetic field is of opposite sign). When we calculate t_k for $L - R_D = 1$ for various ϕ_0, we note that it varies all the way from $-t_k^0$ to $+t_k^0$ for some value t_k^0. From this observation, we cannot derive the dependence of the shape of the droplet on ϕ_0, since we do not posses a direct way to 'translate' t_k into the shape of the boundary $z(w)$.

This model serves as an example for the application of the theory to practical situations. Calculating the harmonic moments of the nonuniform part of the magnetic field is crucial here, since they completely determine the potential which drives the growth process of the electronic droplet. Knowledge of this potential enables one to reveal the evolution of the shape of the droplet, using Monte Carlo simulations.

We have not performed this simulations here and it might be interesting to investigate in further research if one can reproduce the patterns that were observed in the experiment using Monte Carlo simulations.

Furthermore, it would be very instructive to obtain a more profound understanding of the analytic solutions for the shape of the boundary. It is only for the simply form of the potential in Eq. (7.3) that it was possible to derive the exact form of the boundary, which was already a highly non-trivial procedure.

Chapter 9

Conclusion and outlook

Motivated by hydrogenated graphene experiments, in which fractal-like structures were observed in the electron density, we have investigated two different kinds of interactions in graphene under the influence of a perpendicular magnetic field. We have used existing models for conventional two-dimensional electron systems like GaAs, and adjusted them to fit the special characteristics of graphene.

To begin with, we have considered the interactions between electrons in a single partially filled Landau level. In this regime, the kinetic energy is quenched, making the Coulomb interaction between the electrons the dominant contribution to the Hamiltonian. We have calculated and compared the energies of the Wigner crystal phase, the bubble phases and the electron-liquid phase. As a start, we have shown that the Landau level structure of the Hamiltonian can be collected in the form factor, which determines the form of the effective interaction. The multi-component character of the wave function in graphene causes this form factor to change with respect to the familiar one for GaAs. The form factor in graphene for the n-th Landau level combines the form factors of GaAs in the n-th and $(n-1)$-th Landau level. This blending of two adjacent Landau levels also influences the electronic phase diagram. We have seen that, for the lowest Landau level, graphene behaves the same as GaAs, which exhibits no charge density waves but only electron-liquid phases. Thereby, the fractional quantum Hall effect can be observed at filling factors $\bar{\nu} = 1/(2s+1)$, for integer s. For the $n = 1$ Landau level in graphene, there are still some characteristics of the lowest Landau level present, as a consequence of the Landau level blending. We have shown that the liquid phases are lower in energy than the solid phases for all filling fractions. However, impurities in the sample can lower the solid energies, especially at low filling. Indeed, if the impurity potential is sufficiently strong, the $\bar{\nu} = 1/7$ and $\bar{\nu} = 1/9$ fractional quantum Hall states can be washed out. The plateau in the resistivity will then be broadened because the electrons are collectively pinned by the impurities and do not contribute to macroscopic electronic transport. In higher Landau levels, the electron-solid phases become more pronounced. In the $n = 2$ Landau level, for instance, the $\bar{\nu} = 1/3$ fractional quantum Hall state is dominated by the 2-electron bubble phase, even without impurities. As the Landau level increases, more bubble phases emerge and there could also be phase coexistence between different electron-solid phases.

Furthermore, we have compared our analytic calculations for the electron-liquid energies to numerical ones and we have found that they are in excellent agreement, which confirms the validity of our presumption that all of graphene's special features can be captured in the form factor.

Until thus far, no signs of these types of electron-solid phases have been observed in experiments. For the lowest Landau levels this is not surprising, since we expect the liquid phase to dominate. It would be interesting to see whether future experiments in higher Landau levels can verify our theoretical predictions of the various electron phases in graphene, just like they did for GaAs.

In the second part of the thesis, we have analyzed the interaction between electrons and an inhomogeneous magnetic field. Here, the electrons are in the completely filled lowest Landau level, such that we can ignore electron-electron interactions. The motivation for this study was an existing theory that describes fingering of electronic droplets in the integer quantum Hall regime, due to a nonuniform magnetic field outside the droplet. Since this could provide an explanation for the fractal-like structures in the hydrogenated graphene experiment. We have set up a model that uses pseudo-magnetic fields in graphene to quantize the energy levels and to provide a nonuniform magnetic field. We have seen that these pseudo-magnetic fields can arise due to deformations in the graphene sheet, which can be generated by the underlying substrate or the hydrogen atoms on top of the graphene layer. Subsequently, we have calculated the coefficients of the potential that drives the fingering growth process and compared them for different values of various parameters. With this, we have laid the groundwork for further investigations that can be done using Monte Carlo simulations.

This model was inspired by the experiment but is actually much more general than that and it could be used to describe the behavior of electrons in deformed graphene, under the influence of a nonuniform magnetic field. For future research, it would be very insightful to do Monte Carlo simulations to see whether it is possible to reproduce the structures that were observed in the experiment. More experimental research on the origin of the deformations would also be very instructive, since there are indications that this pseudo-magnetic field is caused by chemical interactions instead of mechanical strain.

Appendix A

Appendices to Chapter 4

A.1 Hamiltonian in first and second quantization

Here, we will show that the second-quantized Hamiltonian (4.13) in real space is equivalent to the effective first-quantized Hamiltonian (4.12) in momentum space. First of all, we write down the former,

$$H = t \sum_{\langle i,j\rangle,\sigma} (a^\dagger_{\sigma,i} b_{\sigma,j} + \text{h.c.}) + t' \sum_{\langle\langle i,j\rangle\rangle,\sigma} (a^\dagger_{\sigma,i} a_{\sigma,j} + b^\dagger_{\sigma,i} b_{\sigma,j} + \text{h.c.}),$$

and do a Fourier transform to momentum space, that is

$$a_{\sigma,i} = \frac{1}{\sqrt{N}} \sum_{\boldsymbol{k}} a_{\sigma,\boldsymbol{k}}\, e^{i\boldsymbol{k}\cdot\boldsymbol{r}_i},$$

where $\boldsymbol{r}_i$ is the position of site i. The Fourier transform of the operators on the B-sublattice are defined similarly. For notational convenience we will drop the spin index σ from now on. For the nearest-neighbor hopping term we then obtain

$$\begin{aligned}\sum_{\langle i,j\rangle} a^\dagger_i b_j &= \frac{1}{N} \sum_{\boldsymbol{k},\boldsymbol{k}'} \sum_{\langle i,j\rangle} a^\dagger_{\boldsymbol{k}} b_{\boldsymbol{k}'} e^{-i\boldsymbol{k}\cdot\boldsymbol{r}_i} e^{i\boldsymbol{k}'\cdot\boldsymbol{r}_j} \\ &= \frac{1}{N} \sum_{\boldsymbol{k},\boldsymbol{k}'} \sum_{\langle i,j\rangle} a^\dagger_{\boldsymbol{k}} b_{\boldsymbol{k}'} e^{-i\boldsymbol{k}\cdot(\boldsymbol{r}_i - \boldsymbol{r}_j)} e^{i\boldsymbol{r}_j\cdot(\boldsymbol{k}'-\boldsymbol{k})}.\end{aligned}$$

Since we sum only over nearest neighbors, $\boldsymbol{r}_i - \boldsymbol{r}_j = \boldsymbol{\delta}_m$, where $\boldsymbol{\delta}_m$ is one of the nearest-neighbor vectors, as defined in Eq. (4.2). Hence, the sum over nearest neighbors reduces to

$$\begin{aligned}\sum_{\langle i,j\rangle} a^\dagger_i b_j &= \frac{1}{N} \sum_{\boldsymbol{k},\boldsymbol{k}'} \sum_{j=1}^{N} a^\dagger_{\boldsymbol{k}} b_{\boldsymbol{k}'} e^{i\boldsymbol{r}_j\cdot(\boldsymbol{k}'-\boldsymbol{k})} \sum_{m=1}^{3} e^{i\boldsymbol{k}\cdot\boldsymbol{\delta}_m} \\ &= \sum_{\boldsymbol{k},\boldsymbol{k}'} \sum_{j=1}^{N} a^\dagger_{\boldsymbol{k}} b_{\boldsymbol{k}'} e^{i\boldsymbol{r}_j\cdot(\boldsymbol{k}'-\boldsymbol{k})} \sum_{m=1}^{3} e^{i\boldsymbol{k}\cdot\boldsymbol{\delta}_m}.\end{aligned}$$

In the continuum limit, the sum over j of the exponent becomes and integral and yields a delta-function $\delta(\boldsymbol{k} - \boldsymbol{k}')$. Then the sum over $\boldsymbol{k}'$ also becomes an integral which can then

be evaluated. This leads to

$$\sum_{\langle i,j\rangle} a_i^\dagger b_j = \sum_{\boldsymbol{k}} a_{\boldsymbol{k}}^\dagger b_{\boldsymbol{k}} \sum_{m=1}^{3} e^{i\boldsymbol{k}\cdot\boldsymbol{\delta}_m}.$$

The next-nearest neighbor term can be calculated in the same manner, except that now $\boldsymbol{r}_i - \boldsymbol{r}_j$ is one the of the six vectors connecting the next-nearest neighbors of a particular site, which are $\pm\boldsymbol{a}_1$, $\pm\boldsymbol{a}_2$ and $\pm\boldsymbol{a}_3 \equiv \pm(\boldsymbol{a}_1 + \boldsymbol{a}_2)$, where $\boldsymbol{a}_{1,2}$ are the primitive lattice vectors of the sublattices, as defined in Eq. (4.1). The next-nearest neighbor term of the Hamiltonian in momentum space thus becomes

$$\begin{aligned}\sum_{\langle i,j\rangle} a_i^\dagger a_j &= \frac{1}{2}\sum_{\boldsymbol{k}} a_{\boldsymbol{k}}^\dagger a_{\boldsymbol{k}} \sum_{m=1}^{3} (e^{-i\boldsymbol{k}\cdot\boldsymbol{a}_m} + e^{i\boldsymbol{k}\cdot\boldsymbol{a}_m}) \\ &= \sum_{\boldsymbol{k}} a_{\boldsymbol{k}}^\dagger a_{\boldsymbol{k}} \sum_{m=1}^{3} \cos(\boldsymbol{k}\cdot\boldsymbol{a}_m),\end{aligned}$$

where the factor $1/2$ in the first line comes from the fact that we only sum over one sublattice, which contains half of all the sites. The rest of the terms in the Hamiltonian can be transformed similarly and we obtain for the Hamiltonian in momentum space

$$H = t\sum_{\boldsymbol{k}}\sum_{m=1}^{3}(a_{\boldsymbol{k}}^\dagger b_{\boldsymbol{k}} e^{i\boldsymbol{k}\cdot\boldsymbol{\delta}_m} + a_{\boldsymbol{k}} b_{\boldsymbol{k}}^\dagger e^{-i\boldsymbol{k}\cdot\boldsymbol{\delta}_m}) + 2t'\sum_{\boldsymbol{k}}\sum_{m=1}^{3}(a_{\boldsymbol{k}}^\dagger a_{\boldsymbol{k}} + b_{\boldsymbol{k}}^\dagger b_{\boldsymbol{k}})\cos(\boldsymbol{k}\cdot\boldsymbol{a}_m).$$

Subsequently, write it in matrix form as follows,

$$H = \begin{pmatrix} a_{\boldsymbol{k}}^\dagger & b_{\boldsymbol{k}}^\dagger \end{pmatrix} H_{\boldsymbol{k}}^{eff} \begin{pmatrix} a_{\boldsymbol{k}} \\ b_{\boldsymbol{k}} \end{pmatrix},$$

such that we can read off the matrix elements. They read

$$H_{\boldsymbol{k}}^{eff} = \sum_{m=1}^{3} \begin{pmatrix} 2t'\cos(\boldsymbol{k}\cdot\boldsymbol{a}_m) & te^{i\boldsymbol{k}\cdot\boldsymbol{\delta}_m} \\ te^{-i\boldsymbol{k}\cdot\boldsymbol{\delta}_m} & 2t'\cos(\boldsymbol{k}\cdot\boldsymbol{a}_m). \end{pmatrix}$$

Using the notation introduced in Eq. (4.9),

$$\gamma_{\boldsymbol{k}} = \left(1 + e^{-i\boldsymbol{k}\cdot\boldsymbol{a}_2} + e^{-i\boldsymbol{k}\cdot\boldsymbol{a}_3}\right),$$

we can write

$$\sum_{m=1}^{3} e^{i\boldsymbol{k}\cdot\boldsymbol{\delta}_m} = e^{i\boldsymbol{k}\cdot\boldsymbol{\delta}_3}\gamma_{\boldsymbol{k}}^*,$$

which can be seen by using the relations between $\boldsymbol{\delta}_i$ and $\boldsymbol{a}_j$. The exponent on the right-hand side is just a phase shift that is irrelevant for the physics of the system, which can be seen from the dispersion relation (4.11), which only depends on the modulus of $\gamma_{\boldsymbol{k}}$. Furthermore, for the diagonal terms in the Hamiltonian we can write

$$\sum_{m=1}^{3} 2\cos(\boldsymbol{k}\cdot\boldsymbol{a}_m) = |\gamma_{\boldsymbol{k}}|^2 - 3,$$

which can be derived straightforwardly by writing out the expressions on both sides. Notice that the term -3 will contribute to the Hamiltonian a constant term $-3t'$ which we omit, just like we did originally for the effective Hamiltonian (4.12) because a constant shift in the Hamiltonian is not relevant for the physics of the system. We then obtain

$$\mathcal{H}_{\boldsymbol{k}}^{eff} = \begin{pmatrix} t'|\gamma_{\boldsymbol{k}}|^2 & t\gamma_{\boldsymbol{k}}^* \\ t\gamma_{\boldsymbol{k}} & t'|\gamma_{\boldsymbol{k}}|^2 \end{pmatrix},$$

which is exactly the effective first-quantized Hamiltonian in momentum space for which we wanted to show the equivalence to the second-quantized Hamiltonian in real space we started out with.

Appendix B

Appendices to Chapter 5

B.1 Derivation of the form factor

In Eq. (5.3), we have written the density operator in reciprocal space in terms of the projected density operator and a form factor, the latter given explicitly in Eq. (5.5). Here, we will demonstrate how we can separate the density operator in those two contributions and derive the explicit expression of the form factor. We start off by writing out the density in reciprocal space and inserting the expression for $\psi_n(\boldsymbol{r})$ given by Eq. (5.2),

$$\begin{aligned}\rho_n(\boldsymbol{q}) &= \int d^2r\, \psi_n^\dagger(\boldsymbol{r})\psi_n(\boldsymbol{r})e^{i\boldsymbol{q}\cdot\boldsymbol{r}} \\ &= \sum_{y_0,y_0'} \int d^2r\, \langle n, y_0|\boldsymbol{r}\rangle e^{i\boldsymbol{q}\cdot\boldsymbol{r}} \langle \boldsymbol{r}|n, y_0'\rangle c_{n,y_0}^\dagger c_{n,y_0'}.\end{aligned}$$

We remark that $|\boldsymbol{r}\rangle$ is an eigenstate of the position operator $\hat{\boldsymbol{r}}$ with eigenvalue $\boldsymbol{r}$. Hence, we can write

$$e^{i\boldsymbol{q}\cdot\hat{\boldsymbol{r}}} = \int d^2r\, e^{i\boldsymbol{q}\cdot\hat{\boldsymbol{r}}}|\boldsymbol{r}\rangle\langle\boldsymbol{r}| = \int d^2r\, e^{i\boldsymbol{q}\cdot\boldsymbol{r}}|\boldsymbol{r}\rangle\langle\boldsymbol{r}|,$$

where we inserted a complete set of states in the first step and applied the position operator in the second step. With this, we can write

$$\rho_n(\boldsymbol{q}) = \sum_{y_0,y_0'} \langle n, y_0|e^{i\boldsymbol{q}\cdot\hat{\boldsymbol{r}}}|n, y_0'\rangle c_{n,y_0}^\dagger c_{n,y_0'}.$$

We can write the position operator as a sum of the guiding center position operator and the cyclotron variable, as shown in Section 3.2, such that

$$e^{i\boldsymbol{q}\cdot\hat{\boldsymbol{r}}} = e^{i\boldsymbol{q}\cdot\hat{\boldsymbol{R}}+i\boldsymbol{q}\cdot\hat{\boldsymbol{\eta}}} = e^{i\boldsymbol{q}\cdot\hat{\boldsymbol{R}}}e^{i\boldsymbol{q}\cdot\hat{\boldsymbol{\eta}}}e^{-[\hat{\boldsymbol{R}},\hat{\boldsymbol{\eta}}]/2} = e^{i\boldsymbol{q}\cdot\hat{\boldsymbol{R}}}e^{i\boldsymbol{q}\cdot\hat{\boldsymbol{\eta}}},$$

where we used the Baker-Hausdorff formula and the fact that $\hat{\boldsymbol{R}}$ and $\hat{\boldsymbol{\eta}}$ commute. Furthermore, since $\hat{\boldsymbol{\eta}}$ only acts on $|n\rangle$ and $\hat{\boldsymbol{R}}$ only on $|y_0\rangle$, as we have elaborated on in Section 3.3.1, we can split the two terms, such that

$$\begin{aligned}\rho_n(\boldsymbol{q}) &= \langle n|e^{i\boldsymbol{q}\cdot\hat{\boldsymbol{\eta}}}|n\rangle \sum_{y_0,y_0'} \langle y_0|e^{i\boldsymbol{q}\cdot\hat{\boldsymbol{R}}}|y_0'\rangle c_{n,y_0}^\dagger c_{n,y_0'} \\ &= F_n(\boldsymbol{q})\bar{\rho}(\boldsymbol{q}).\end{aligned}$$

The form factor can now be computed by evaluating the matrix elements of $e^{i\boldsymbol{q}\cdot\hat{\boldsymbol{\eta}}}$. Firstly, we use Eqs. (3.9) and (3.13) to express $\hat{\boldsymbol{\eta}}$ in terms of the ladder operators,

$$\hat{\eta}_x = \frac{il_B}{\sqrt{2}}\left(a^\dagger - a\right), \qquad \hat{\eta}_y = \frac{l_B}{\sqrt{2}}\left(a^\dagger + a\right).$$

Using this, we can write the form factor as

$$\begin{aligned} F_n(\boldsymbol{q}) &\equiv \langle n|e^{i\boldsymbol{q}\cdot\hat{\boldsymbol{\eta}}}|n\rangle \\ &= \langle n|e^{-q_x l_B(a^\dagger - a)/\sqrt{2} + iq_y l_B(a^\dagger + a)/\sqrt{2}}|n\rangle \\ &= \langle n|e^{-l_B q a^\dagger/\sqrt{2} + l_B q^* a/\sqrt{2}}|n\rangle \\ &= \langle n|e^{-l_B q a^\dagger/\sqrt{2}}\, e^{l_B q^* a/\sqrt{2}}|n\rangle\, e^{l_B^2 q^2/4[a^\dagger, a]}, \end{aligned}$$

where we defined $q \equiv q_x - iq_y$ and hence $q^* = q_x + iq_y$ in the second equality and we used the Baker-Hausdorff formula in the third equality. Inserting a complete set of states, we obtain

$$F_n(\boldsymbol{q}) = \sum_{j=0}^{\infty} \langle n|e^{-l_B q a^\dagger/\sqrt{2}}|j\rangle\langle j|e^{l_B q^* a/\sqrt{2}}|n\rangle\, e^{-l_B^2 q^2/4}.$$

Using the definition of the creation operator $a^\dagger|j\rangle = \sqrt{j+1}|j+1\rangle$, we can derive that

$$\begin{aligned} \langle n|e^{-l_B q a^\dagger/\sqrt{2}}|j\rangle &= \sum_{m=0}^{\infty} \sqrt{\frac{(j+m)!}{j!}} \frac{1}{m!} \left(\frac{-l_B q}{\sqrt{2}}\right)^m \langle n|j+m\rangle \\ &= \sum_{m=0}^{\infty} \sqrt{\frac{(j+m)!}{j!}} \frac{1}{m!} \left(\frac{-l_B q}{\sqrt{2}}\right)^m \delta_{n,j+m} \\ &= \begin{cases} \sqrt{\frac{n!}{j!}} \frac{1}{(n-j)!} \left(\frac{-l_B q}{\sqrt{2}}\right)^{n-j} & \text{if } j \le n, \\ 0 & \text{if } j > n. \end{cases} \end{aligned} \tag{B.1}$$

The second term appearing in $\langle n|e^{i\boldsymbol{q}\cdot\hat{\boldsymbol{\eta}}}|n\rangle$ is basically the Hermitian conjugate of the first one, thus we can combine both terms to obtain

$$\begin{aligned} F_n(\boldsymbol{q}) &= \sum_{j=0}^{n} \frac{n!}{j!} \frac{1}{(n-j)!^2} (-1)^{n-j} \left(\frac{l_B^2 q^2}{2}\right)^{n-j} e^{-l_B^2 q^2/4} \\ &= \sum_{j=0}^{n} \binom{n}{j} \frac{(-1)^j}{j!} \left(\frac{l_B^2 q^2}{2}\right)^j e^{-l_B^2 q^2/4} \\ &= L_n\left(\frac{q^2 l_B^2}{2}\right) e^{-l_B^2 q^2/4}, \end{aligned}$$

where $L_n(x)$ is the n-th Laguerre polynomial.

B.2 Density operator commutation relations

We will derive the commutation relation in Eq. (5.8). For convenience, we will use the expression for $\bar{\rho}(\boldsymbol{q})$ in the Landau gauge, since it can be shown that this commutation

relation is in fact gauge invariant [43]. We start by writing out the definition of the projected density operators given in Eq. (5.4),

$$[\bar{\rho}(\boldsymbol{q}), \bar{\rho}(\boldsymbol{k})] = \sum_{y_0, y_0'} e^{-iq_y y_0} e^{-ik_y y_0'} [c^\dagger_{n,y_0+\gamma_q} c_{n,y_0-\gamma_q}, c^\dagger_{n,y_0'+\gamma_k} c_{n,y_0'-\gamma_k}], \tag{B.2}$$

where we defined $\gamma_q \equiv q_x l_B^2/2$. Using the following identity, which holds for fermionic operators,

$$[AB, CD] = -AC\{B, D\} + A\{B, C\}D - C\{A, D\}B + \{A, C\}DB,$$

we can write out the commutator on the right hand side in Eq. (B.2),

$$\begin{aligned}
&[c^\dagger_{n,y_0+\gamma_q} c_{n,y_0-\gamma_q}, c^\dagger_{n,y_0'+\gamma_k} c_{n,y_0'-\gamma_k}] = -c^\dagger_{n,y_0+\gamma_q} c^\dagger_{n,y_0'+\gamma_k} \{c_{n,y_0-\gamma_q}, c_{n,y_0'-\gamma_k}\} \\
&+ c^\dagger_{n,y_0+\gamma_q} \{c_{n,y_0-\gamma_q}, c^\dagger_{n,y_0'+\gamma_k}\} c_{n,y_0'-\gamma_k} - c^\dagger_{n,y_0'+\gamma_k} \{c^\dagger_{n,y_0+\gamma_q}, c_{n,y_0'-\gamma_k}\} c_{n,y_0-\gamma_q} \\
&+ \{c^\dagger_{n,y_0+\gamma_q}, c^\dagger_{n,y_0'+\gamma_k}\} c_{n,y_0'-\gamma_k} c_{n,y_0-\gamma_q} \\
&= c^\dagger_{n,y_0+\gamma_q} c_{n,y_0'-\gamma_k} \delta_{y_0-\gamma_q, y_0'+\gamma_k} - c^\dagger_{n,y_0'+\gamma_k} c_{n,y_0-\gamma_q} \delta_{y_0+\gamma_q, y_0'-\gamma_k}.
\end{aligned}$$

We substitute this back into Eq. (B.2) and perform the sum over y_0',

$$\begin{aligned}
[\bar{\rho}(\boldsymbol{q}), \bar{\rho}(\boldsymbol{k})] &= \sum_{y_0} e^{-iq_y y_0} e^{-ik_y(y_0-\gamma_q-\gamma_k)} c^\dagger_{n,y_0+\gamma_q} c_{n,y_0-\gamma_q-2\gamma_k} \\
&\quad + e^{-iq_y y_0} e^{-ik_y(y_0+\gamma_q+\gamma_k)} c^\dagger_{n,y_0+\gamma_q+2\gamma_k} c_{n,y_0-\gamma_q} \\
&= e^{-iy_0(q_y+k_y)} \left(e^{ik_y(\gamma_q+\gamma_k)} c^\dagger_{n,y_0+\gamma_q} c_{n,y_0-\gamma_q-2\gamma_k} + e^{-ik_y(\gamma_q+\gamma_k)} c^\dagger_{n,y_0+\gamma_q+2\gamma_k} c_{n,y_0-\gamma_q} \right)
\end{aligned}$$

To rewrite this into a more convenient form, we shift $y_0 \to y_0 + \gamma_k$ in the first term in the sum and $y_0 \to y_0 - \gamma_k$ in the second. The expression above then reduces to,

$$\begin{aligned}
[\bar{\rho}(\boldsymbol{q}), \bar{\rho}(\boldsymbol{k})] &= \sum_{y_0} e^{-iy_0(q_y+k_y)} \left(e^{-i\gamma_k q_y} e^{ik_y\gamma_q} + e^{i\gamma_k q_y} e^{-ik_y\gamma_q} \right) c^\dagger_{n,y_0+\gamma_q+\gamma_k} c_{n,y_0-\gamma_q-\gamma_k} \\
&= \sum_{y_0} e^{-iy_0(q_y+k_y)} \left(e^{i(q_x k_y - q_y k_x) l_B^2/2} + e^{-i(q_x k_y - q_y k_x) l_B^2/2} \right) c^\dagger_{n,y_0+\gamma_q+\gamma_k} c_{n,y_0-\gamma_q-\gamma_k} \\
&= \sum_{y_0} e^{-iy_0(q_y+k_y)} \, 2i \sin\left[\frac{(\boldsymbol{q} \times \boldsymbol{k})_z l_B^2}{2} \right] c^\dagger_{n,y_0+\gamma_q+\gamma_k} c_{n,y_0-\gamma_q-\gamma_k} \\
&= 2i \sin\left(\frac{(\boldsymbol{q} \times \boldsymbol{k})_z l_B^2}{2} \right) \bar{\rho}(\boldsymbol{q} + \boldsymbol{k}).
\end{aligned}$$

This is the expression we wanted to derive.

B.3 Exchange potential in $n = 1$ Landau level

We calculate the Fock exchange potential in Eq. (5.9) for $n = 1$, by using the definition of the effective potential $v_n(p)$ given by Eq. (5.7) in terms of a Laguerre polynomial,

$$\begin{aligned} u_1^F(q) &= \frac{1}{N_B}\sum_{\boldsymbol{p}} v_1(p) e^{-i(p_y q_x - q_y p_x)l_B^2} \\ &= \frac{1}{N_B}\sum_{\boldsymbol{p}} \frac{2\pi e^2}{\epsilon p} L_1(p^2 l_B^2/2)^2 e^{-p^2 l_B^2/2} e^{-i(p_y q_x - q_y p_x)l_B^2} \\ &= \frac{1}{N_B}\sum_{\boldsymbol{p}} \frac{2\pi e^2}{\epsilon p} (1 - p^2 l_B^2/2)^2 e^{-p^2 l_B^2/2} e^{-i(p_y q_x - q_y p_x)l_B^2}. \end{aligned}$$

Notice that we can write $N_B = n_B A$ and furthermore, we substitute the sum by an integral using $\sum_{\boldsymbol{p}} \to A \int d^2p/(2\pi)^2$. In the second line, we write the integrand in polar coordinates $\boldsymbol{p} = p(\cos\phi_p, \sin\phi_p)$ and $\boldsymbol{q} = q(\cos\phi_q, \sin\phi_q)$. This leads to,

$$\begin{aligned} u_1^F(q) &= \frac{2\pi e^2}{\epsilon n_B}\frac{1}{(2\pi)^2}\int d^2p\, \frac{1}{p}(1 - p^2 l_B^2/2)^2 e^{-p^2 l_B^2/2} e^{-i(p_y q_x - q_y p_x)l_B^2} \\ &= \frac{e^2}{\epsilon n_B}\frac{1}{2\pi}\int dp\,(1 - p^2 l_B^2/2)^2 e^{-p^2 l_B^2/2} \int d\phi_p\, e^{-ipq(\sin\phi_p\cos\phi_q - \cos\phi_p \sin\phi_q)l_B^2} \\ &= \frac{e^2}{\epsilon n_B}\frac{1}{2\pi}\int dp\,(1 - p^2 l_B^2 + p^4 l_B^4/4) e^{-p^2 l_B^2/2}\, 2\pi J_0(pq l_B^2) \\ &= \frac{e^2}{\epsilon n_B}\left\{ \frac{e^{-q^2 l_B^2/4}}{l_B}\sqrt{\frac{\pi}{2}} I_0\left(\frac{q^2 l_B^2}{4}\right) - \frac{e^{-q^2 l_B^2/4}}{2l_B}\sqrt{\frac{\pi}{2}}\left[(2 - q^2 l_B^2) I_0\left(\frac{q^2 l_B^2}{4}\right) + q^2 l_B^2 I_1\left(\frac{q^2 l_B^2}{4}\right)\right]\right. \\ &\left. + \frac{e^{-q^2 l_B^2/4} l_B}{8}\sqrt{\frac{\pi}{2}}\left[(6/l_B^2 - 6q^2 + l_B^2 q^4) I_0\left(\frac{q^2 l_B^2}{4}\right) + (4q^2 - l_B^2 q^4) I_1\left(\frac{q^2 l_B^2}{4}\right)\right]\right\} \\ &= \frac{e^2}{\epsilon n_B}\frac{e^{-q^2 l_B^2/4}}{8l_B}\sqrt{\frac{\pi}{2}}\left\{(6 - 2q^2 l_B^2 + q^4 l_B^4) I_0\left(\frac{q^2 l_B^2}{4}\right) - q^4 l_B^4 I_1\left(\frac{q^2 l_B^2}{4}\right)\right\}. \end{aligned}$$

This is the desired form of Eq. (5.11) that we wanted to derive.

B.4 A useful identity

In this section, we will derive the identity used in Section 5.2,

$$\sum_j e^{-i\boldsymbol{q}\cdot\boldsymbol{R}_j} = \frac{(2\pi)^2}{A_{pc}}\sum_l \delta(\boldsymbol{q} - \boldsymbol{G}_l), \tag{B.3}$$

where $\boldsymbol{R}_j$ are the lattice vectors, $\boldsymbol{G}_l$ the reciprocal lattice vectors and A_{pc} the area of the primitive cell in real space. To prove this identity, we start by remarking that the real space and reciprocal space lattice vectors relate to each other according to the identity

$$\boldsymbol{R}_j \cdot \boldsymbol{G}_l = 2\pi\delta_{j,l}.$$

Hence, we can write $1 = e^{i\boldsymbol{R}_j\cdot\boldsymbol{G}_l}$ for all j and l and thus also

$$1 = \sum_l e^{i\boldsymbol{R}_j\cdot\boldsymbol{G}_l}/\#l, \tag{B.4}$$

where $\#l$ is the total number of reciprocal lattice vectors that is summed over by l. We can express this number as the ratio A_{BZ}/A_{rec}, where A_{BZ} is the area of the Brillouin zone and A_{rec} the area of reciprocal space corresponding to the area in real space, which is $A_{rec} = (2\pi)^2/A$. Hence,

$$\#l = \frac{A_{BZ}}{A_{rec}} = \frac{(2\pi)^2/A}{(2\pi)^2/A_{pc}} = \frac{A_{pc}}{A}.$$

If we now multiply the left hand side of Eq. (B.3) by 1, using the expression from Eq. (B.4), we obtain

$$\begin{aligned}
\sum_j e^{-i\boldsymbol{q}\cdot\boldsymbol{R}_j} &= \sum_j e^{-i\boldsymbol{q}\cdot\boldsymbol{R}_j} \frac{A}{A_{pc}} \sum_l e^{i\boldsymbol{R}_j\cdot\boldsymbol{G}_l} \\
&= \frac{1}{A_{pc}} \sum_l A \sum_j e^{-i\boldsymbol{R}_j\cdot(\boldsymbol{q}-\boldsymbol{G}_l)} \\
&= \frac{1}{A_{pc}} \sum_l (2\pi)^2 \int d^2r\, e^{-i\boldsymbol{R}_j\cdot(\boldsymbol{q}-\boldsymbol{G}_l)} \\
&= \frac{(2\pi)^2}{A_{pc}} \sum_l \delta(\boldsymbol{q}-\boldsymbol{G}_l),
\end{aligned}$$

which is precisely the right-hand side of Eq. (B.3). This proves this identity.

B.5 Plotting the cohesive energy of the bubble phase

In Section 5.2, we derived the cohesive energy of an M-electron-bubble phase in the n-th Landau level. It reads

$$E^B_{coh}(n; M, \bar{\nu}) = \frac{\bar{\nu}}{2\pi l_B^2 M} \sum_l u_n^{HF}(\boldsymbol{G}_l) \frac{J_1(\sqrt{2M} l_B |\boldsymbol{G}_l|)^2}{l_B^2 |\boldsymbol{G}_l|^2}. \tag{B.5}$$

In order to compare the energies of the different bubble phase and the liquid phase, we want to plot this energy in units of $e^2/\epsilon l_B$. We do this explicitly for the $n = 1$ Landau level, the other Landau levels are then a straightforward generalization. First of all, we write out the expression for the Hartree-Fock energy in the $n = 1$ Landau level, using Eqs. (5.7) and (5.11),

$$\begin{aligned}
u_1^{HF}(q) &= v_1(q) - u_1^F(q) \\
&= \frac{2\pi e^2}{\epsilon q} [L_1(q^2 l_B^2/2)]^2 e^{-q^2 l_B^2/2} \\
&\quad - \sqrt{\frac{\pi}{2}} \frac{e^2}{\epsilon l_B} \frac{e^{-q^2 l_B^2/4}}{8 n_B} \left[(6 - 2q^2 l_B^2 + q^4 l_B^4) I_0\left(\frac{q^2 l_B^2}{4}\right) - q^4 l_B^4 I_1\left(\frac{q^2 l_B^2}{4}\right) \right] \\
&= \frac{e^2}{\epsilon l_B} \frac{2\pi l_B^2}{q l_B} [L_1(q^2 l_B^2/2)]^2 e^{-q^2 l_B^2/2} \\
&\quad - \frac{e^2}{\epsilon l_B} \sqrt{\frac{\pi}{2}} \frac{\pi l_B^2}{4} e^{-q^2 l_B^2/4} \left[(6 - 2q^2 l_B^2 + q^4 l_B^4) I_0\left(\frac{q^2 l_B^2}{4}\right) - q^4 l_B^4 I_1\left(\frac{q^2 l_B^2}{4}\right) \right],
\end{aligned}$$

where we used $n_B = 1/2\pi l_B^2$. If we write the energy in units of $e^2/\epsilon l_B$ and the momentum in units of $1/l_B$ we can write it more compactly in a dimensionless way as

$$\frac{u_1^{HF}(q/l_B)}{(e^2/\epsilon l_B)} = \frac{2\pi l_B^2}{q}[L_1(q^2/2)]^2 e^{-q^2/2} - \sqrt{\frac{\pi}{2}}\frac{\pi l_B^2}{4} e^{-q^2/4}\left[(6-2q^2+q^4)I_0\left(\frac{q^2}{4}\right) - q^4 I_1\left(\frac{q^2}{4}\right)\right].$$

From this we can see that we keep a factor of l_B which cancels exactly the factor of $1/l_B^2$ that appears in the cohesive energy in Eq. (B.5).

Furthermore, to actually evaluate the cohesive energy, we have to sum over the reciprocal lattice vectors. The reciprocal lattice of a triangular lattice is again a triangular lattice with primitive lattice vectors

$$\boldsymbol{b}_1 = \frac{2\pi}{\Lambda_B}\left(\hat{x} - \frac{1}{\sqrt{3}}\hat{y}\right), \qquad \boldsymbol{b}_2 = \frac{4\pi}{\sqrt{3}\Lambda_B}\hat{y}.$$

Using the relation between the real space lattice spacing and the partial filling factor obtained in Eq. (5.13), we can write

$$\Lambda_B = l_B\left(\frac{4\pi M}{\sqrt{3}\bar{\nu}}\right)^{1/2}.$$

The reciprocal lattice vectors are linear combinations of the primitive vectors, such that

$$\begin{aligned}\boldsymbol{G}_l &= \alpha_l \boldsymbol{b}_1 + \beta_l \boldsymbol{b}_2 \\ &= \alpha_l \frac{2\pi}{l_B}\left(\frac{\sqrt{3}\bar{\nu}}{4\pi M}\right)^{1/2}\left(\hat{x} - \frac{1}{\sqrt{3}}\hat{y}\right) + \beta_l \frac{4\pi}{\sqrt{3}l_B}\left(\frac{\sqrt{3}\bar{\nu}}{4\pi M}\right)^{1/2}\hat{y} \\ &= \frac{1}{l_B}\left(\frac{\sqrt{3}\pi\bar{\nu}}{M}\right)^{1/2}\left[\alpha_l\hat{x} + \frac{1}{\sqrt{3}}(2\beta_l - \alpha_l)\hat{y}\right].\end{aligned}$$

From this we can conclude that the terms $l_B|\boldsymbol{G}_l|$ appearing in the cohesive energy are independent of l_B. Notice that the reciprocal lattice vectors do depend on the partial filling factor. Hence, the only parameters that appear in the cohesive energy are indeed the number of electrons per bubble M and the Landau level index n.

Since we sum only over the length of the reciprocal lattice vectors, we can make use of the sixfold symmetry of the triangular lattice to simplify the computation. We can then divide the triangular lattice intro rings of lattice points around a given point (see Fig. B.1). In the k-th ring, there are six sets of k lattice vectors that have the same length. These are given by

$$|\boldsymbol{G}_l^k| = |k\boldsymbol{b}_1 + l\boldsymbol{b}_2|,$$

for $l = 0, \cdots, k-1$. The cohesive energy can then be written as

$$E_{coh}^B(n; M, \bar{\nu}) = \frac{3\bar{\nu}}{\pi l_B^2 M}\sum_k \sum_{l=0}^{k-1} u_n^{HF}(\boldsymbol{G}_l^k)\frac{J_1(\sqrt{2M}l_B|\boldsymbol{G}_l^k|)^2}{l_B^2|\boldsymbol{G}_l^k|^2}. \tag{B.6}$$

The advantage of writing it in this form is that the sum over l is now finite and since k runs over sets of vectors with increasing lengths, we can use a natural cut-off for k such that we sum over those vectors with the smallest length, which have the largest contribution to the energy, since all the terms appearing in the energy become small if $|\boldsymbol{G}_l^k|$ becomes large.

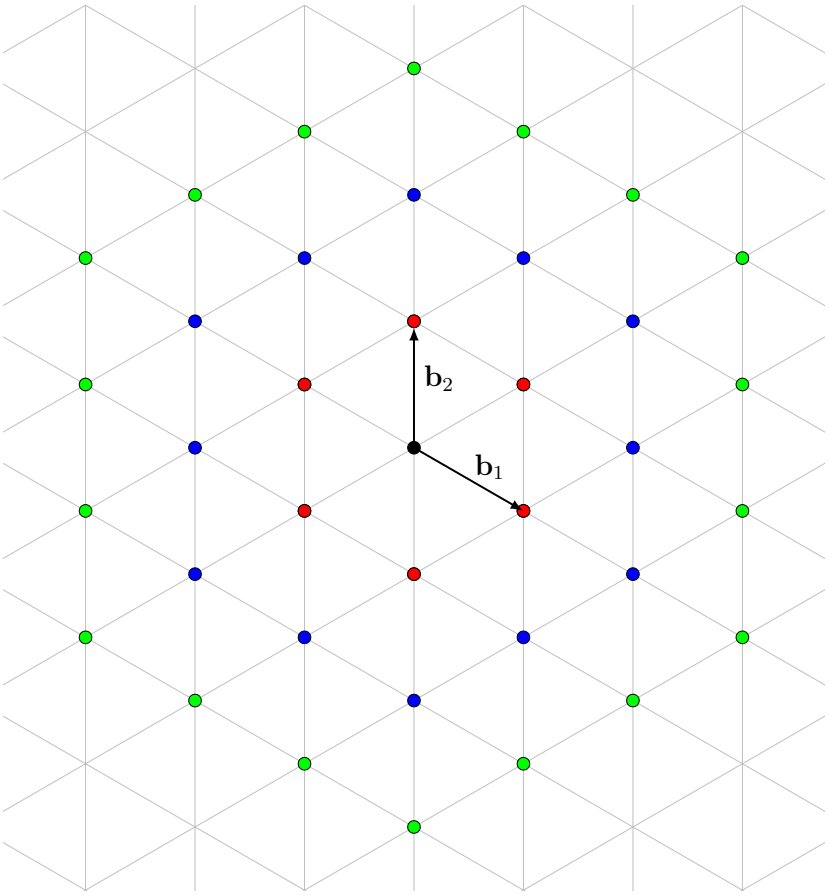

Figure B.1: Reciprocal triangular lattice of the bubble crystal. The colors indicate the separate groups of lattice points that we sum over in Eq. (B.6).

Appendix C

Appendices to Chapter 6

C.1 Derivation of the form factor in graphene

In this appendix, we derive the form factors of graphene for general valley indices and subsequently show that the terms with different indices in the interaction are not contributing to the leading order in perturbation theory.

First of all, we write out the density operator in reciprocal space

$$\begin{aligned}
\rho^n(\boldsymbol{q}) &= \sum_\alpha \rho^n_\alpha(\boldsymbol{q}) \\
&= \sum_\alpha \sum_{\sigma,\sigma'} \int d^2r\, \psi^\dagger_{\alpha,\sigma}(\boldsymbol{r})\psi_{\alpha,\sigma'}(\boldsymbol{r})e^{i\boldsymbol{q}\cdot\boldsymbol{r}} \\
&= \sum_\alpha \int d^2r\, \left[\psi^\dagger_{\alpha,+}(\boldsymbol{r})\psi_{\alpha,+}(\boldsymbol{r}) + \psi^\dagger_{\alpha,-}(\boldsymbol{r})\psi_{\alpha,-}(\boldsymbol{r}) + \psi^\dagger_{\alpha,+}(\boldsymbol{r})\psi_{\alpha,-}(\boldsymbol{r}) + \psi^\dagger_{\alpha,-}(\boldsymbol{r})\psi_{\alpha,+}(\boldsymbol{r})\right] e^{i\boldsymbol{q}\cdot\boldsymbol{r}} \\
&= \sum_\alpha \int d^2r\, \Big[\chi^\dagger_{\alpha,+}(\boldsymbol{r})\chi_{\alpha,+}(\boldsymbol{r}) + \chi^\dagger_{\alpha,-}(\boldsymbol{r})\chi_{\alpha,-}(\boldsymbol{r}) \\
&\qquad\qquad + \chi^\dagger_{\alpha,+}(\boldsymbol{r})\chi_{\alpha,-}(\boldsymbol{r})e^{-2i\boldsymbol{K}\cdot\boldsymbol{r}} + \chi^\dagger_{\alpha,-}(\boldsymbol{r})\chi_{\alpha,+}(\boldsymbol{r})e^{2i\boldsymbol{K}\cdot\boldsymbol{r}}\Big] e^{i\boldsymbol{q}\cdot\boldsymbol{r}},
\end{aligned}$$

where we inserted the wave function given in Eq. (6.1). Using the definition of $\chi_\sigma(\boldsymbol{r})$ given by Eq. (6.2), where α denotes its components, we obtain

$$\begin{aligned}
\rho^n(\boldsymbol{q}) = \frac{1}{2}\sum_{m,m'} \int d^2r\, e^{i\boldsymbol{q}\cdot\boldsymbol{r}} \Big\{ & (c^\dagger_{n,m,+}c_{n,m',+} + c^\dagger_{n,m,-}c_{n,m',-}) \\
& \times \left[(1+\delta_{n,0})\langle|n|,m|\boldsymbol{r}\rangle\langle\boldsymbol{r}||n|,m'\rangle + \mathrm{sgn}^2(n)\langle|n|-1,m|\boldsymbol{r}\rangle\langle\boldsymbol{r}||n|-1,m'\rangle\right] \\
& + \mathrm{sgn}(n) i\sqrt{1+\delta_{n,0}}(e^{-2i\boldsymbol{K}\cdot\boldsymbol{r}}c^\dagger_{n,m,+}c_{n,m',-} + e^{2i\boldsymbol{K}\cdot\boldsymbol{r}}c^\dagger_{n,m,-}c_{n,m',+}) \\
& \times \left[\langle|n|-1,m|\boldsymbol{r}\rangle\langle\boldsymbol{r}||n|,m'\rangle - \langle|n|,m|\boldsymbol{r}\rangle\langle\boldsymbol{r}||n|-1,m'\rangle\right] \Big\}.
\end{aligned}$$

Using a similar derivation as was done for the normal form factor in Appendix B.1, we can write

$$\int d^2r\, e^{i\boldsymbol{q}\cdot\boldsymbol{r}}|\boldsymbol{r}\rangle\langle\boldsymbol{r}| = e^{i\boldsymbol{q}\cdot\hat{\boldsymbol{r}}},$$

where $\hat{\boldsymbol{r}} = \hat{\boldsymbol{R}} + \hat{\boldsymbol{\eta}}$ is the position operator, which can be expressed in terms of the guiding-center position operator $\boldsymbol{R}$ and the cyclotron variable $\boldsymbol{\eta}$. As shown for the non-relativistic case, the wave function then decompose into

$$\langle n, m|e^{i\boldsymbol{q}\cdot\hat{\boldsymbol{r}}}|n', m'\rangle = \langle n|e^{i\boldsymbol{q}\cdot\hat{\boldsymbol{\eta}}}|n'\rangle\langle m|e^{i\boldsymbol{q}\cdot\hat{\boldsymbol{R}}}|m'\rangle.$$

Substituting these results into the density operator, we obtain

$$\begin{aligned}
\rho^n(\boldsymbol{q}) = \frac{1}{2}\sum_{m,m'}\Big\{ & (c^\dagger_{n,m,+}c_{n,m',+} + c^\dagger_{n,m,-}c_{n,m',-})\langle m|e^{i\boldsymbol{q}\cdot\hat{\boldsymbol{R}}}|m'\rangle \\
& \times \left[(1+\delta_{n,0})\langle |n||e^{i\boldsymbol{q}\cdot\hat{\boldsymbol{\eta}}}||n|\rangle + \mathrm{sgn}^2(n)\langle |n|-1|e^{i\boldsymbol{q}\cdot\hat{\boldsymbol{\eta}}}||n|-1\rangle\right] \\
& + \mathrm{sgn}(n)i\sqrt{1+\delta_{n,0}}\,\langle m|e^{i(\boldsymbol{q}-2\boldsymbol{K})\cdot\hat{\boldsymbol{R}}}|m'\rangle c^\dagger_{n,m,+}c_{n,m',-} \\
& \times \left[\langle |n|-1|e^{i(\boldsymbol{q}-2\boldsymbol{K})\cdot\hat{\boldsymbol{\eta}}}||n|\rangle - \langle |n||e^{i(\boldsymbol{q}-2\boldsymbol{K})\cdot\hat{\boldsymbol{\eta}}}||n|-1\rangle\right] \\
& + \mathrm{sgn}(n)i\sqrt{1+\delta_{n,0}}\,\langle m|e^{i(\boldsymbol{q}+2\boldsymbol{K})\cdot\hat{\boldsymbol{R}}}|m'\rangle c^\dagger_{n,m,-}c_{n,m',+} \\
& \times \left[\langle |n|-1|e^{i(\boldsymbol{q}+2\boldsymbol{K})\cdot\hat{\boldsymbol{\eta}}}||n|\rangle - \langle |n||e^{i(\boldsymbol{q}+2\boldsymbol{K})\cdot\hat{\boldsymbol{\eta}}}||n|-1\rangle\right]\Big\}.
\end{aligned}$$

For $n \neq 0$ we can write this as

$$\begin{aligned}
\rho^n(\boldsymbol{q}) &= \frac{1}{2}\sum_{m,m'}\sum_{\sigma} c^\dagger_{n,m,\sigma}c_{n,m',\sigma}\langle m|e^{i\boldsymbol{q}\cdot\hat{\boldsymbol{R}}}|m'\rangle\left[\langle |n||e^{i\boldsymbol{q}\cdot\hat{\boldsymbol{\eta}}}||n|\rangle + \langle |n|-1|e^{i\boldsymbol{q}\cdot\hat{\boldsymbol{\eta}}}||n|-1\rangle\right] \\
&+ \frac{1}{2}\sum_{m,m'}\sum_{\sigma}\langle m|e^{i(\boldsymbol{q}-2\sigma\boldsymbol{K})\cdot\hat{\boldsymbol{R}}}|m'\rangle c^\dagger_{n,m,\sigma}c_{n,m',-\sigma} \\
&\times \mathrm{sgn}(n)i\left[\langle |n|-1|e^{i(\boldsymbol{q}-2\sigma\boldsymbol{K})\cdot\hat{\boldsymbol{\eta}}}||n|\rangle - \langle |n||e^{i(\boldsymbol{q}-2\sigma\boldsymbol{K})\cdot\hat{\boldsymbol{\eta}}}||n|-1\rangle\right] \qquad \text{(C.1)} \\
&= \sum_{\sigma}\left[\bar{\rho}^{\sigma,\sigma}(\boldsymbol{q})F^{\sigma,\sigma}_n(\boldsymbol{q}) + \bar{\rho}^{\sigma,-\sigma}(\boldsymbol{q})F^{\sigma,-\sigma}_n(\boldsymbol{q})\right].
\end{aligned}$$

We can shift $\boldsymbol{q} \to \boldsymbol{q} + \sigma\boldsymbol{K}$ in the second term and subsequently we can read off the expressions for $\bar{\rho}^{\sigma,\sigma'}(\boldsymbol{q})$ and $F^{\sigma,\sigma'}_n(\boldsymbol{q})$. Firstly,

$$\begin{aligned}
\bar{\rho}^{\sigma,\sigma}(\boldsymbol{q}) &= \sum_{m,m'}\langle m|e^{i\boldsymbol{q}\cdot\hat{\boldsymbol{R}}}|m'\rangle c^\dagger_{n,m,\sigma}c_{n,m',\sigma}, \\
\bar{\rho}^{\sigma,-\sigma}(\boldsymbol{q}) &= \sum_{m,m'}\langle m|e^{i(\boldsymbol{q}-\sigma\boldsymbol{K})\cdot\hat{\boldsymbol{R}}}|m'\rangle c^\dagger_{n,m,\sigma}c_{n,m',-\sigma},
\end{aligned}$$

which we can generalize to

$$\bar{\rho}^{\sigma,\sigma'}(\boldsymbol{q}) = \sum_{m,m'}\langle m|e^{i(\boldsymbol{q}+(\sigma'-\sigma)\boldsymbol{K})\cdot\hat{\boldsymbol{R}}}|m'\rangle c^\dagger_{n,m,\sigma}c_{n,m',\sigma'}.$$

For the form factors we obtain

$$\begin{aligned}
F^{\sigma,\sigma}_n(\boldsymbol{q}) &= \frac{1}{2}\left[\langle |n||e^{i\boldsymbol{q}\cdot\hat{\boldsymbol{\eta}}}||n|\rangle + \langle |n|-1|e^{i\boldsymbol{q}\cdot\hat{\boldsymbol{\eta}}}||n|-1\rangle\right] \\
&= \frac{1}{2}\left[L_{|n|}\left(\frac{q^2l_B^2}{2}\right) + L_{|n|-1}\left(\frac{q^2l_B^2}{2}\right)\right]e^{q^2l_B^2/4},
\end{aligned}$$

where we used the expressions for the non-relativistic form factors we derived in Appendix B.1, since the two terms correspond to $F_{|n|}(q)$ and $F_{|n|-1}(q)$. For the form factor with different valley indices we get

$$F_n^{\sigma,-\sigma}(\boldsymbol{q}) = \frac{1}{2}\lambda i \left[\langle |n|-1|e^{i(\boldsymbol{q}-\sigma\boldsymbol{K})\cdot\hat{\boldsymbol{\eta}}}||n|\rangle - \langle |n||e^{i(\boldsymbol{q}-\sigma\boldsymbol{K})\cdot\hat{\boldsymbol{\eta}}}||n|-1\rangle\right],$$

where $\lambda = \mathrm{sgn}(n)$. The two terms in between the square brackets can be computed using the expressions for these matrix elements derived in Eq. (B.1). We obtain

$$\begin{aligned} F_n^{\sigma,-\sigma}(\boldsymbol{q}) &= \lambda i \frac{-l_B[q+q^*+\sigma(K+K^*)]}{2\sqrt{2|n|}} e^{-l_B^2|\boldsymbol{q}+\sigma\boldsymbol{K}|^2/4} \\ &\quad \times \sum_{j=0}^{n-1}\left[\frac{n!}{j!(n-j)!}\frac{1}{(n-1-j)!}(-1)^{n-1-j}\left(\frac{l_B^2|\boldsymbol{q}+\sigma\boldsymbol{K}|^2}{2}\right)^{n-1-j}\right] \\ &= \frac{\lambda i l_B[q+q^*-\sigma(K+K^*)]}{2\sqrt{2|n|}} L^1_{|n|-1}\left(\frac{l_B^2|\boldsymbol{q}-\sigma\boldsymbol{K}|^2}{2}\right) e^{-l_B^2|\boldsymbol{q}-\sigma\boldsymbol{K}|^2/4}, \end{aligned}$$

where we used the definition of the generalized Laguerre polynomial in the second line.

Next, we investigate the form factors in the lowest Landau level. We write the density operator in Eq. (C.1) for $n=0$,

$$\begin{aligned} \rho^0(\boldsymbol{q}) &= \sum_{m,m'}\sum_{\sigma} c^\dagger_{n,m,\sigma}c_{n,m',\sigma}\langle m|e^{i\boldsymbol{q}\cdot\hat{\boldsymbol{R}}}|m'\rangle\langle |n||e^{i\boldsymbol{q}\cdot\hat{\boldsymbol{\eta}}}||n|\rangle \\ &= \sum_{\sigma} F_0(q)\bar{\rho}_{\sigma,\sigma}(\boldsymbol{q}), \end{aligned}$$

where $F_0(q)$ is the non-relativistic form factor in the lowest Landau level. Hence, for $n=0$ the form factor for graphene and for normal 2DEGs coincide.

Having derived the interaction in Eq. (6.3) in terms of the form factors, we show here that the leading order term in a/l_B is of the form

$$v_n(\boldsymbol{q}) = v(q)[F_n^{\sigma,\sigma}(\boldsymbol{q})]^2.$$

We can distinguish three cases that will not contribute to the leading order term. Notice that $|\boldsymbol{K}| \sim 1/a$. First of all, terms of the form $v(q)F_n^{\sigma,\sigma}(\mp\boldsymbol{q})F_n^{\sigma',-\sigma'}(\pm\boldsymbol{q})$ or $v(q)F_n^{\sigma,-\sigma}(-\boldsymbol{q})F_n^{\sigma,-\sigma}(\boldsymbol{q})$ (the latter are so-called umklapp-scattering terms) have as leading order term $e^{-l_B^2|\boldsymbol{q}-\sigma\boldsymbol{K}|^2} \sim e^{-(l_B/a)^2}$, hence they are exponentially small in a/l_B. Furthermore, backscattering terms of the form

$$\begin{aligned} v(q)F_n^{\sigma,-\sigma}(-\boldsymbol{q})F_n^{-\sigma,\sigma}(\boldsymbol{q}) &\sim f(\boldsymbol{q}-\sigma\boldsymbol{K})e^{-l_B^2|\boldsymbol{q}-\sigma\boldsymbol{K}|^2} l_B/q \\ &\sim f(\boldsymbol{q})e^{-l_B^2|\boldsymbol{q}|^2}/|\boldsymbol{q}+\sigma\boldsymbol{K}| \\ &\sim a/l_B, \end{aligned}$$

where $f(\boldsymbol{q})$ is some general function. In the second step we have shifted $\boldsymbol{q} \to \boldsymbol{q}+\sigma\boldsymbol{K}$. Hence, the leading order terms in a/l_B are of the form $v(q)[F_n^{\sigma,\sigma}(\boldsymbol{q})]^2$.

C.2 Exchange potentials in graphene

Here we write down the explicit forms of the exchange potentials by evaluating the equation (6.8). We calculate the expressions for Landau levels $n = 1, 2, 3$, using the same derivation as was done in Appendix B.3 for the normal case. The potential is in units of $e^2/\epsilon l_B$ and q is in units of $1/l_B$,

$$u_1^F(q) = \frac{e^{-q^2/4}}{32n_B}\sqrt{\frac{\pi}{2}}\left[(22+2q^2+q^4)I_0\left(\frac{q^2}{4}\right) - (4q^2+q^4)I_1\left(\frac{q^2}{4}\right)\right],$$

$$u_2^F(q) = \frac{e^{-q^2/4}}{512n_B}\sqrt{\frac{\pi}{2}}\left[(290-12q^2+28q^4-2q^6+q^8)I_0\left(\frac{q^2}{4}\right) - (56q^2+30q^4+q^8)I_1\left(\frac{q^2}{4}\right)\right],$$

$$u_3^F(q) = \frac{e^{-q^2/4}}{18432n_B}\sqrt{\frac{\pi}{2}}\left[(9270-1458q^2+1809q^4-360q^6+114q^8-14q^{10}+q^{12})I_0\left(\frac{q^2}{4}\right)\right.$$
$$\left. -(1836q^2+1563q^4-192q^6+92q^8-12q^{10}+q^{12})I_1\left(\frac{q^2}{4}\right)\right].$$

Appendix D

Appendices to Chapter 7

D.1 Derivation of the critical point N^*

We will derive the critical number of electrons N^* given in Eq. (7.6), at which the droplet develops a cusp. We start by writing down the equation for the boundary, for general M,

$$z_M^B(t) = r_M e^{it} + u_M e^{-iMt}$$

Remember that the N-dependence is in r_M and u_M. The boundary is parametrized in such a way that one of the fingers is positioned at the x-axis, which corresponds to $t = 0$. We will use this finger to determine the time at which it grows into a cusp. At the critical point, the derivative of both the x- and y-coordinate of the finger with respect to t vanishes. Since we use complex coordinates, the x- and y-coordinates corresponds respectively to the real and imaginary part of $z_M^B(t)$ at $t = 0$. Taking the derivative of $z_M^B(t)$, we get

$$\begin{aligned}\frac{d}{dt}z_M^B(t) &= ir_M e^{it} - iMu_M e^{-iMt} \\ &= ir_M[\cos(t) + i\sin(t)] - iMu_M[\cos(Mt) - i\sin(Mt)] \\ &= -r_M \sin(t) - Mu_M \sin(Mt) + i[r_M \cos(t) - Mu_M \cos(Mt)].\end{aligned}$$

The finger corresponds to $t = 0$, hence we need to set the equation above to zero and put t to zero. This leads to

$$r_M(N^*) = Mu_M(N^*). \tag{D.1}$$

Now, we can use this relation, together with Eq. (7.5), to write N^* in terms of u_M only,

$$\begin{aligned}N^* &= \frac{r_M^2 - Mu_M^2}{2} \\ &= \frac{M(M-1)}{2}\, u_M^2.\end{aligned}$$

To clean up the notation, we have refrained from writing the explicit N-dependence of r_M and u_M. Next, we can derive u_M as a function of t_{M+1} by first writing r_M in terms of t_{M+1}, using Eq. (7.5) and equating it to the expression for r_M that we derived in Eq. (D.1). This yields

$$\left[\frac{u_M}{(M+1)t_{M+1}}\right]^{1/M} = Mu_M.$$

Raising both sides of the equation to the power M and bringing all u_M to one sides, we obtain

$$u_M = M^{-M/(M-1)} \left[(M+1)t_{M+1}\right]^{-1/(M-1)}.$$

Substituting this expression into the equation for N^*, we get

$$\begin{aligned} N^* &= \frac{M(M-1)}{2} M^{-2M/(M-1)} \left[(M+1)t_{M+1}\right]^{-2/(M-1)} \\ &= \frac{1}{2}(M-1)M^{-2M/(M-1)+1} \left[(M+1)t_{M+1}\right]^{-2/(M-1)} \\ &= \frac{1}{2}(M-1)M^{-(M+1)/(M-1)} \left[(M+1)t_{M+1}\right]^{-2/(M-1)}. \end{aligned}$$

Appendix E

Appendices to Chapter 8

E.1 Derivation of the pseudo-magnetic fields

Firstly, we will derive the pseudo-magnetic field that is mentioned in Eq. (8.4), which arises due to deformations caused by the silicon dangling bonds. We start with the height profile of these deformations, which is given by Eq. (8.1),

$$h(x,y) = \frac{h_0}{3} + \frac{2h_0}{9}\left[\cos\left(\frac{2\pi x}{\sqrt{3}\lambda} - \frac{2\pi y}{\lambda}\right) + \cos\left(\frac{2\pi x}{\sqrt{3}\lambda} + \frac{2\pi y}{\lambda}\right) + \cos\left(\frac{4\pi x}{\sqrt{3}\lambda}\right)\right].$$

Using this function, we compute components of the deformation tensor, via Eq. (8.3),

$$\begin{aligned}
u_{xx} &= \frac{1}{2}\left(\frac{\partial h}{\partial x}\right)^2 \\
&= \frac{1}{2}\left(\frac{2h_0}{9}\right)^2\left[-\frac{2\pi}{\sqrt{3}\lambda}\sin\left(\frac{2\pi x}{\sqrt{3}\lambda} - \frac{2\pi y}{\lambda}\right) - \frac{2\pi}{\sqrt{3}\lambda}\sin\left(\frac{2\pi x}{\sqrt{3}\lambda} + \frac{2\pi y}{\lambda}\right) - \frac{4\pi}{\sqrt{3}\lambda}\sin\left(\frac{4\pi x}{\sqrt{3}\lambda}\right)\right]^2 \\
&= \frac{32\pi^2 h_0^2}{243\lambda^2}\left[2\cos\left(\frac{2\pi x}{\sqrt{3}\lambda}\right) + \cos\left(\frac{2\pi y}{\lambda}\right)\right]^2 \sin^2\left(\frac{2\pi x}{\sqrt{3}\lambda}\right), \\
u_{yy} &= \frac{1}{2}\left(\frac{\partial h}{\partial y}\right)^2 \\
&= \frac{1}{2}\left(\frac{2h_0}{9}\right)^2\left[-\frac{2\pi}{\lambda}\sin\left(\frac{2\pi x}{\sqrt{3}\lambda} - \frac{2\pi y}{\lambda}\right) - \frac{2\pi}{\lambda}\sin\left(\frac{2\pi x}{\sqrt{3}\lambda} + \frac{2\pi y}{\lambda}\right)\right]^2 \\
&= \frac{32\pi^2 h_0^2}{81\lambda^2}\cos^2\left(\frac{2\pi x}{\sqrt{3}\lambda}\right)\sin^2\left(\frac{2\pi y}{\lambda}\right), \\
u_{xy} &= \frac{1}{2}\frac{\partial h}{\partial x}\frac{\partial h}{\partial y} \\
&= \frac{16\pi^2 h_0^2}{81\sqrt{3}\lambda^2}\left[2\cos\left(\frac{2\pi x}{\sqrt{3}\lambda}\right) + \cos\left(\frac{2\pi y}{\lambda}\right)\right]\sin\left(\frac{4\pi x}{\sqrt{3}\lambda}\right)\sin\left(\frac{2\pi y}{\lambda}\right).
\end{aligned}$$

The components of the vector potential can then be calculated by using Eqs. (7.11) and (7.12) (with c absorbed in β, like in the rest of that section),

$$\begin{aligned}
A_x &= \beta t\,(u_{xx} - u_{yy}) \\
&= \beta t \frac{32\pi^2 h_0^2}{243\lambda^2}\left\{\left[\cos\left(\frac{2\pi y}{\lambda}\right)\sin\left(\frac{2\pi x}{\sqrt{3}\lambda}\right) + \sin\left(\frac{4\pi x}{\sqrt{3}\lambda}\right)\right]^2 - 3\cos^2\left(\frac{2\pi x}{\sqrt{3}\lambda}\right)\sin^2\left(\frac{2\pi y}{\lambda}\right)\right\}, \\
A_y &= -2\beta t\, u_{xy} \\
&= -\beta t \frac{32\pi^2 h_0^2}{81\sqrt{3}\lambda^2}\left[2\cos\left(\frac{2\pi x}{\sqrt{3}\lambda}\right) + \cos\left(\frac{2\pi y}{\lambda}\right)\right]\sin\left(\frac{4\pi x}{\sqrt{3}\lambda}\right)\sin\left(\frac{2\pi y}{\lambda}\right).
\end{aligned}$$

Finally, we can compute the pseudo-magnetic field, using Eq. (7.13). It reads

$$\begin{aligned}
B_{ps}^0 &= \frac{1}{ev_F}\left(\frac{\partial A_y}{\partial x} - \frac{\partial A_x}{\partial y}\right) \\
&= \frac{\beta t}{ev_F}\frac{256\pi^3 h_0^2}{243\lambda^3}\left[\cos\left(\frac{2\pi y}{\lambda}\right) - \cos\left(\frac{2\sqrt{3}\pi x}{\lambda}\right)\right]\sin\left(\frac{2\pi y}{\lambda}\right).
\end{aligned}$$

Next, we calculate the nonuniform part of the pseudo-magnetic field $\delta B = B - B_0$, where B_0 is the field due to the dangling bonds, which we just derived and B is the total magnetic field that is produced by the combined effect of the dangling bonds and one hydrogen atom that sits on top of one of the bumps, thereby enlarging it. The height profile of the total configuration is given by $h(x,y) + h_H(x,y)$, as defined by Eqs. (8.1) and (8.2). The components of the deformation tensor are

$$\begin{aligned}
u_{xx} &= \frac{1}{2}\left(\frac{\partial h}{\partial x} + \frac{\partial h_H}{\partial x}\right)^2 \\
&= \frac{1}{2}\left(\frac{\partial h}{\partial x}\right)^2 + \frac{1}{2}\left(\frac{\partial h_H}{\partial x}\right)^2 + \frac{\partial h}{\partial x}\frac{\partial h_H}{\partial x} \\
&= u_{xx}^0 + u_{xx}^H + \frac{\partial h}{\partial x}\frac{\partial h_H}{\partial x}, \\
u_{yy} &= \frac{1}{2}\left(\frac{\partial h}{\partial y} + \frac{\partial h_H}{\partial y}\right)^2 \\
&= \frac{1}{2}\left(\frac{\partial h}{\partial y}\right)^2 + \frac{1}{2}\left(\frac{\partial h_H}{\partial y}\right)^2 + \frac{\partial h}{\partial y}\frac{\partial h_H}{\partial y} \\
&= u_{yy}^0 + u_{yy}^H + \frac{\partial h}{\partial y}\frac{\partial h_H}{\partial y}, \\
u_{xy} &= \frac{1}{2}\left(\frac{\partial h}{\partial x} + \frac{\partial h_H}{\partial x}\right)\left(\frac{\partial h}{\partial y} + \frac{\partial h_H}{\partial y}\right) \\
&= \frac{1}{2}\frac{\partial h}{\partial x}\frac{\partial h}{\partial y} + \frac{1}{2}\frac{\partial h_H}{\partial x}\frac{\partial h_H}{\partial y} + \frac{1}{2}\left(\frac{\partial h}{\partial x}\frac{\partial h_H}{\partial y} + \frac{\partial h_H}{\partial x}\frac{\partial h}{\partial y}\right) \\
&= u_{xy}^0 + u_{xy}^H + \frac{1}{2}\left(\frac{\partial h}{\partial x}\frac{\partial h_H}{\partial y} + \frac{\partial h_H}{\partial x}\frac{\partial h}{\partial y}\right).
\end{aligned}$$

The total deformation tensor can thus be written as $u_{\alpha\beta}^{tot} = u_{\alpha\beta}^0 + u_{\alpha\beta}^H + u_{\alpha\beta}^M$, where $u_{\alpha\beta}^M$ consists of the terms that mix both height functions. The components $u_{\alpha\beta}^0$ will give rise to the magnetic field B_0, which we will have to subtract later. Hence, to compute δB,

we have to calculate the vector potential and subsequently the magnetic field that is generated by $u^H_{\alpha\beta} + u^M_{\alpha\beta}$. The derivation of said formula is analogous to the calculation we did for B_0. In the end, we obtain

$$\delta B(x,y) = \frac{\beta t}{e v_F} \frac{h_0^2}{\lambda^3} \left[\frac{4096(y^3 - 3x^2 y)}{H^2} \, e^{-16(x^2+y^2)} + \frac{512\pi}{27H} C(x,y) \, e^{-8(x^2+y^2)} \right], \tag{E.1}$$

where we defined

$$\begin{aligned} C(x,y) = &- \pi y \cos\left(\frac{4\pi x}{\sqrt{3}}\right) + \sqrt{3} x \sin\left(\frac{2\pi x}{\sqrt{3}}\right) \left[16y \cos\left(\frac{2\pi x}{\sqrt{3}}\right) + 8y \cos(2\pi y) + \pi \sin(2\pi y) \right] \\ &+ \cos\left(\frac{2\pi x}{\sqrt{3}}\right) \left[\pi y \cos(2\pi y) + 12(x-y)(x+y) \sin(2\pi y) \right], \end{aligned}$$

and x and y are in units of the lattice spacing λ. This magnetic field is dominated by the first term, hence we can approximate

$$\delta B(x,y) = \frac{\beta t}{e v_F} \frac{H_0^2}{\lambda^3} 4096(y^3 - 3x^2 y) \, e^{-16(x^2+y^2)},$$

which is exactly the pseudo-magnetic field that arises due to the single Gaussian bump defined in Eq. (8.2).

Acknowledgements

Looking back on these nine months of working on my research project, it strikes me how much I have learned. Not only about physics and the specific subject I was studying, but also about what it is like to work as a scientist. I am very grateful for the many people that have so positively contributed to this experience.

First of all, my supervisor Cristiane. Her positive mentality and encouragements have helped me to believe in myself and my work and to find renewed motivation at times that I was stuck. I admire her positive attitude and how she sincerely helps to bring out the best in people.

My co-supervisor from Utrecht, Vladimir, has helped me a lot with all the technical details, for which I am very grateful. Our discussions gave me a great deal of insight that you just can not get out of a book.

Furthermore, I would like to acknowledge Kees and his group, the experimental researcher from TU/e. The experiments really gave an extra dimension to my thesis, which I valued very much. I was always looking forward to the discussions about the experiment and I was very pleased to notice that each time we met, I understood more and more.

Also, I am very pleased about all the discussions I had with fellow students and the scientists that I met during this time. It gave me the oppurtunity to present my work and to get valuable feedback and interesting ideas from different perspectives.

And finally, aside from all the great insights and scientific experiences that this research has enriched me with, one thing that my time in Cristianes group has brought me that I value the most is that I met my current boyfriend Anton. It was great that I could talk with him about my research and he has helped me a great deal when I was stuck on some calculations. But most importantly, he made my life outside the thesis amazing, and I will remember this period in university as the most wonderful of all.

Bibliography

[1] Anthony Hall, http://www.antonyhall.net/works01/heleshaw02.html

[2] D. R. Hofstadter, *Phys. Rev. B* **14**, 2239 (1976).

[3] M. O. Goerbig, P. Lederer, and C. Morais Smith, *Europhys. Lett.* **68**, 72 (2004).

[4] O. Agam, E. Bettelheim, P. Wiegmann, A. Zabrodin, *Phys. Rev. Lett.* **88**, 236801 (2002).

[5] A.J.M. Giesbers, K. Uhlirova, M. Konecny, E.C. Peters, M. Burghard, J. Aarts, and C.F.J. Flipse, *Phys. Rev. Lett.* **111**, 166101 (2013).

[6] C. Riedl, C. Coletti, T. Iwasaki, A. A. Zakharov, and U. Starke, *Phys. Rev. Lett.* **103**, 246804 (2009).

[7] K. V. Emtsev, F. Speck, Th. Seyller, and L. Ley, *Phys. Rev. B* **77**, 155303 (2008).

[8] F. Varchon, P. Mallet, J.-Y. Veuillen, and L. Magaud, *Phys. Rev. B* **77**, 235412 (2008).

[9] S.M. Girvin, *The Quantum Hall Effect: Novel Excitations and Broken Symmetries*, Lecture notes (1998).
http://arxiv.org/abs/cond-mat/9907002

[10] The NIST reference on Constants, Units, and Uncertainty. Accessed June 7, 2015, http://physics.nist.gov/cgi-bin/cuu/Value?rk90|search_ for=adopted_ in!

[11] M.O. Goerbig, *Quantum Hall effects*, Lecture notes (2009).
http://arxiv.org/abs/0909.1998v2

[12] D.C. Tsui, H.L. Störmer, and A.C. Gossard, *Phys. Rev. Lett.* **48** 1559 (1982).

[13] R.B. Laughlin, *Phys. Rev. Lett.* **50**, 1395 (1983).

[14] J.K. Jain, *Phys. Rev. Lett.* **63**, 199 (1989).

[15] J.K. Jain, *Phys. Rev. B* **41**, 7653 (1990).

[16] K.S. Novoselov, A.K. Geim, S.V. Morosov, D. Jiang, M.I. Katsnelson, I.V. Grigorieva, S.V. Dubonos, and A.A. Firsov, *Nature* **438**, 197 (2005).

[17] Y. Zhang, Y.W. Tan, H.L. Stormer, and P. Kim, *Nature* **438**, 201 (2005).

[18] Nobelprize.org. Accessed June 7, 2014, http://www.nobelprize.org/nobel_prizes/physics/laureates/1998/press.html

[19] G. Fano, F. Ortolani, E. Colombo, *Phys. Rev. B* **34**, 2670 (1986).

[20] A.H. MacDonald, *Phys. Rev. B* **30**, 3550 (1984).

[21] J.K. Jain, *Composite Fermions*, Cambridge University Press (2007)

[22] J.H. Ahn, and B.H. Hong, *Nature Nanotechnology* **9**, 737 (2014)

[23] P.R Wallace, *Phys. Rev.* **71**, 622 (1947)

[24] M.O. Goerbig, *Rev. Mod. Phys.* **83**, 1193 (2011)

[25] R. Saito, G. Dresselhaus, and M.S. Dresselhaus, *Physical properties of carbon nanotubes*. Imperial College Press, 1998.

[26] C. Kittel, *Introduction to solid state physics*. John Wiley & Sons, Inc. 2005.

[27] A.H. Castro Neto, F. Guinea, N.M.R. Peres, K.S. Novoselov, and A.K. Geim, *Rev. Mod. Phys.* **81**, 109 (2009)

[28] K.S. Novoselov, Z. Jiang, Y. Zhang, S.V. Morozov, H.L. Stormer, U. Zeitler, J.C. Maan, G.S. Boebinger, P. Kim, and A.K. Geim, *Science* **315**, 1379 (2007).

[29] K. I. Bolotin, F. Ghahari, M. D. Shulman, H. L. Stormer, and P. Kim, *Nature* **462**, 196 (2009).

[30] X. Du, I. Skachko, F. Duerr, A. Luican, and E. Y. Andrei, *Nature* **462**, 192 (2009).

[31] C. Dean, A. Young, P. Cadden-Zimansky, L. Wang, H. Ren, K.Watanabe, T. Taniguchi, P. Kim, J. Hone, and K. Shepard, *Nature Phys.* **7**, 693 (2011).

[32] B. E. Feldman, B. Krauss, J. H. Smet, and A. Yacoby, *Science* **337**, 1196 (2012).

[33] B. E. Feldman, A. J. Levin, B. Krauss, D. A. Abanin, B. I. Halperin, J. H. Smet, and A. Yacoby, *Phys. Rev. Lett.* **111**, 076802 (2013).

[34] B. I. Halperin, *Helv. Phys. Acta* **56**, 75 (1983).

[35] M. O. Goerbig, and N. Regnault, *Phys. Rev. B* **75**,241405 (2007).

[36] K. B. Cooper, M. P. Lilly, J. P. Eisenstein, L. N. Pfeiffer, and K. W. West, *Phys. Rev. B* **60**, 11285 (1999).

[37] J. P. Eisenstein, K. B. Cooper, L. N. Pfeiffer, and K. W. West, *Phys. Rev. Lett.* **88**, 076801 (2002).

[38] M.O. Goerbig, P. Lederer, and C. Morais Smith, *Phys. Rev. B* **69**, 115327 (2004).

[39] H. Bruus and K. Flensberg, *Many-body quantum theory in condensed matter physics*, (2003).

[40] R. Chitra, T. Giamarchi, and P. Le Doussal, *Phys. Rev. Lett.* **80**, 3827 (1998).

[41] M. M. Fogler and D. A. Huse, *Phys. Rev. B* **62**, 7553 (2000).

[42] S. M. Girvin, *Phys. Rev. B* **30**, 558 (1984)

[43] S. M. Girvin, A. H. MacDonald, and P. M. Platzman, *Phys. Rev. B* **33**, 2481 (1986).

[44] R. Shankar, *Phys. Rev. B* **63**, 085322 (2001).

[45] G. Murthy and R. Shankar, *Rev. Mod. Phys.* **75**, 1101 (2003).

[46] J. P. Eisenstein, K. B. Cooper, L. N. Pfeiffer, and K. W. West, *Phys. Rev. Lett.* **88**, 076801 (2002).

[47] M. O. Goerbig, R. Moessner, and B. Douçot, *Phys. Rev. B* **74**, 161407 (2006).

[48] E. H. Rezayi and N. Read, *Phys. Rev. Lett.* **72**, 900 (1994).

[49] G. Moore and N. Read, *Nucl. Phys. B* **360**, 362 (1991).

[50] C. H. Zhang and Y. N. Joglekar, *Phys. Rev. B* **75**, 245414 (2007).

[51] K. Park, N. Meskini, and J.K. Jain, *J. Phys. Condens. Matter* **11**, 7283 (1999).

[52] R. M. Lewis, Yong Chen, L. W. Engel, D. C. Tsui, P. D. Ye, L. N. Pfeiffer, and K. W. West, *Phys. Rev. Lett.* **93**, 176808 (2004).

[53] Guohong Li, A. Luican, J. M. B. Lopes dos Santos, A. H. Castro Neto, A. Reina, J. Kong, and E. Y. Andrei, *Nature Physics* **6**, 109 (2010).

[54] M. R. Peterson and C. Nayak, *Phys. Rev. Lett.* **113**, 086401 (2014).

[55] C. H. Zhang and Y. N. Joglekar, *Phys. Rev. B* **77**, 205426 (2008).

[56] P. Wiegmann, arXiv:cond-mat/0204254.

[57] T. L. Hughes, A. D. Klironomos, and A. T. Dorsey, *Phys. Rev. Lett.* **90**, 196802 (2003).

[58] N. Levy, S. A. Burke, K. L. Meaker, M. Panlasigui, A. Zettl, F. Guinea, A. H. Castro Neto, M. F. Crommie, *Science* **329**, 5991 (2010).

[59] M. I. Katsnelson, *Graphene (Carbon in two dimension)*, Cambridge University Press (2012).

[60] M. A. H. Vozmediano, M. I. Katsnelson, and F. Guinea, *Phys. Rep.* **496**, 109 (2010).